

**Functional Polymer Nanocomposites and Nanohybrids:
Synthesis, Characterization and Application**

BY

ARINDAM DAS
B.M.E., Jadavpur University, India, 2006

THESIS

Submitted as partial fulfillment of the requirements
for the degree of Doctor of Philosophy in Mechanical Engineering
in the Graduate College of the
University of Illinois at Chicago, 2013

Chicago, Illinois

Defense Committee:

Constantine M. Megaridis, Chair and Advisor
Amin Salehi-Khojin
Christos G. Takoudis, Bioengineering/Chemical Engineering
Danilo Erricolo, Electrical and Computer Engineering.
Ranjan Ganguly, Jadavpur University, India.

ACKNOWLEDGEMENT

I had the opportunity to be surrounded by so many nice people around me, without whose kind support and advice I could never have thought of completing the serious endeavor of my doctoral thesis. First and foremost, I would like to express my heartfelt gratitude to my doctoral advisor and mentor Prof. Constantine M. Megaridis. Without his continuous support, mentoring and faith in my ideas and abilities, I could never have achieved what I have so far. I am also grateful for his personal interest in making my life as graduate student as smooth as possible, especially when I was struggling to adapt with the challenging situations of my personal and professional life during the initial years of my graduate studies.

My sincere thanks to my ex lab mate Dr. Manish Kumar Tiwari and our collaborator Dr. Ilker Bayer for introducing me to the field of surface wettability, the main area of my research work. I sincerely thank both of them for their systematic guidance and help towards me to acquire skills essential for an experimentalist. They were also instrumental in several works that I have published.

I am also grateful to Dr. Abhijit Biswas and Dr. Lei Liu (Univ. of Notre Dame) for their support and collaboration in the field of THz EMI shielding.

I would like to offer my sincere thanks to Dr. Despina Fragouli and Dr. Ilker Bayer of Istituto Italiano di Tecnologia for collaborating on anisotropic polymer nanocomposites. I also appreciate all the help and encouragement from my lab mates Tom Schutzius, Shreyas Kapatral, Joseph Mates, Mohamed Elsharkawy and Aritra Ghosh. Special thanks to Tom and Shreyas for collaborating on several projects.

ACKNOWLEDGEMENT (continued)

I am also forever grateful to my undergraduate mentors from Jadavpur University, Dr. Achintya Mukhopadhyay and Dr. Swarnendu Sen. I could never have had the courage to undertake higher studies abroad if it were not for their constant encouragement and blessings.

I am eternally thankful to have seniors and special friends like Kaustav, Harish, Sandeep, Niru, Biswadeepa, Sumita, Swarvanu, Moumita, Chandan, Neena, Bibhash, Moumi, Arnab, Nilanjana, Saugata, Swarnava, Koushik, Niladri, Zanker, Suman, Abir, Arjun, Soumyo, Tathagata, Ketaki, Payoli, Navendu and many more. The fun chats, parties, festivals, food, interesting coffee time discussion, dinners, movies, and outings created some beautiful moments in my life. Their presence always made me feel at home in Chicago, thousands of miles away from my native country India.

I am profoundly grateful to my parents Mr. Jayanta Das and Mrs. Purabi Das. Without their constant support and encouragement and lots of sacrifices, I could never have reached this point.

AD

TABLE OF CONTENTS

<u>CHAPTER</u>	<u>PAGE</u>
1. INTRODUCTION	1
1.1. Nanotechnology	1
1.2. Research philosophy and procedure	2
1.3. Nanocomposites and nanohybrids	4
1.4. Motivation	6
1.5. Background	11
1.5.1. Wettability considerations	11
1.5.2. Ice nucleation theory	18
1.5.2.1. General concept of nucleation	18
1.5.2.2. Thermodynamic/kinetic theory	19
1.5.2.2.1. Homogeneous ice nucleation	19
1.5.2.2.2. Heterogeneous nucleation	23
1.5.2.2.2.1. Rate of heterogeneous nucleation.....	25
1.5.3. Superhydrophobic surface as ice phobic surface	26
1.5.4. Electromagnetic wave shielding	27
1.5.4.1. Definition of S –parameter and measurement of SE	29
1.6. Thesis objectives	31
1.6.1. Polymer nanocomposite surface of extreme wettability and applications	32
1.6.2. EMI shielding properties of multifunctional conductive polymer nanocomposites in GHz and THz frequency domain	32
1.6.3. Superoleophobic surface from ink like dispersion of carbon nanofibers.....	32
1.6.4. Synthesis and characterization of a nanohybrid material based on magnetic nanoparticle filled carbon nanofibers	33

TABLE OF CONTENTS (continued)

CHAPTER	PAGE
2. POLYMER NANOCOMPOSITE COATING OF EXTREME WETTABILITY: SYNTHESIS, CHARACTERIZATION AND APPLICATION	34
2.1. Introduction	34
2.2. Polymer nanocomposite coatings for anti-icing applications	38
2.3. Passive icephobic properties of PTFE based superhydrophobic surfaces	41
2.3.1. Materials and method	41
2.3.2. Surface characterization	42
2.3.3. Experimental setup	43
2.3.4. Results: freezing delay	44
2.3.5. Theoretical considerations	45
2.4. Conductive superhydrophobic surfaces for active anti icing	48
2.4.1. PTFE-CNF-PVDF-PMMA conductive composite coatings	48
2.4.1.1. Material and surface synthesis	48
2.4.1.2. Surface morphology	50
2.4.1.3. Electro-thermal characterization of composite coatings	51
2.4.1.4. Icing experiment	52
2.4.2. CNF-PMC electro-conductive composite coatings	60
2.4.2.1. Materials and surface synthesis	60
2.4.2.2. Surface morphology	60
2.4.2.3. Electro-thermal properties	61
2.4.2.4. Icing experiment	62

TABLE OF CONTENTS (continued)

<u>CHAPTER</u>	<u>PAGE</u>
3. SUPERHYDROPHOBIC, ELECTRICALLY CONDUCTING, POLYMER COMPOSITES FOR GHz AND THz ELECTROMAGNETIC WAVE ATTENUATION AND THz DEVICES	66
3.1. Introduction	66
3.2. PTFE-CNF based, electrically conducting, superhydrophobic composites as THz and GHz film attenuators.	69
3.2.1. Experimental	69
3.2.2. Solutions/dispersions and spray application	69
3.2.3. Conductivity, contact angle and roll-off angle measurement	70
3.2.4. Scanning electron microscope observation	70
3.2.5. Definition and measurement of S parameter	71
3.2.6. Results	72
3.2.6.1. Shielding results in the X-band	73
3.2.6.2. Shielding results in THz frequencies	75
3.3. PMC based conductive patterns as THz polarizer	76
3.3.1. Material and nanocomposite synthesis	77
3.3.2. Results and discussion.....	77
4. SUPEROLEOPHOBIC AND CONDUCTIVE CARBON NANOFIBER /FLUOROPOLYMER COMPOSITE FILMS	85
4.1. Introduction	85
4.2. Experimental	87
4.2.1. Materials and preparation of CNF/PMC composite	87

TABLE OF CONTENTS (continued)

<u>CHAPTER</u>	<u>PAGE</u>
4.2.2. Coating characterization	88
4.3. Results and discussion	89
4.3.1. Dispersion considerations	89
4.3.2. Coating surface morphology	94
4.3.3. Large-area coating wettability and effect of underlying substrate roughness.....	94
4.3.4. Microscale application: Ink-Jet printed Patterns	100
5. CARBON NANOFIBER-MAGNETIC NANOPARTICLE NANOHYBRID AND ITS APPLICATION IN FABRICATION OF POLYMER NANOCOMPOSITE OF HIGHLY ANISOTROPIC PROPERTY	102
5.1. Introduction	102
5.2. Materials and processes	104
5.2.1. Dispersion procedures	106
5.2.2. Drying of suspensions	106
5.2.3. Washing of dried powder to remove nanoparticles from CNF wall exterior	107
5.3. HRTEM characterization of filled CNF	107
5.4. Results and discussion	107
5.4.1. Effect of nanoparticle dispersibility	107
5.4.2. Effect of dispersion medium	110
5.4.3. Influence of process parameters	111
5.4.3.1. Sonication time	112
5.4.3.2. Sonication type	114
5.4.3.3. Concentration of solids in dispersions	116
5.4.3.4. CNF to nanoparticle mass ratio	118

TABLE OF CONTENTS (continued)

<u>CHAPTER</u>	<u>PAGE</u>
5.4.3.5. Drying temperature	119
5.4.3.6. Sonication before drying	121
5.5. Tilt mode observation of LHT CNFs	123
5.6. Intercalation of HHT CNFs	124
5.7. Response of intercalated CNFs under an external magnetic field	125
5.8. Application: Alignment of magnetic CNFs to fabricate polymeric coatings of anisotropic properties	126
5.9. Conclusion	128
CITED LITERATURE	129
APPENDIX	147
VITA	158

LIST OF TABLES

<u>TABLE</u>		<u>PAGE</u>
I	CONTACT ANGLE, ROLL-OFF ANGLE, COMPOSITION, SOLVENTS AND ELECTRICAL CONDUCTIVITY OF THREE CNF/PTFE COMPOSITES.	50
II	ENERGY SPENT TO COMPLETELY MELT THE FROZEN WATER DROPLET.	53
III	ENERGY SPENT FOR SHEDDING FROZEN WATER DROPLET FROM THREE DIFFERENT SURFACES HELD AT DIFFERENT TILT ANGLE. NA INDICATES THAT NO DROPLET DETACHMENT OCCURRED AT THE CORRESPONDING CONDITIONS.	54

LIST OF FIGURES

<u>FIGURE</u>		<u>PAGE</u>
1.	Liquid contact angle and three different interfacial tensions at 3-phase contact point.	12
2.	Hydrophobic and Hydrophilic surface.	13
3.	a) Superhydrophobic; b) Superhydrophilic; c) Self-cleaning surface.	13
4.	Cassie and Wenzel model.	15
5.	Liquid drop rests on composite surface of solid and air or vapor.	16
6.	Variation of advancing contact angle with roughness parameter r	17
7.	The free energy of a nucleus of the new phase as a function of nucleus radius.	20
8.	Spherical Ice nucleus on solid surface and submerged in water phase.	24
9.	Comparison of Gibbs free energy variation with roughness between Homogeneous and heterogeneous nucleation.	25
10.	Electrical and magnetic components of an electromagnetic wave.	27
11.	Two-port network defining the quantities used in the definition of the S parameters.	29
12.	Experimental setup implementing the schematic of Fig. 11. The coating sample (red) is fully encased at the coupling of the two waveguides, to ensure minimal outside interference.	30
13.	Natural superhydrophobic surfaces of (a) Lotus leaf and (d) Water strider. SEM images of (b),(c) lotus leaf and (e), (f) Water strider at different magnifications. Image a and b were adapted from references 79 (reproduced by permission of AIP). Image c was adapted from reference 75 by permission of the Royal	

LIST OF FIGURES (continued)

<u>FIGURE</u>	<u>PAGE</u>
Society. Images d, e, f were adapted from reference 78 (reproduced by permission of ACS).....	35
14. Scanning Electron Microscopic images of superhydrophilic plant surfaces of (a) the water plant (<i>Anubias barteri</i>), (b) water-adsorbing moss (<i>Sphagnum squarrosum</i>), (c) water-adsorbing moss <i>Rhacocarpus purpurescens</i> , (d) the Spanish moss (<i>Tillandsia usneoides</i>), (e) The leaf of <i>Calathea xiiebrine</i> , (f) the superhydrophilic leaves of <i>Ruellia devosiana</i> . Images reproduced from: Koch, K., and Barthlott, W., Superhydrophobic and superhydrophilic plant surfaces: an inspiration for biomimetic materials, <i>Phil. Trans. R. Soc. A</i> , 2009, 367, 1893, 1487–1509, by permission of the Royal Society.	36
15. Naturally occurring patterned wettable surface of (a) of Nabib desert beetle (elytra), Scale bar is 10 mm), (b) wax free hydrophilic zone in waxy superhydrophobic background, (c) Scanning electron micrograph of the textured surface of the depressed areas .(Scale bars are 10 mm, 0.2 mm and 10 μm). Reprinted by permission from Macmillan Publishers Ltd: <i>Nature</i> , ^[81] copyright 2001.	36
16. Schematic of Spray casting process for applying polymer nanocomposite coatings on surfaces. All of the superhydrophobic composites were spray deposited by an air brush.	37
17. (a), (b) Scanning electron micrographs of a superhydrophobic coating (sample2) studied in ref. 97, (c) Average roughness values Ra (DIN 4768) and advancing contact angles θ for selected surfaces studied in same reference.	42

LIST OF FIGURES (continued)

<u>FIGURE</u>	<u>PAGE</u>
18.	Schematic drawing of the setup showing flow of nitrogen gas (blue arrows) and thermocouples T1-T3 (red dots). This setup is available at Swiss Federal Institute of Technology, where these measurements were performed.43
19.	Logarithmic box plot of the time to freezing (or freezing delay) of a growing (through successive impacts of ink-jetted droplets) sessile droplet on each of the ten surfaces considered ^[97] in the experiments performed by our collaborators at ETH-Zurich. (b) Clarifying illustration of a (linear) box plot for the surface “7_Ref_sb_AL”, showing the time-to-freezing minimum and maximum (crosses), median (M), and the arithmetic mean (filled square). The middle 50% of the data distribution falls within the open box. The ends of the two “whiskers” extending from the box indicate the locations of the furthest non-outlier data points, (c) Geometric area of the liquid –solid interface at the onset of freezing for each surface.45
20.	(a) Freezing delay time t_{med} (median values) vs. advancing contact angle for “highly” corrugated surfaces, $x \gg O(10)$. Contrary to the classical nucleation theory (Fitting curve 1), the extended model (Fitting curve 2) offers a better fit for the experimental data (symbols). (b) Freezing delay time (median values) vs. roughness for smooth surfaces, $x \leq O(10)$. The value beside each symbol indicates the measured contact angle of the respective surface. The extended model is indicated by Fitting curve 3. Excellent agreement between experiments and theory is apparent in both plots.48
21.	SEM images of CNF/PTFE/PVDF/PMMA coatings at (a) 1000 \times ; (b) 5000 \times ;

LIST OF FIGURES (continued)

<u>FIGURE</u>	<u>PAGE</u>
(c) 10000× ; (d) 35000× magnifications.	50
22. I-V curve of PTFE/CNF based (a) S1 (self-cleaning, roll-off angle <10°), (b) S2 (high roll over angle, roll-off angle ~40°); (c) S3 (sticky) superhydrophobic nanocomposite surfaces.	51
23. Surface temperature evolution of PTFE/CNF/PVDF/PMMA self-cleaning surface at (a) -30°C; (b) -15°C ambient temperature at different voltages applied for skin heating. Relative humidity of 30% and air velocity of 2 m/s were maintained inside the chamber.	52
24. (a) Environmental Chamber; (b) Schematic of Experimental setup.	52
25. Sequence of ice from supercooled water shedding off from the surface even when most of the ice was not melted.	55
26. Sequence of supercooled (-11°C) with water droplet interaction with self-cleaning surface held at (a)-(d) -5°C and (e)-(f) -16°C. Figures (a) – (d) were taken at 250 ms interval. Figures (e) – (g) were also taken at 250 ms. Figure (h) was taken 3 minutes after the image (g). Inset of figure (h) shows the frost halos formed around the periphery of the frozen droplet on the surface.	56
27. Image of PTFE/CNF coating (a) before, (b) after defrosting with peltier. Figure (c) shows the surface after subjected to gentle air blow.	58
28. Condensation of water vapor into micro droplets on the PTFE/CNF self-cleaning composite surface inside the environmental scanning electron microscope operated in wet mode. Figure (a) was taken at pressure 6.4 Torr during the condensation process. Figure (b) was taken at pressure 6 Torr,	

LIST OF FIGURES (continued)

<u>FIGURE</u>	<u>PAGE</u>
<p>during the process of gradual pressure reduction to facilitate evaporation of the droplets. For all these experiments ambient temperature was lowered ($\sim 4^{\circ}\text{C}$) to achieve 100% relative humidity.</p>	58
<p>29. PTFE/CNF based self-cleaning under extremely humid environment of 90% RH and 15°C. (a) surface before condensate reaches critical size; (b) condensed droplet with diameter above critical radius glides down from the surface and exposes new area for condensate to form; (c) showing one drop gliding down the surface and taking with it all droplets in its path; (d) surface after a gentle blow of air.</p>	59
<p>30. ESEM images of 30:70 CNF:PMC composite surfaces at (a) $100\times$ and (b) generated by the HHT CNFs.</p>	61
<p>31. I-V curve of 30:70 CNF: PMC composite.</p>	61
<p>32. Surface temperature evolution of CNF-PMC 30:70 nanocomposite self-cleaning surface at (a) -30°C; (b) -15°C ambient temperature. Relative humidity of 40% and air velocity of 2 m/s were maintained inside the chamber.</p>	62
<p>33. Schematic diagram of experimental set up used to evaluate the performance of CNF-PMC coatings in defrosting experiments.</p>	62
<p>34. Showing a sequence from a defrosting experiment (a) at beginning, after (b) 23, (c) 25 (d) 58 seconds after skin heating process started. Three surfaces were glass slide, coating without skin heating and with skin heating (from left to right).</p>	65
<p>35. SEM image of composites with CNF loading of (a),(b) 0.068 ; (c),(d) 1.1 at different magnifications.</p>	71

LIST OF FIGURES (continued)

<u>FIGURE</u>	<u>PAGE</u>
36.	Frequency domain terahertz spectroscopy system (available at Notre Dame University).....71
37.	(a) Electrical conductivity and sessile water contact angle for various (PVDF+PMMA)/PTFE/CNF composite coatings as a function of CNF loading expressed in terms of CNF/(PVDF+PMMA) weight ratio. In all cases, the PTFE/polymer weight ratio was 5.76. The conductivity regimes suitable for different applications are marked by the horizontal lines. (b) Water droplet roll-off angle on coatings with different CNF loadings.72
38.	Variation of transmitted and reflected power with amount of CNF loading expressed in % of incident power.73
39.	S parameters, S_{11} (reflection) and S_{21} (transmission), for coatings with different CNF loading in the 8.2-12.4 GHz frequency range (X-band), as obtained by means of the two-port measurement setup shown in Fig. 10a. 74
40.	(a) Transmission vs. Frequency plot for sample with different CNF loading; (b) Variation of conductivity and percentage transmitted power with CNF loading.75
41.	2-D transmission map of sample E5.76
42.	Scanning electron micrograph of a CNW/PMC (1:1 mass ratio) coating.77
43.	THz power transmission measurement results for composite coating samples with CNW/PMC mass ratio of 1:1 and average thicknesses as stated on the legend.79
44.	(a) Design of the THz polarizer fabricated on 25 μm -thick Mylar film, with 100 μm -wide microstrips separated by 100 μm spacing. The prototype polarizer

LIST OF FIGURES (continued)

<u>FIGURE</u>	<u>PAGE</u>	
<p>had 1 μm CNW/PMC film thickness (h) and was characterized in the frequency band of 0.57–0.63 THz with the frequency domain THz spectrometer of Fig. 1(b). (b) Parallel orientation (0°) for minimum transmission, and (c) perpendicular (90°) orientation for minimum attenuation. (d) Optical microscope image of the inkjet-printed prototype THz polarizer. The dark lines consist of the CNW/PMC film material. The magnified detail shows the spatial non-uniformity of a typical strip. The dark areas depict high content of CNWs, while the bright areas indicate lower particle presence.</p>	81	
45.	<p>(a) THz transmission (T) spectra of the prototype CNW polarizer for three different polarization orientations: 0°, 45°, and 90°. (b) Corresponding absorbance, defined as $A = -\log_{10}(T)$, for the above three orientations and following Ref. 138.</p>	82
46.	<p>The degree of polarization (P) of the prototype THz polarizer over the frequency range of 570–630 GHz. An average degree of polarization of ~ 0.35 is seen for this polarizer with coating thickness of only 1 μm.</p>	83
47.	<p>Schematic of the effect of formic acid on CNF dispersion stability. CNFs phase separate in the absence of formic acid (top panel), whereas CNFs disperse and produce ink like stable dispersions (bottom panel) in the presence of formic acid.</p>	91
48.	<p>Role of PMC during CNF dispersion in acetone, formic acid and water mixture. (Left) Without PMC, large aggregates form (red circle); (Right) With PMC, superior CNF separation prevents aggregate formation.</p>	92

LIST OF FIGURES (continued)

<u>FIGURE</u>	<u>PAGE</u>
49. High resolution TEM image of CNF walls (a) after formic acid treatment; inset shows enlargement of intact grapheme layers of CNF wall, indicating no chemical modification; (b) after treatment with formic acid and fluoropolymer dispersion diluted to 0.01 wt%; inset shows detail of polymeric layer adsorbed over the outer CNF wall composed of intact grapheme layers.	93
50. Scanning electron microscope images showing surface morphology of a thick coating (on smooth paper) comprising 25 wt. % CNFs within the PMC polymer matrix. (a) Low magnification surface topology, and (b) enlargement of sub-micron surface roughness due to CNF bundles held together by the polymer.	94
51. Variation of (a) sessile contact angle and droplet roll-off angle for water and oil, and (b) electrical conductivity with CNF loading for thick composite coatings applied on smooth glass slides.	95
52. (a) Scanning electron microscope image showing morphology of a conformal superhydrophobic CNF/PMC composite (25 wt. % CNF in total solids) spray-deposited on a 600 grit sand paper (average roughness 15 μm). (b) Higher magnification image showing coverage of sand paper micro roughness with the CNF/PMC composite web. (c) SEM image showing surface morphology of the bare 600 grit sand paper.	96
53. Variation of water (a) sessile contact angle and (b) droplet roll-off angle with CNF loading for conformal composite coatings deposited on sand papers of different micro-roughness (grit size in legend). Increasing grit size indicates reduced roughness.	97

LIST OF FIGURES (continued)

<u>FIGURE</u>	<u>PAGE</u>
54. Variation of oil static contact angle with CNF loading for conformal composite coatings deposited on sand papers of varying micro-roughness (grit size in legend).	98
55. Scanning electron micrographs showing surface morphology of CNF/PMC (25 wt. % CNF in solids) CNF/PMC composite films spray cast and dried on (a) 1200 grit, and (b) 1500 grit sand paper surfaces. The inset in (b) shows an enlargement of the marked area.	99
56. Hydrophobic and conducting carbon/fluoropolymer composite lines printed on a hydrophilic Mylar substrate (yellow background) from a dilute carbon nanowhisiker/PMC solution using an ink-jet nozzle of 60 μm dia. The carbon nanowhisiker concentration in the dried composite film is 50 wt. %. The dark areas depict high content of nanowhisikers, while the bright areas indicate lack of the particle filler.	101
57. HRTEM micrographs showing portions of: (a) 1500°C-treated (LHT) CNF, and (b) 3000°C-treated (HHT) CNF. The insets show magnified details of the graphitic wall structure for each fiber.	105
58. HRTEM images of CNFs containing magnetite nanoparticles originating from: (a-c) EMG-911 Ferrofluid; (d-f) non functionalized, dry magnetite nanoparticle powder. The liquid dispersant used in both cases was toluene. The cellular structures seen in the CNF cavity in (d-f) were created by the drying of the solvent that had imbibed into the CNF cavity. The edges of the supporting carbon film are visible in (a), (b) and (f).	108

LIST OF FIGURES (continued)

<u>FIGURE</u>	<u>PAGE</u>
59.	Visual comparison of magnetite nanoparticle dispersions (in toluene) prepared with: (a) functionalized nanoparticles supplied in EMG-911 Ferrofluid, and (b) non-functionalized dry powder nanoparticles. The dispersions were subjected to 10 min of probe sonication, and left to sit for 10 minutes before the two images were taken. 109
60.	Magnetite nanoparticles intercalated in CNFs. The respective dispersion liquid was: (a) Toluene, (b) Water, (c) Acetone.111
61.	Typical nanoparticle-intercalated CNFs produced after (a), (b) 10 min; (c) 60 min; (d) 360 min of bath sonication. The curved edges of the supporting carbon film are visible in (b), (c) and (d).112
62.	Nanoparticle-intercalated CNFs after: (a) 10s, (b) 100 sec; (c) 1000 sec of probe sonication. 113
63.	Nanoparticle-intercalated CNF with one end capped by clustered nanoparticles.114
64.	Intercalated CNFs from 10 min of probe sonication. The curved edge of the supporting carbon film is visible in (a).115
65.	Intercalated CNFs obtained from experiments having: (a), (b) 10 mg CNF – 4.16 mg magnetite nanoparticle (from EMG 911), 0.1 wt% solid concentration in 20 ml toluene ; (c),(d) 1 mg CNF-0.416 mg magnetite nanoparticle (from EMG 911), 0.01 wt% solid concentration as starting dispersion.....117
66.	Intercalated CNFs obtained with Nanoparticle:CNF ratio of (a) 0 .416:1 (b) 0.104:1.dispersion in 20 ml toluene dispersion. The curved edges of the supporting carbon film are visible in both images. 118
67.	Intercalated CNFs obtained from drying at: (a) room temperature; (b) 120°C.

LIST OF FIGURES (continued)

<u>FIGURE</u>	<u>PAGE</u>
Note the denser packing in (b), as compared to (a).	120
68. Magnified detail of HRTEM image showing bending of grapheme sheets from CNF wall (left) toward the surfactant nanoparticle mixture at the core of CNF (right).	121
69. HRTEM image of intercalated CNF obtained from experiment where the Ferrofluid nanoparticles were added after sonication of the Ferrofluid. The curved edges of the supporting carbon film can be also seen.	122
70. Tilt specimen HRTEM images of intercalated CNFs rotated at: (a) -17° ; (b) 0° , (c) 17° around the CNF axis. Such imaging helps in determining whether particles are encased within the CNF cavity or are attached to the exterior walls.	124
71. HRTEM images of intercalated CNFs from (a), (b) 60 min of probe sonication; (c), (d) 240 min of bath sonication.	125
72. (a) Well dispersed magnetized CNFs in toluene; (b) Separation of magnetized CNFs from toluene in the presence of a bar magnet (0.1 T).	126
73. Oriented magnetic nanofibers in PMMA nanocomposite with 1 wt% nanofiber loading, prepared by solution casting process under 0.13 Tesla magnetic field. Alignment experiment were performed by our collaborator at Italian Institute of Technology, Italy.	127
74. I-V measurement in 1 wt% magnetic-CNF nanocomposite with aligned nanofibers under an external magnetic field. Measurements were performed by our collaborator at Italian Institute of Technology, Italy.	128

SUMMARY

Nanoparticle-based polymer nanocomposites offer opportunities to develop many advanced materials of multiple functionalities with wide scope for property tunability. All nanocomposite surfaces in this work were prepared by spray coating different substrates with a nanoparticle-polymer solution/dispersion. Multiple functionalities, such as electrical conductivity, extreme water repellency, extreme oil repellency, ice-frost phobicity, electromagnetic interference (EMI) shielding, and magnetic function were introduced into the polymer composites. Based upon the application, either single or multiple functionalities were incorporated into a single polymer composite. The first topic of this dissertation is the icephobic performance of extremely non-wettable surfaces (a.k.a. superhydrophobic). The problem of icing is very critical to many industrial problems, such as aircraft icing, wind turbines, power cable failures. Since the water has very low residence time on superhydrophobic self-cleaning surfaces during droplet impact, this approach is used to address the problem of aircraft icing. Superhydrophobic/hydrophobic coatings with high electrical conductivity were synthesized by incorporating conductive carbon nanofibers (CNFs) in two different polymeric systems. In one composition, 60:40 weight ratio of Poly (vinylidene fluoride) and Poly (methyl methacrylate) were used as matrix material, whereas a fluorinated acrylic co-polymer (PMC) was used in the second composition. Anti-icing and defrosting performance of these coatings were evaluated under skin heating condition, by applying DC voltage across these surfaces.

The second part of the thesis is focused on synthesis of various electrically conductive films and their application as effective low-cost large-area electromagnetic interference shielding materials over frequencies ranging from GHz to THz. Conductive composites based on carbon nanofibers, Poly-tetrafluoroethylene nanoparticle filler and PVDF-PMMA polymer blends were fabricated by spray casting. These surfaces showed excellent shielding performance at both GHz and THz

SUMMARY (continued)

frequencies. Shielding performance of two other compositions made of carbon nanofibers or carbon nanowhiskers (CNW) and PMC were also studied at THz frequencies. The fabrication and performance of a THz polarizer based on an ink-like CNW dispersion was also reported in the EMI shielding section of this thesis. Using ink-jetting, conductive hydrophobic line patterns were generated. These line patterns showed 30% polarization of incoming electromagnetic waves.

The third part of this thesis describes the synthesis of carbon nanofiber inks and their use in the preparation of oleophobic and superoleophobic surface coatings. The ink-like dispersions were prepared by ultrasonically dispersing the CNFs in a mixed solvent system comprising of acetone, formic acid and subsequent mixing of sonicated/dispersed CNFs with 20 wt.% PMC (in water) dispersion. The dispersions were sprayed on smooth or microtextured surfaces, thus forming conformal coatings after drying. Nanostructured composite films of different degrees of oil and water repellency were attained by varying the concentration of CNFs. The effect of substrate micro texture and CNF content on oil/water repellency was studied.

The fourth and final section discusses a unique nanohybrid material composed of superparamagnetic nanoparticles and hollow heat-treated CNFs. Influences of several experimental parameters were studied with respect to the intercalation efficiency, which was determined by transmission electron microscopy images. The filled CNFs showed excellent response under a magnetic field. The magnetic CNFs were also used as a filler in a PMMA-based nanocomposite prepared by solvent casting. When the solution casting method was carried out in a magnetic field, the magnetic CNFs oriented themselves along the magnetic field lines, thus creating a polymer nanocomposite of highly anisotropic electrical conductivity and magnetic property. The

SUMMARY (continued)

synthesis process of this nanohybrid also opens up an opportunity to study nanoparticles under nanoscale confinement.

The present work demonstrates several possible applications of polymeric nanocomposites, which have the potential to advance new areas of research and technology. Due to their low cost, multifunctionality, synthesis scalability and property tunability, the present composites show advantages that should facilitate their incorporation in applications over the near future.

1. INTRODUCTION

1.1 Nanotechnology

The term Nanotechnology defines the subject area where properties of materials having one or more dimension less than 100 nm^[1] are being investigated, explored and utilized in different scientific and technical applications.

Several ancient civilizations^[2,3,4] have used nanomaterials in their technologies unknowingly, but in the present era the area of nanotechnology emerges in the 1980's by the discovery of the Scanning Tunneling Microscope (STM) and Fullerenes. STM was developed by Gerd Binnig and Heinrich Rohrer in 1981.^[5] Fullerenes were discovered by Harry Kroto, Robert Curl and Richard Smalley in 1985.^[6] For their discoveries, all of the above researchers were awarded the Nobel prize. The huge potential of nanotechnology was first envisioned and predicted by visionary scientist Richard Feynman in his lecture "There's Plenty of Room at the Bottom" at Caltech in 1959, much earlier than its actual emergence.^[7]

Owing to their very high surface to volume ratio and nanometer characteristic length, nanomaterials possess several unique properties much different than their bulk values. It is these properties which have generated a tremendous amount of interest in scientific research communities cutting across various fields of science and engineering and now promoting interdisciplinary collaborative research. Because of the very high values of specific surface area in nanomaterials, the relative number of molecules close to the surface is very high, which leads to significant variations of their electronic, optical, electro-magnetic and thermodynamic or mechanical properties and behavior.^[8] Altering the size, shape and chemical composition intelligently along with highly optimized synthesis process, material and devices of novel properties and performance can be generated, even when this seemed impossible. The area of nanotechnology is currently expanding almost in an exponential pace indicated by the number of

journal and research papers in this field. Almost every field of science and technology -including modern medical science- are now being heavily dependent on nanotechnology research to address the future challenges in their respective fields.

1.2 Research philosophy and procedure

Research in nanotechnology constitutes three major steps, namely material synthesis, characterization and application. Nanomaterials studied in the field of nanotechnology are now being produced via numerous and versatile techniques employing chemical and physical processes. Synthesis of nanomaterials is broadly classified into three different categories based on their approaches, namely top down, bottom up and combination of these two. In top down approaches, nanomaterials are produced by reducing the dimensions of the material gradually to nanometer scale employing externally controlled tools and techniques. This approach usually starts with a bulk or thin film material and removes selective regions in order to fabricate nanostructures or nanodevices (similar to micromachining techniques) utilizing submicron lithographic techniques. Nowadays, most advanced NEMS devices are fabricated by “top-down” approaches, which combine existing process technologies, such as electron-beam lithography, conventional film growth, chemical etching, etc. A typical example of non-lithographic “top-down” approach is “soft lithography”,^[9-12] where a master or mold is used to generate patterns, identified by the relief on its surface, on polymers by replica molding,^[13] embossing (nanoimprint lithography) ,^[14] or by micro contact printing or μ CP.^[15] As the dimension of the devices gets reduced to much smaller scale, the top down approach becomes very challenging and costly. Hence the “bottom-up” approaches emerged. Unlike their top down counterparts, “bottom-up” approaches involve the fabrication of nanoscale devices in similar way that nature creates objects, by sequential assembly of atomic and/or molecular building blocks. The bottom-up approach mainly relies on nanochemistry^[1,16-21] and includes chemical synthesis, the spontaneous self-assembly of molecular clusters (molecular self-assembly) from simple reagents in solution or

biological molecules as building blocks to produce three-dimensional nanostructures. Typical examples are molecular-beam epitaxy (MBE) and organometallic vapor-phase epitaxy (OMVPE) used to create specialized crystals one atomic or molecular layer at a time, and manipulation of individual atoms by a scanning tunneling microscope or an atomic force microscope or atom optics. Bottom-up approaches are expected to produce devices in parallel and much cheaper than top-down methods, but could potentially be of no use as the complexity and size of the assembly or devices increase. Mixed approaches utilize both of the previous two techniques to produce nanomaterials or devices. One example of mixed techniques is fabrication of nanotube based electronic devices, where initially catalyst particles are deposited at selective locations on a nano/micro device (top down approach) and then nanotubes are produced on those selective locations using the bottom up approach.

After synthesis, characterization of the synthesized nanomaterials and estimation of their properties/performance with cutting edge instruments are performed. The discovery of the Atomic Force Microscope (AFM) and the Scanning Tunneling Microscope (STM) are the earliest of scanning probes that catalyzed the launch of the field of nanotechnology. There are other types of scanning probe microscopy, coming from the ideas of the scanning confocal microscope proposed by Marvin Minsky in 1961 and the scanning acoustic microscope (SAM) by C. Quate and coworkers in the 1970s, enabling to see structures at the nanometer scale. Surface visualization at the nanoscale and beyond has been facilitated by Scanning Electron Microscopy (SEM). Transmission Electron Microscopes (TEM) are used extensively to see inside material samples having thickness less than 100nm. Other important instrument/techniques used extensively in nanotechnology to characterize materials are different types of spectrometers, XPS, XRD, EDX, NMR etc. Several conventional instruments are also used with or without some modification to evaluate/measure the performance or properties (thermal, electrical, mechanical) of macroscale materials made out of nanoscale components. The Differential Scanning

Calorimeter (DSC), thermal conductivity measuring systems, and nanoindenters are just a few examples of such instruments.

Based upon the properties of the basic nanomaterials and their arrangement, applications vary widely. Application of nanomaterials ranges from different sensors, actuators, electro-magnetic-optical devices, smart materials, functional polymer composites and coatings, heat transfer enhancement fluids or interfaces, drug synthesis/design/delivery to energy harvesting devices, memory chips, electronic devices, catalysis and in so many other areas invading most branches of science and technology. Detailed description of these applications is beyond the scope of this thesis.

1.3 Nanocomposites and nanohybrids

The term nanocomposite is used to define a multiphase solid material having at least one of its constituents with one or more of its physical dimensions less than 100nm.^[1] Usually Nanocomposites are a solid state mixture of one solid state bulk material and one or more nanofiller particles of different mechanical, electrical, thermal, optical and electrochemical and catalytic properties, drastically different than the respective matrix materials. Nanocomposites are often divided in three major different categories based upon the type of matrix material, namely metal-matrix, ceramic-matrix and polymer-matrix. The matrix material helps to bind the nanofillers together and also with the substrate, if applied as a coating. Sometimes the matrix also provides some functionality, such as environmental protection or serves as corrosion barrier to the nanofillers. Generally the purpose of the nanoparticles is to provide the necessary functional properties to the matrix material which it lacks. In that sense, nanocomposites are similar to regular composite materials. But due to their very high surface-to-volume ratio and unique properties arising out of this characteristic, their application in composite materials is nontrivial. The presence of nanomaterials in nanocomposites changes the properties of the matrix materials

drastically, as mentioned above. Size limits for these effects have been proposed to be ^[22] <5 nm for catalytic activity, <20 nm for making a hard magnetic material soft, <50 nm for refractive index changes, and <100 nm for achieving superparamagnetism, mechanical strengthening or restricting matrix dislocation movement. For example, introduction of high aspect ratio carbon nanotubes into highly insulating materials imparts electrical conductivity through percolative electrical connectivity.^[23, 24] Similarly, other functional properties can be imparted by choosing appropriate nanofillers ^[25,26] and even those properties can be well tuned by changing the filler loading.^[27]

Out of the above mentioned three different nanocomposite types, polymer composites are gaining much attention these days in industry and research communities due to their ease of processing, application, low cost, low weight, flexibility and versatility in properties. Though polymer matrix nanocomposite generally contains very small amounts of nanofillers, sometimes when the presence of nanostructure on the nanocomposite surface is necessary to impart certain surface functionality, the volume fraction of nanofillers has to increase to such great extent that the polymer just serves as binder material for those nanofillers. This thesis devotes most of its chapters on such nanostructured coatings with different functional properties along with a prime focus on extreme wettability (very low to very high). Extreme wettability of these nanocomposites is an outcome of their micro-nano hierarchical surface morphology generated by the presence of nanofillers at high volume fractions in these nanocomposites.

Whereas nanocomposites have matrix materials of macroscopic or bulk length scale, there exists special types of composite materials where each of the constituents has nanoscale/molecular level dimensions, thus forming composites at the nanometer scale itself. These special types of nanoscale composites are called nanohybrid materials. Most of these nanohybrid materials are made of one inorganic and one organic part. Formation of composites at the nanoscale gives some distinct features to the nanohybrid materials. Material homogeneity is far more superior, and

composites show characteristics of both constituents or sometimes show completely new properties. Nanohybrid materials are formed either through non chemical interaction (such as Van-der-waals, hydrophobic, hydrogen bonding and Coulombic interaction) or by chemical bonding between constituent materials. Several different approaches have been used to prepare nanohybrid materials. One way of producing such materials is by formation of all components in-situ from their respective precursor simultaneously or with only one component in the presence of another component. “Sol gel” process of making organic or inorganic hybrid material is one such example, where these materials are produced through continuous chemical modification of their precursors. In another approach, known as building block approach- constituents do not lose their properties completely while forming the hybrid material. One example is nanoparticles of inorganic materials with organic groups attached outside their surface. In the building block approach, one more constituent material of nano/molecular scale possesses one or more active groups which interact either chemically or through physical bonding (Van-der-waals, Coulombic, hydrogen bonding, hydrophobic-hydrophilic interaction, etc.). The latter part of this thesis discusses synthesis and application of one such nanohybrid composite material where nanoparticles of magnetite were intercalated inside hollow carbon nanofibers. Possible application of such nanohybrid materials is also explored along with the study of intercalation process parameters.

1.4 Motivation

The field of nanotechnology is expanding rapidly owing to its huge technological and scientific potential. It will not be an overstatement to describe present time as the era of nanotechnology. Almost all branches of science and technology are now progressing due to the advancement of nanoscience and nanotechnology. Out of so many nano technological research areas, polymer matrix functional nanocomposites, nanoparticle dispersions and nanohybrid materials are getting more importance/interest in the research community owing to their unique and application

oriented properties. The present thesis focuses on synthesis of polymer nanocomposites and nano hybrid materials based on potentially scalable processes. The production of such materials involved mixed approaches of top-down and bottom up techniques.

Preparation of polymer nanocomposites presented in this thesis was accomplished by a wet based spray process which can be easily scaled up for mass production of these coatings. This process begins with the preparation of stable dispersion of nanoparticles, used as fillers in the composite materials. Dispersion of nanoparticles is also important, while preparing nanoparticle based nano-hybrid materials, as discussed in the last chapter of the present thesis. The following paragraphs describe the importance and motivation behind the individual projects undertaken in this work.

To impart a specific property to polymer matrix nanocomposites, nanoparticles having such properties are being used as filler material. Polymer matrix nanoparticle filler composites also have the flexibility to allow multiple functionalities. By incorporating two types of nanoparticles with different properties in an optimum ratio, a composite possessing properties of both the nanofillers can be produced. For example, when a surface in addition to extreme water repellency (superhydrophobic) requires other functional properties, such as electrical conductivity, ice phobicity or chemical inertness, the intelligent choice of micro and nanomaterials (proper combination of morphology, size and functionality) is important.

Surfaces of extreme repellency or extreme wettability to water or other liquids have huge potential and application in a number of fields. Areas, such as droplet based microfluidic systems, high heat flux cooling of high energy microelectronics components, anti-fouling surfaces, and low drag surfaces, corrosion resistant coatings, icephobic surfaces, organic solvent resistant surfaces, coatings with multiple functionality, protective materials in biological or chemical warfare, etc. are expected to gain momentum from the research in this particular field. Polymer matrix composites in addition to their functional properties also possess certain good properties,

such as low weight, flexibility, and good adherence on the underlying surface made of different materials.

Icing is of great importance in different technological fields. Some important examples of icing are aircraft icing, icing of wind turbines, power cables, icing on water vessels in cold climatic regions and frost formation on several surfaces.^[28,29] Superhydrophobic surfaces as potential icephobic surface have been proposed long ago, but in most of those cases complicated processes were employed to generate surfaces which cannot be produced in large scale. So superhydrophobic surfaces produced via scalable processes are required for their practical applications. The second chapter of this thesis discusses different water repellent superhydrophobic surfaces produced via spray with primary focus on icephobic self-cleaning superhydrophobic behavior. Superhydrophobic surfaces with high electrical conductivity were also synthesized along with other similar nonconductive surfaces. Additional functionality of electrical conductance was imparted to superhydrophobic self-cleaning surfaces for use in active electrical heating, in addition to the icephobic characteristics of self-cleaning surfaces. Though several studies showed^[28, 29] the icephobic nature of self-cleaning surfaces, the influence of surface roughness, filler size and other surface properties -such as contact angle and roll off angle- on icing delay lacks understanding. Moreover, the application of active heating on ice removal from superhydrophobic surfaces with electrical conductivity has never been explored. Hence the second chapter of the thesis addresses these issues through studying the icephobic properties of superhydrophobic nanocomposite coatings.

Surfaces with extreme wettability have several potential applications in heat transfer engineering. Similar to superhydrophobic surfaces, superwetting surfaces are technologically significant at the other end of the wettability spectrum. Usually when some liquid completely wets the surface with contact angle of 0° , then that surface is called superwetting with respect to that particular liquid. Nanocomposite coatings made out of hydrophilic or rather high surface energy polymer matrix

materials and nanoparticle-induced nanotexture can produce such superwetting surface. Choice of proper micro/nano filler and spraying parameters can also make special nanocomposite surfaces where liquid not only forms very low contact angle but also spreads rapidly. One such surface is discussed in the second part of the second chapter along with its potential as a heat transfer surface. Superhydrophobic surfaces -when combined with superwetting surfaces, in particular geometric patterns- can also influence heat transfer rates, especially when this involves phase change. Surface of hydrophobic/hydrophilic patterns have already shown their positive influence in boiling heat transfer^[30] and their possible application in fog collecting^[31,32] devices. The third part of the second chapter discusses few such surfaces.

Preparation of stable nanoparticle dispersions is very critical in polymer-nanocomposite synthesis. Based upon the size, shape and material and intended dispersion medium, different techniques are employed. To impart distinct functionalities to the nanocomposites, different nanoparticles are chosen, as based on their properties. When desired properties are related to some transport properties, such as electrical conductivity or heat transfer, nanofillers with high aspect ratio (length to thickness ratio) are preferred. Carbon-based materials offer one of the best choices to impart thermal or electrical properties due to their high temperature stability, high melting point, low chemical activity and corrosion resistance. Formulation of these carbon-based conductive nanoparticle dispersions as inks can greatly increase their scope of application in printed electronics and electromagnetic devices. Thus, the third chapter of this thesis discusses one novel technique to disperse carbon-based nanomaterials and prepare inks which can be ink-jetted. High temperature treated Carbon Nanofibers (CNF) in this ink also have desired morphological features of highly re-entrant surfaces, as required to generate superoleophobic surfaces.^[33] Just like superhydrophobic surfaces, superoleophobic surfaces also have many technical applications. Moreover, making these surfaces self-cleaning with respect to oils could open up new technological applications, such as oil vapor collectors, chemical sensors, oil based

heat transfer surfaces, etc. Synthesis and wettability study of one such superoleophobic and self-cleaning surface are also presented in Chapter 3 of this thesis.

Synthesis of electrically conductive polymer nanocomposites is heavily pursued ^[34, 35] because of their many potential applications. Usually highly electrically conductive carbon nanotubes are used in conductive nanocomposites due to their high aspect ratio. But due to the higher cost of carbon nanotubes (CNTs), large scale production of CNT-based nanocomposites is not feasible. Low cost but high-aspect-ratio nanofillers, such as CNF or Carbon Nano Whiskers (CNW) are alternative choices to CNTs. Apart from several different applications, electrically conductive composite surfaces can be used as effective electromagnetic wave interference shielding materials. When electromagnetic waves pass through an electronic device they may disturb its function and sometime permanently damage it. To protect instruments from such outside interference, nanocomposites of electrical functionality can be employed. Due to their light weight, corrosion resistance and flexibility, conductive polymer composites are preferred than metals. Apart from Electro Magnetic Interference (EMI) shielding, they can be used in different types of opto-electronic devices, if produced in special geometric pattern. Chapter 4 of this thesis presents synthesis and shielding performance of CNF and CNW based nanocomposites in GHz and THz frequency domains.

Carbon nanotube based nanohybrid materials and their applications^[36] have been widely reported in the literature. Intercalation is one such process that can produce such materials. Mostly inorganic materials, such as metals, metal oxides, metal halides, etc. have been used as intercalating materials. Fullerene and its chemical derivatives were also introduced inside the CNTs.^[37] Several studies have also reported nanohybrid materials of CNTs and biomaterials, such as DNA.^[38] Most of these processes have either incorporated other nanomaterials outside of the nanotubes or synthesized materials inside the hollow cavity of the nanotubes by different chemical means. Very few of these studies ^[37] have tried to intercalate nanomaterials inside CNTs

from the outside. These types of nanohybrid materials apart from having unique properties, protect the intercalated components from being changed or degraded chemically, thus increasing their lifetime. Intercalation of foreign nanomaterials inside the CNTs from outside possess significant challenges owing to the very small inner diameter and complicated end opening of the CNTs. Carbon nanofibers with mostly open-ended hollow structure with comparatively large diameter allows a better alternative to the CNTs. Intercalation of materials from solution or dispersion into the CNFs is an effective process with potential to achieve large scalability. Very few works have tried to intercalate materials^[39, 40] inside CNFs. Nanoparticles of many different elements and compounds are easily available in the market at very low prices. Hence rather than making nanoparticles inside the CNF cavity by some chemical process, filling CNF cavities with as-received nanoparticles from their dispersion may be an intelligent and versatile option for mass production. The 4th and final chapter of this thesis reports synthesis techniques and application of one such nanohybrid material made up of super paramagnetic nanoparticles intercalated in the hollow cavity of highly graphitic CNFs.

1.5 Background

1.5.1 Wettability considerations

Wettability of a surface translates into how well a liquid wets the surface. Various important engineering technologies as well as many natural phenomena and processes are highly governed by the wettability of materials with respect to specific liquid. Natural phenomena, such as cleanliness of plant leaves, motion of water insects, transport of moisture, water or biological fluids in plants and animal body, geological formations and mineral deposits, heavily depend on the surface wettability of the related materials. On the other hand, the science of surface wettability has a critical role on engineering technologies, such as coating industry, medical technologies,

fluid handling and transportation devices, drug industry, garment industry, polymer processing, energy, etc. Thus, proper understanding of surface wettability is very important.

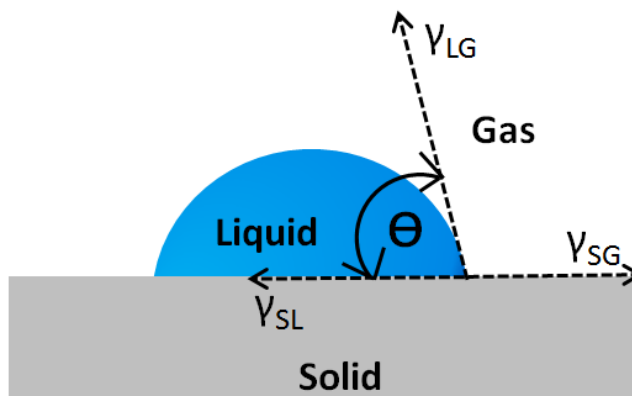


Figure 1: Liquid contact angle and three different interfacial tensions at 3-phase contact line

The basic understanding of surface wettability starts from the wettability of homogeneous, smooth solid surfaces and can be described by Young's or equilibrium contact angle at the liquid-solid-air (3 phase) contact line. The value of contact angle is the direct outcome of mechanical balance of interfacial surface tensions or surface energy, as described in Fig. 1. The angle Θ made by the tangent on the gas-liquid interface at the liquid-solid contact point with the solid surface is defined as Young's or equilibrium or static contact angle. Under equilibrium, the contact angle is related to the various interfacial surface energies and given by the Young-Dupre^[42] equation.

$$\cos \theta = \frac{\gamma_{SG} - \gamma_{SL}}{\gamma_{LG}} \dots\dots\dots (1)$$

Based upon the value of this contact angle, a surface can be described as either phobic or philic to a particular liquid. When water is considered, a surface is called hydrophilic or hydrophobic when water contact angle on that surface is below or above 90° , respectively (Fig 2). Strictly

speaking, an ideal hydrophilic surface should have 0° contact angle, whereas a surface with contact angle less than 90° and higher than 0° should be called partially wettable surface.

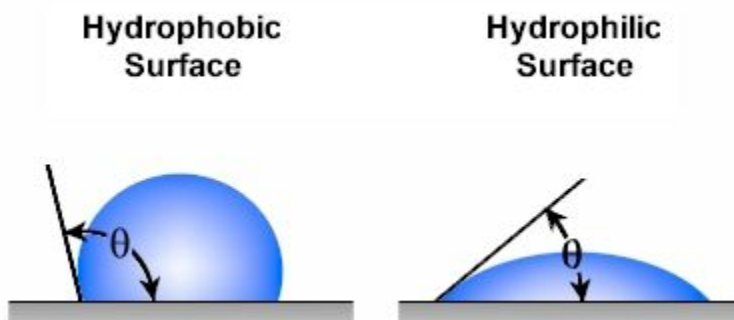


Figure 2: Hydrophobic (left) and hydrophilic (right) surfaces

Both hydrophobic and hydrophilic surfaces have many applications. When surfaces achieve complete wettability (0° degree contact angle) or complete repellency (180° contact angle), then unique and novel applications are possible using these surfaces.

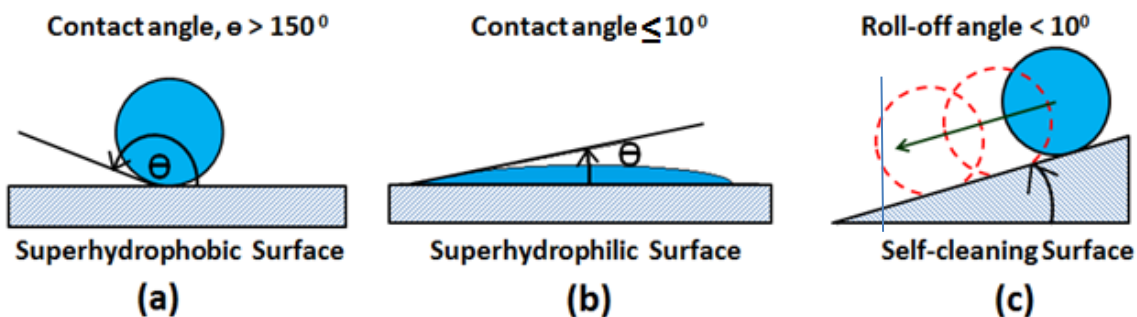


Figure 3: a) Superhydrophobic ; b) Superhydrophilic ; c) Self-cleaning surface

To characterize the wettability properties of any surface, two important parameters are used namely, liquid contact angle and roll-off angle. While the first parameter indicates the degree of water repellency of the surface, the latter parameter indicates the mobility of water on that

surface. Water contact angle is defined by the angle that the tangent on the water-gas interface makes with the liquid-solid interface at the point where the three phase meet. Roll off angle is the angle at which the liquid droplet rolls off from the surface when the surface is tilted slowly from its horizontal position. When a surface has contact angle higher than 150° , it is referred to as Superhydrophobic surface, as shown in Fig. 3.a. The surface is called superhydrophilic when the contact angle is below 10° , as shown in Fig 3.b. The roll off angle is mainly associated with superhydrophobic surfaces and indicates their self-cleaning properties. When superhydrophobic surfaces have roll off angle less than 10° they are called self-cleaning superhydrophobic, as shown in Fig. 3.c.

Since the maximum known water contact angle possible for any smooth material is 120° , other synthetic ^[42, 43] methods are employed to achieve higher contact angle. Increasing surface roughness or by introducing micro-nano hierarchical surface texture can be one of such techniques and particularly relevant to the wettability characteristics of the nanoparticle-filled polymer matrix nanocomposites discussed in this thesis. Nanoparticles introduced in polymer nanocomposites not only provide specific functionality but can also alter the roughness/texture (along with other micro particles) to tune the surface wettability characteristics. Sometimes these nanoparticles apart from providing necessary roughness features also control the overall surface energy of the surface material if incorporated in the composite with higher amount of loadings. Proper choice of micro and nanoparticles and the polymer matrix material can not only make the surfaces display contact angles higher than 120° but also extremely water repellent, where contact angle exceeds 150° and the roll off angle is below 10° (self-cleaning). Similarly, a hydrophilic surface can be made more hydrophilic with contact angle less than that of a smooth surface made of the same surface energy material.

The initial research on superhydrophobic surface was mainly motivated from the extreme water repellent lotus leaf ^[44] which also has micro-nano scale rough surface morphology. By changing

the surface texture and surface energy of both fillers and matrix materials, different types of self-cleaning surfaces were produced. [43,45,46]

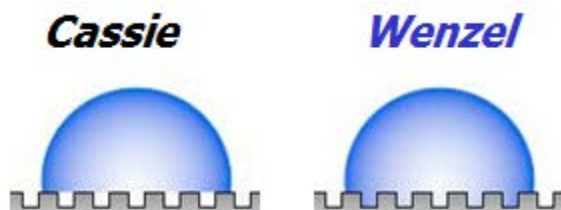


Figure 4: Cassie (left) and Wenzel (right) model of liquid/solid contact

To understand the wettability of the textured surface, two main equations are used, despite their shortcomings and limitations. The equation of Wenzel and Cassie-Baxter are these two equations, which estimate the contact angles of the surfaces based upon two different models (as shown in Fig. 4). In the former case, water is assumed to penetrate the surface asperities and apparent contact angle is estimated from the following relation,

$$\cos \theta^* = r \cos \theta \dots\dots\dots (1)$$

where θ^* and θ are, respectively, the apparent and smooth surface contact angles and r is the ratio of total to projected surface area. Wenzel's equation predicts two important aspects. For $r > 1$, when $\theta > 90^\circ$ (hydrophobic surface), $\theta^* > \theta$ i.e.; for hydrophobic surface, increasing roughness causes contact angle to increase. Similarly for $\theta < 90^\circ$ (hydrophilic), $\theta^* < \theta$ i.e.; for hydrophilic surface, increasing surface roughness will decrease the contact angle. The Cassie-Baxter model, unlike Wenzel's model, estimates the contact angle of a chemically heterogeneous surface as described by the following equation based on surface energy minimization,

$$\cos \theta^* = f_1 \cos \theta_1 + f_2 \cos \theta_2$$

where f indicates fraction of surface area occupied by a particular material and θ indicates its contact angle. When used to describe the wetting state for hydrophilic material ($\theta < 90^\circ$) the Cassie –Baxter equation simplifies into the following form,

$$\cos \theta^* = 1 - \phi_s + \phi_s \cos \theta \dots\dots\dots(2)$$

where, ϕ_s is the fraction of area occupied by the solid underneath the droplet. This model contradicts the fact that a surface can be completely wettable (0° contact angle) in clear contradiction to Wenzel’s law. Now to find out the limit of Wenzel’s law of wetting, a parameter θ_c is introduced based on energy minimization and given by the following equation,

$$\cos \theta_c = \frac{1-\phi_s}{r-\phi_s} , \dots\dots\dots (3)$$

When $\theta < \theta_c$, a film will impregnate the texture and the Cassie-Baxter law best describes the wetting behavior. For $\theta_c < \theta < 90^\circ$, the solid ahead of the droplet will remain dry, thus the Wenzel equation describes the wetting correctly.

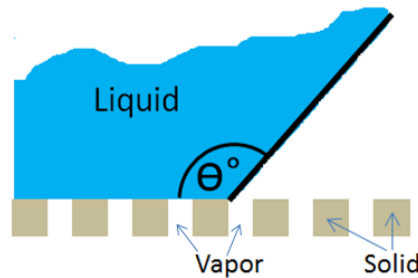


Figure 5: Liquid drop resting on composite surface of solid and air or vapor

To understand the wetting properties of hydrophobic materials, a model (as described in Fig. 5) features a surface made of both solid and air pockets. Application of the Cassie-Baxter equation yields the following relationship,

$$\cos \theta^* = -1 + \phi_s (1 + \cos \theta) \dots\dots\dots (4)$$

This relation predicts a distinct behavior from Wenzel's model. According to this model, the contact angle cannot reach the ideal value of 180° since for that ϕ_s will have to be zero, which is unrealistic. But according to Wenzel's model, this is possible as soon as the value of $r \cos \theta$ reaches the value of -1.

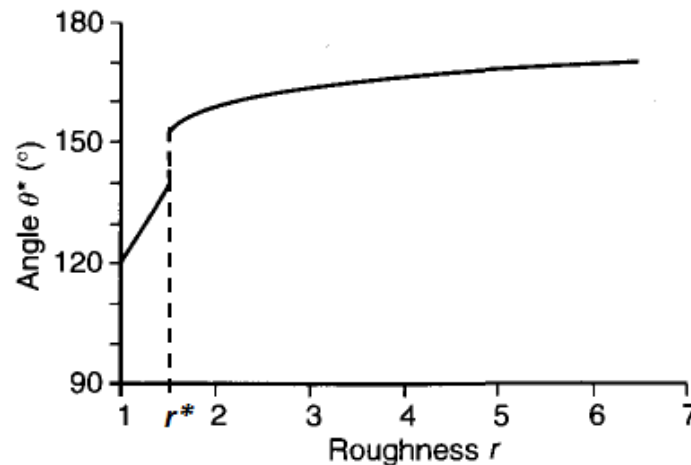


Figure 6: Variation of advancing contact angle with surface roughness parameter r

In all practical cases, it is observed that with the value of r approaching a certain value r^* , the contact angle increases slowly and then jumps rapidly (as shown in Fig. 6) indicating the presence of trapped air within the surface asperities. To estimate the onset of this regime of air entrapment, a critical contact angle θ_c is proposed, and is obtained by minimizing the contact line displacement energy. This critical angle is given by Equation (3) mentioned above.

For given values of r and ϕ_s , when Young's contact angle θ lies between 90° and θ_c , the water completely follows the contour of the surface roughness (Wenzel case), but even in this case air entrapment is reported and seems to indicate a metastable state. When θ is greater than θ_c , entrapment of air is ensured and indicates a stable condition. For a given surface energy of the hydrophobic surface when the value of r crosses the critical value r^* , the apparent water contact angle jumps to a very high value (Fig. 6). The value of r^* is given by the following equation,

$$r^* = 1 + \frac{\tan^2\theta}{4} \dots\dots\dots(5)$$

For $\theta = 120^\circ$ (maximum possible contact angle on smooth surface) the value of $r^* = 1.75$. Hence values of r greater than 1.75 ensure entrapment of air. Equation 3 gives the guideline for designing a super repellent surface by changing the surface energy of the materials, whereas Equation 5 does the same, but by changing the roughness factor r .

Both the Wenzel and Cassie-Baxter models have some limitations^[47] hence they must be used carefully where applicable. It has been experimentally proven^[47] that the contact angle of a droplet is mainly determined by the contact line dynamics, not by the roughness features beneath the bulk droplet. It was also shown^[48] that the Wenzel and Cassie Baxter equations are valid when the length scales of the roughness on composite surfaces are either similar or less than the contact line length scale (i.e.; $2\pi R$). Since the roughness features in polymer nano-composite surfaces are of micron to nanometer scale, the Wenzel and Cassie-Baxter equations are valid to describe the wettability of these surfaces.

1.5.2. Ice nucleation theory

The term nucleation can be defined as extremely localized formation of a different thermodynamic phase. Ice nucleation is a special case of nucleation where the solid phase (ice) is formed in liquid water at very small length scales. Ice formation on various solid surfaces is of practical importance in many industries. The mechanism of ice formation and nucleation is also very important from the fundamental scientific point of view.

1.5.2.1. General concept of nucleation

The formation of ice from a metastable supercooled state occurs via ice nuclei, which are tiny and transient clusters of ice which exist in various sizes dispersed within the water phase. Continuous fluctuations in the sizes of these clusters, due to the simultaneous addition of molecules and the

detachment of same, the size of these nuclei continuously fluctuates. Based upon the various thermodynamic parameters, their size may grow large enough to become stable, i.e. for growth to become more probable than decay. This is termed as reaching the critical size for stability, and hence nucleation of the new phase. Stability of ice nucleus mainly depends upon the surface area to volume ratio of the nucleus. As size of the ice phase increases, the relative value of the surface area decreases and the relative number of interior molecules increases. This makes the number of molecules returning to the water phase from the surface of ice far less significant compared to the number of interior molecules, hence stability of the nucleus increases and growth of its size is facilitated. Nucleation of this type is known as homogeneous nucleation. There exists another type of nucleation where the nucleus forms on some pre-existing solid structure, thus making the stability of the nucleus more probable. This type of nucleation is known as heterogeneous nucleation. For studying ice nucleation on micro-nano hierarchical surfaces, both of these theories play an important role.

From the definition of homogeneous nucleation it is evident that it requires a greater degree of meta-stability (supercooling or supersaturation) than heterogeneous nucleation. Similarly, ice can also form on the solid surface from the vapor state and this phenomenon is known as ice deposition or atmospheric frost formation. Thus in the atmosphere, ice nucleation may occur by either heterogeneous or homogeneous freezing, or heterogeneous deposition. Homogeneous deposition does not occur in the atmosphere.

1.5.2.2. Thermodynamic/kinetic theory

1.5.2.2.1. Homogeneous Ice nucleation

In terms of thermodynamic free energies, the new phase (solid, in freezing) is expected to have lower bulk energy. That is why solid is always the stable phase at the conditions considered. Hence the volume energy of the nucleus is negative, and proportional to the number of molecules

within it. The interfacial surface tension energy between the nucleus and the parent phase is positive and approximately proportional to the $2/3$ power of the number of molecules. The sum of these two energy (volume and surface) terms thus has a maximum at the critical nucleus size r^* , indicating that below that size growth is energetically unfavorable, but beyond that size growth is spontaneous as increasing size leads to decreasing total potential for the cluster.

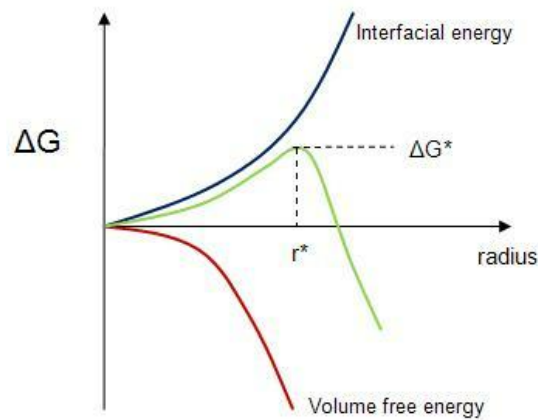


Figure 7: Gibbs free energy of a nucleus of the new phase (ice) as a function of nucleus radius.

When a liquid is cooled below the maximum heterogeneous nucleation temperature (melting temperature), but above the homogeneous nucleation temperature (pure substance freezing temperature) it is said to be in super-cooled state. Supercooling provides the necessary driving force required for nucleation. Super-saturation occurs when the pressure in the newly formed solid is less than the liquid pressure, which brings about a change in free energy per unit volume between the liquid and the newly created solid phase. This change in free energy reflects the gain of volume free energy and the energy loss due to creation of a new interface. When this overall free energy change is negative, the triggering mechanism (i.e. nucleation) is favored.

In the classic case^[49] a spherical nucleus which liberates $-G_v$ Joule/cm³ volume free energy during its formation ($G_v < 0$), the positive cost of σ Joules/cm² surface free energy must be compensated. Hence the required free energy to form a spherical cluster of radius r is,

$$\Delta G = -\frac{4}{3}\pi r^3 G_v + 4\pi r^2 \sigma \dots\dots\dots (6)$$

where the right-hand terms represent volume free energy and surface free energy changes respectively. Until the radius r reaches r^* , it is $\frac{dG}{dr} > 0$, which means that in order to increase the nucleus size, free energy must be spent. Hence up to this point, nucleus growth is not energetically favored. The critical radius r^* is given by

$$r^* = -\frac{2\sigma}{G_v}$$

as obtained by setting $\frac{dG}{dr} = 0$. When the radius reaches r^* , addition of molecules results in release of energy rather than absorption. From this point on, growth of the cluster does not depend on nucleation and possibly controlled by diffusion.^[50] Gibbs free energy at this critical radius is given as

$$\Delta G^* = \frac{16\pi\sigma^3}{3(G_v)^2} \dots\dots\dots (7)$$

The term G_v or ΔG_v is related to the enthalpy of fusion (ΔH_v), equilibrium temperature (T) and degree of supercooling or undercooling (ΔT).

From the basic thermodynamic equation of free energy,

$$\Delta G_v = \Delta H_v - T\Delta S_v \dots\dots\dots (8)$$

Since at the melting point $\Delta G_v = 0$, the above equation gives

$$\Delta S_v = \frac{\Delta H_v}{T_m}$$

Putting this value of ΔS_v in equation (8) we can express ΔG_v as follows

$$\Delta G_v = \Delta H_v - T\left(\frac{\Delta H_v}{T_m}\right) \dots\dots\dots (9)$$

and using the relationship $\Delta T = T_m - T$ in equation (9), ΔG_v becomes

$$\Delta G_v = \frac{\Delta H_v}{T_m} \Delta T \dots\dots\dots (10)$$

It is clear that a greater degree of super-cooling ΔT increases the probability of phase transformation. The critical radius r^* and corresponding Gibbs free energy (ΔG^*) can be expressed in terms of the degree of super-cooling ΔT as follows

$$r^* = \frac{2\sigma T_m}{\Delta H_v} \frac{1}{\Delta T} \dots\dots\dots(11)$$

$$\Delta G^* = \frac{16\pi\sigma^3 T_m^2}{3(\Delta H_v)^2} \frac{1}{(\Delta T)^2} \dots\dots\dots(12)$$

From Equations (11) and (12) it is evident that increasing the amount of super-cooling, the critical nucleus size decreases and so does the free energy of formation of the same.

Another important aspect of ice nucleation is how to describe the fluctuation of nucleus size. In order to understand this effect, a steady state described by a Boltzmann distribution has been assumed for nucleus sizes between 0 and the critical radius and for an energy change of $\Delta G(n)$ and expressed as follows

$$N(n) = N_0 e^{-\frac{G(n)}{kT}} \dots\dots\dots(13)$$

where $N(n)$ and N_0 stand for the number of nuclei and the number of single molecules per unit volume of the parent phase. Boltzmann's distribution is used here because of Einstein's theory that the probability of some state arising by fluctuation is proportional to the negative exponential of the entropy change involved. Similarly, the nucleation rate J (units $L^{-3}T^{-1}$) is also expressed as

$$J = A e^{-\frac{\Delta G^*}{kT}} \dots\dots\dots(15)$$

where the pre-exponential factor, A , depends on slowly varying quantities, such as the molecular mass, the molecular concentration in the parent phase, temperature and others. The most influential parameter is ΔG^* which is related to the degree of super-cooling or super saturation.

Detailed derivations of the nucleation rate can be found elsewhere in the literature; Götze, Mészáros and Vali,^[51] Young,^[52] Pruppacher and Klett^[53] have nucleation theory in great detail.

The specific form of nucleation rate J (from vapor to solid) can be expressed as

$$J = A \exp\left[-B \frac{\sigma^3}{T^3} \frac{1}{(\ln S)^2}\right] \dots\dots\dots(15)$$

where A and B are constants (approximately), σ is the interfacial energy between liquid and vapor, T the absolute temperature, and S is the saturation ratio. This equation is also valid for homogeneous nucleation of the liquid phase from the vapor phase.

The expression for freezing is more controversial due to the alternative ways of estimating the free energy change using temperature and pressure-dependent density, specific heat, etc. The form given below is from Jeffery and Austin^[54]

$$J = A_f \sigma_{i/w}^{1/2} \exp\left[-B_f \frac{\sigma_i^3}{kT} \frac{1}{\left\{\ln\left(\frac{T_m}{T}\right)\right\}^2}\right] \dots\dots\dots (16)$$

where A_f and B_f denote some temperature dependent quantities expressed in simple form to demonstrate the most important temperature dependence of J; $\sigma_{i/w}$ is the liquid/ice interfacial tension, T the temperature and T_m is the melting point (273 K for water). The term A_f incorporates a factor $\exp[-\Delta G/kT]$ which accounts for the molecular flux to the nucleus. The term ΔG , known as *activation energy*, is determined from self-diffusivity measurements.

From both of the above equations it can be concluded that the nucleation rates are highly sensitive to the interfacial tension. The two equations also indicate rapid change of J with S or T. Those very rapid changes are indication of threshold super-saturation and threshold temperature, denoted by S_{th} or T_{th} corresponding to $J = 1 \text{ cm}^{-3} \text{ s}^{-1}$. The sharp onset of homogeneous nucleation as estimated from these equations corroborates well with the experimental observation and takes place, for ice, at $S_{th} \gg 5-8$, and $T_{th} \gg -40^\circ\text{C}$. Homogeneous deposition is not possible in the atmosphere, as the degree of supersaturation required for it is too high. Even if that was not the case, according to Ostwald's rule of stages, at temperatures below T_m , the liquid phase forms first and freezes rather than the direct vapor-to-solid phase transition.

1.5.2.2.2. Heterogeneous nucleation

Heterogeneous nucleation is more common than homogeneous nucleation due to its smaller free energy barrier, hence it is far more technically significant. Unlike homogeneous nucleation

theory, heterogeneous nucleation theory has much more difficulty to relate with the experimental observation. Main difficulty comes from how to characterize the surface and its specific features which facilitate nucleation. Though extensive amount of research material is available in the literature, strictly speaking, existing theories are more of a basis to synthesize qualitative ideas and frame of reference for further studies rather than a basis for quantitative assessment of heterogeneous ice nucleation.

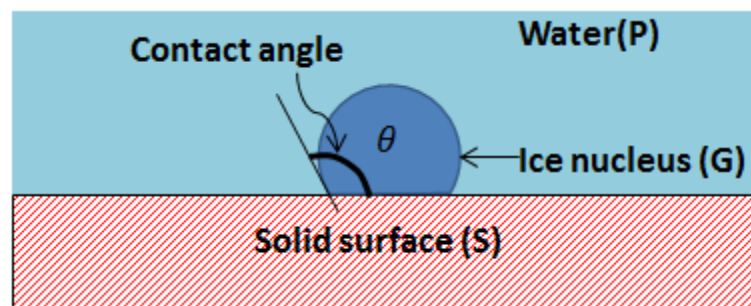


Figure 8: Spherical ice nucleus on a solid surface and submerged in water phase.

The fundamental formulation of heterogeneous nucleation is being derived from the phenomena of wettability, as reflected by the contact angle (Fig.8) of the spherical nucleus on an insoluble solid surface. This contact angle is related to the three interfacial surface energies σ_{SP} , σ_{SG} , σ_{GP} . Heterogeneous nucleation occurs at preferential sites for such phase boundaries, like dust impurities. At such preferential sites, due to low effective surface energies, free energy barrier for nucleation is decreased and thus facilitates nucleation. Though mainly developed for liquid condensation, this model can be easily extended to model solid nucleation from the liquid state. In the simplest formulation of nucleation in terms of spherical nucleus shapes, the critical radius is a sufficient criterion for nucleation with a nucleus of spherical cap shape (as illustrated above). Apart from the free-energy term, the geometry can also modify the pre-exponential term, but in a much less sensitive way.

The free energy needed for heterogeneous nucleation is equal to the product of homogeneous nucleation and a function of the contact angle θ

$$\Delta G_{heterogeneous} = \Delta G_{homogeneous} * f(\theta) \dots\dots\dots(17)$$

where $f(\theta) = (2 + \cos \theta)(1 - \cos \theta)^2 / 4$.

Compared to homogeneous nucleation, the degree of supercooling required for heterogeneous nucleation is reduced because of the lower free energy barrier. The contact angle increases the ease of nucleation by lowering the required energy. The critical radius in heterogeneous nucleation remains same as that of the homogeneous case, as shown in Fig. 9.

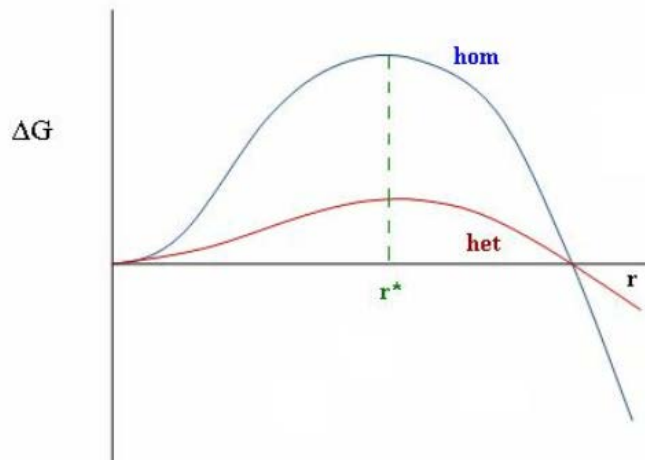


Figure 9: Comparison of Gibbs free energy variation with roughness between homogeneous and heterogeneous nucleation.

1.5.2.2.1. Rate of heterogeneous nucleation

The nucleation rate J depends on the average number of critical clusters, n^* and the diffusion of molecules to the cluster, β

$$J = n^* \beta , \quad \text{where } n^* = N \exp \left[\frac{\Delta G^*}{k_B T} \right] \dots\dots\dots(18)$$

Here ΔG^* is the critical free energy, N the number of potential nucleation sites per unit volume, and k_B is the Boltzmann constant.

The number of nuclei of a specific size formed is a function of the total number of atoms, the free energy to create a nucleus of that particular size, and the temperature.

Using the Volmer-Weber theory^[55], the rate of addition of one extra atom to the critical nucleus is estimated as

$$B = A \exp \left[-\frac{(Q+\Delta G^*)}{k_B T} \right] \dots\dots\dots(19)$$

Here A is a term which accommodates atomistic parameters, and Q the activation energy for atomic migration. This term describes the diffusion of the atoms to the site of nucleation. The rate of nucleation can be expressed as

$$J(T) = A. \exp \left[\frac{-Q}{k_B T} - \frac{16\pi\gamma_{sl}^3}{3\Delta H_s^2} \frac{1}{k_B T} \frac{T_m^2}{\Delta T^2} f(\theta) \right] \dots\dots\dots(20)$$

where γ is the surface tension, ΔH_s the enthalpy per unit volume, T_m the melting point, and θ the wetting angle. When temperature is very low, diffusion is very slow as the molecules are in a low energy state and do not have enough energy to move around and nucleate. The rate of diffusion process increases with temperature and molecules are then able to get to the site of nucleation at a fast enough rate to promote growth of the formed nucleus.

The time required for steady state nucleation is known as the time-lag and can be found by^[56]

$$\tau = \frac{16h}{\pi} \frac{\sigma}{\Delta G_s^2 a^4} \exp \left[\frac{\Delta G}{k_B T} \right] \dots\dots\dots(21)$$

Here a is the average particle size; the other terms have already been defined above.

1.5.3. Superhydrophobic surface as icephobic surface

Due to the high degree of water repellency, superhydrophobic self-cleaning surfaces are expected to have superior icephobic properties. Several experimental works^[28,29,57,58,59] have studied the performance of superhydrophobic surfaces as icephobic surfaces. Superhydrophobic surfaces showed both positive and negative results, hence a detailed understanding^[60] of ice formation on such surfaces is prerequisite for incorporating such surfaces in practical applications. Atmospheric ice forms on surfaces through various mechanisms, such as from supercool water droplets, condensation and freezing and frost formation due to sublimation of water vapor present

in the atmosphere. Since superhydrophobic surfaces have micro-nano surface features, heterogeneous nucleation is relevant to the icephobic properties of those surfaces. Proper understanding on how surface roughness features and length scale of micro-nano hierarchical structure influence the icing process -particularly the delay time of ice nucleation- has still not been investigated adequately. Report on the icephobic properties of superhydrophobic based on the surface heating is very limited. [61] Similar performance analysis of electrically conductive composites via resistive skin heating is also not available in literature. Chapter 3 attempts to address some of these issues by studying both electrically conductive and non-conductive superhydrophobic nanocomposite surfaces under icing conditions.

1.5.4. Electromagnetic wave shielding

Electromagnetic (EM) wave is nothing but a form of energy emitted and absorbed by charged particles. EM waves always have one electrical field (E) component and a magnetic field (B) component, which remain perpendicular to each other and in phase with each other, as depicted in figure below.

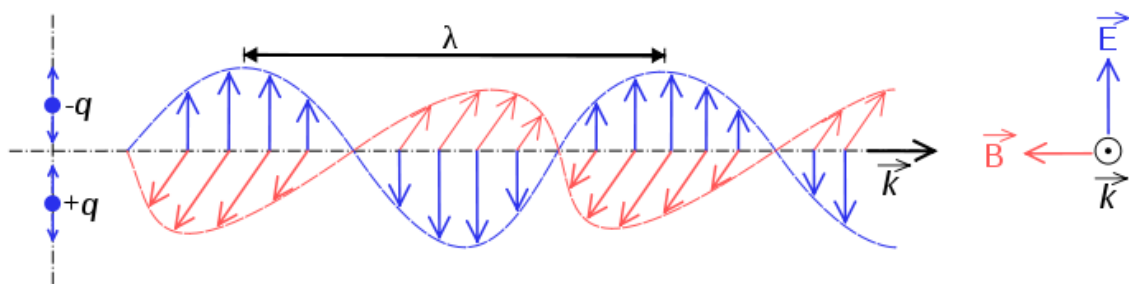


Figure 10: Electrical (blue) and magnetic (red) components of an electromagnetic wave

These two components of the EM field always maintain a fixed ratio and travel in the same direction as the wave. EM waves are classified according to frequency. The electromagnetic waves, in order of increasing frequency and decreasing wavelength, consist of radio waves, microwaves, infrared radiation, visible light, ultraviolet radiation, X-rays and gamma rays.

Electromagnetic waves, when interacting with electronic instruments, can hinder their performance. To avoid this situation, electromagnetic wave interference shielding is required. Electromagnetic shielding is the process of reducing the electromagnetic field in a designated space by blocking the field with barriers made of conductive or magnetic materials. Shielding is typically applied to enclosures to isolate electrical devices from the 'outside world', and to cables to isolate wires from the environment through which the cable runs. The shielding can reduce the coupling of waves, i.e. between electromagnetic and electrostatic fields. The amount of reduction depends very much upon the material used, its conductivity, thickness, the size of the shielded volume, the frequency of the fields of interest and the size, shape and orientation of apertures in a shield to an incident electromagnetic field.

Three mechanisms involved in EMI shielding are reflection, absorption and internal reflections.^[62,63] For reflection-dominated shielding, the shielding material must have mobile charge carriers (electrons or holes) to interact with the incoming EM waves^[63]. In the case of composite materials, EMI shielding increases with a rise in the composite's electrical conductivity. Absorption is the second shielding mechanism, which is enhanced when the shielding material having electrical or magnetic dipoles interacts with the EM waves.^[62,63] Shielding by multiple reflection mechanisms represents the internal reflections within the shielding material and has negative influence. Skin depth is one of the important parameters to understand the shielding property of a material and is defined as the depth into the conductive material at which the electric field drops to (1/e) of the incident value. Skin depth is given by^[63]

$$\delta = \frac{1}{\sqrt{(\pi f \mu \rho)}}, \text{ here } \mu = \mu_0 \mu_r \dots\dots\dots(22)$$

where δ is the skin depth, f is the frequency, μ the magnetic permeability, $\mu_0 = 4\pi \cdot 10^{-7}$ H/m, μ_r is the relative magnetic permeability and ρ the electrical conductivity. Materials having both higher electrical conductivity as well as higher magnetic permeability (known as ferromagnetic

materials) are expected to have smaller skin depth than materials of similar conductivities. For example, ferromagnetic Nickel has smaller skin depth of 0.47 μm compared to 2.09 μm of copper (non-magnetic). Skin depth also indicates that high specific surface area materials should have superior shielding properties. To quantify the shielding performance of materials, the term Shielding Effectiveness (SE) was defined as follows,

$$SE = -10 \log(P_1/P_2) \dots\dots\dots(23)$$

where P₁ and P₂ are transmitted power and incident power from the incoming electromagnetic wave.

1.5.4.1. Definition of S-parameter and measurement of SE

In order to measure the Shielding Effectiveness, the Scattering parameters or S parameters are used. The first published description of S parameters was in the thesis of Vitold Belevitch^[64,65] in 1945 and was named therein as repartition matrix. The name scattering matrix was used by physicist and engineer Robert Henry Dicke in 1947 who independently developed the idea during wartime work on radar.^[66,67]

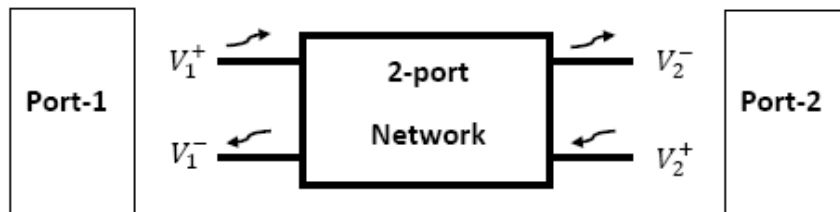


Figure 11: Two-port network defining the quantities used in the definition of the S-parameters

An electrical network to be described by S parameters may have any number of ports. Ports are the points at which electrical signals either enter or exit the network. Ports are usually pairs of terminals with the requirement that the current into one terminal is equal to the current leaving the

other. ^[68,69] S parameters are used at frequencies where the ports are often coaxial or waveguide connections. For a two-port network (Fig. 11), the incident (+) and reflected (-) waves at ports 1 and 2 are related through,

$$\begin{bmatrix} V_1^- \\ V_2^- \end{bmatrix} = \begin{bmatrix} S_{11} & S_{12} \\ S_{21} & S_{22} \end{bmatrix} \begin{bmatrix} V_1^+ \\ V_2^+ \end{bmatrix} \dots\dots\dots(24)$$

where the matrix elements are the S parameters. When the two-port network is connected so that V_1^+ and V_2^+ are incident signals reaching ports 1 and 2, respectively, the S parameters measure the reflected signals $S_{11} = V_1^- / V_1^+$ and $S_{22} = V_2^- / V_2^+$, as well as the transmitted signals $S_{12} = V_1^- / V_2^+$ and $S_{21} = V_2^- / V_1^+$.

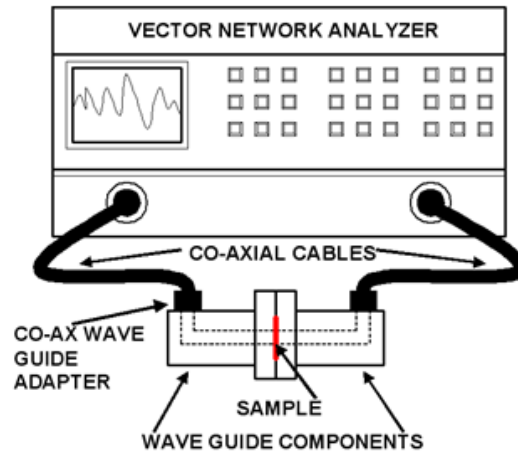


Figure 12: Experimental setup implementing the schematic of Fig. 11. The coating sample (red) is fully encased at the coupling of the two waveguides, to ensure minimal outside interference.

Using the experimental setup shown in Fig. 12, the measurement of the S parameters provides information on the shielding effectiveness of the coatings investigated in the present study. Specifically, the incident signal comes from port 1 of the vector network analyzer and the portion of this signal that is reflected back is used to determine S11, while the portion of the incident

signal that is transmitted through the material and appears at port 2 is used to determine S₂₁. Both S₁₁ and S₂₁ are expressed in decibels (dB), in order to comply with the following equation for the shielding effectiveness,

$$SE = 20 \text{ Log } \left| \frac{V_2^-}{V_1^+} \right| = 20 \text{ Log } |S_{21}| \dots\dots\dots(25)$$

For good shielding effectiveness, highly electrically conductive materials are required. Usually thin metal sheets are used for shielding. But due to low corrosion resistance and other difficulties associated with metals, conductive particle filled polymer composites are investigated extensively for this purpose. The literature is full of studies where different filler materials ranging from metal fibers, magnetic materials, conductive carbon materials, conductive polymers were used to produce thick shielding materials (1mm-4mm) and their shielding performance was characterized mostly in EM wave frequencies, i.e. less than or equal to 12.4 GHz. Extensive review articles are available^[34,35,62,63] in the literature on EMI properties of different nanocomposite materials based on different filler materials at different wave frequencies and sample thicknesses. Carbon based materials were also studied as possible fillers in shielding materials. Because of their reduced corrosion properties and high electrical conductivity and high aspect ratio, Carbon Nanofibers (CNFs) are promising candidates as fillers for thin low weight flexible shielding materials. Polymer nanocomposites made of these CNFs are expected to have higher value of shielding effectiveness even at smaller thicknesses.

1.6. Thesis objectives

The main objective of this thesis is to characterize and evaluate the performance of several nanoparticle-based multifunctional polymer nanocomposites, synthesized through a scalable process. A fundamental investigation is also carried out to understand the different properties and measure the performance of these composites. In addition to polymer nanocomposites, this thesis also studies a synthesis technique to produce a specific nanohybrid material based on nanoparticle

filled carbon nanofibers. The motivation of the different studied topics has already been discussed. In the following subsections, the specific objectives of each of these individual projects are summarized.

1.6.1. Polymer nanocomposite surface of extreme wettability and applications

- To synthesize polymer nanocomposites of extreme wettability.
- To synthesize extremely non-wettable surfaces or superhydrophobic surfaces of different roughness and to evaluate their performance as ice-phobic materials by measuring delay times associated with ice nucleation from super-cooled liquid water.
- To synthesize superhydrophobic surfaces of high electrical conductivity.
- To study the ice-phobic properties of electrically conductive superhydrophobic surfaces with the application of active joule heating.

1.6.2. EMI shielding properties of multifunctional conductive polymer-nanocomposites in GHz and THz frequency domain

- To synthesize multifunctional polymer nanocomposites having both superhydrophobic self-cleaning property as well as tunable electrical conductivity.
- To evaluate the EMI shield effectiveness of these composites in GHz and THz frequencies.
- To evaluate the effect of conductive filler loading and conductive filler's specific surface area on electrical conductivity and shielding effectiveness.

1.6.3. Superoleophobic surface from ink like dispersion of carbon nanofibers

- To synthesize an ink like dispersion of high aspect ratio carbonaceous nanoparticle.
- To synthesize highly electrically conductive superoleophobic surfaces having not only very high oil droplet contact angle but also roll off angle less than 10°.

- To study the effect of underlying substrate roughness on oleophobicity and hydrophobicity of conformal coatings prepared by spray deposition of CNF based inks.
- To ink jet carbon nanoparticle base ink and make a device with this method.
- To study the feasibility of a THz polarizer based on inkjetted and micro patterned conductive polymer nanocomposite.

1.6.4. Synthesis and characterization of a nanohybrid material based on magnetic

nanoparticle filled carbon nanofibers

- To synthesize a nanohybrid material by intercalating magnetic nanoparticles inside hollow carbon nanofibers by employing an ultrasonication-assisted, concentration-gradient-driven filling procedure.
- To evaluate the effect of process parameters, such as carbon nanofiber-nanoparticle concentration, sonication type, sonication time etc. on filling efficiency and quality.
- To synthesize thin polymer nanocomposite films of highly anisotropic properties by orienting magnetically active filled CNFs under a strong magnetic field.
- To use filled CNFs as magnetically-active, conductive filler in polymer composite films and to study the feasibility of those nanocomposites as electro-magnetically tunable EMI shielding material.

2. POLYMER NANOCOMPOSITE COATINGS OF EXTREME WETTABILITY: SYNTHESIS, CHARACTERIZATION AND APPLICATION

2.1. Introduction

Composite coatings based on polymers (as matrix or binder) and nanoparticles (as filler materials) are known as polymer nanocomposites. According to the type and the amount of nanoparticle fillers, nanocomposites can show different functional properties with wide range of tunability. Surface texture/morphology is one of such important surface characteristic. This surface morphology, in addition to the surface energies of both the nanoparticle and polymer, can greatly affect the wettability characteristics of the composite surface. Untextured surfaces are either hydrophobic or hydrophilic based upon the contact angle of water/liquid on those surfaces. Choice of nanoparticle with proper surface energy and the resulting surface texture of the composite surface can facilitate extreme wettability. On one extreme, surfaces may have very high liquid contact angle (superhydrophobic); on the other extreme, surfaces may be easily wettable by the liquids (superhydrophilic). In the introduction chapter, the theoretical background of surface wettability has been discussed in detail.

Nature has always motivated humans to inquire about many of its unique phenomena and in that process helped to produce scientific understanding behind those observations. Surfaces of extreme wettability are not an exception to this pursuit. Many natural surfaces, both plant and animal, have surfaces of extreme wettability. Thorough scientific inspection of such surfaces has provided very useful scientific information to synthesize such surfaces artificially and understand the underlying physics of their functionalities. These surfaces^[43, 70-75] usually have specific functions in respective plants or animals, which motivates the scientific community to achieve similar functionalities via synthetic surfaces of similar morphology and characteristics.

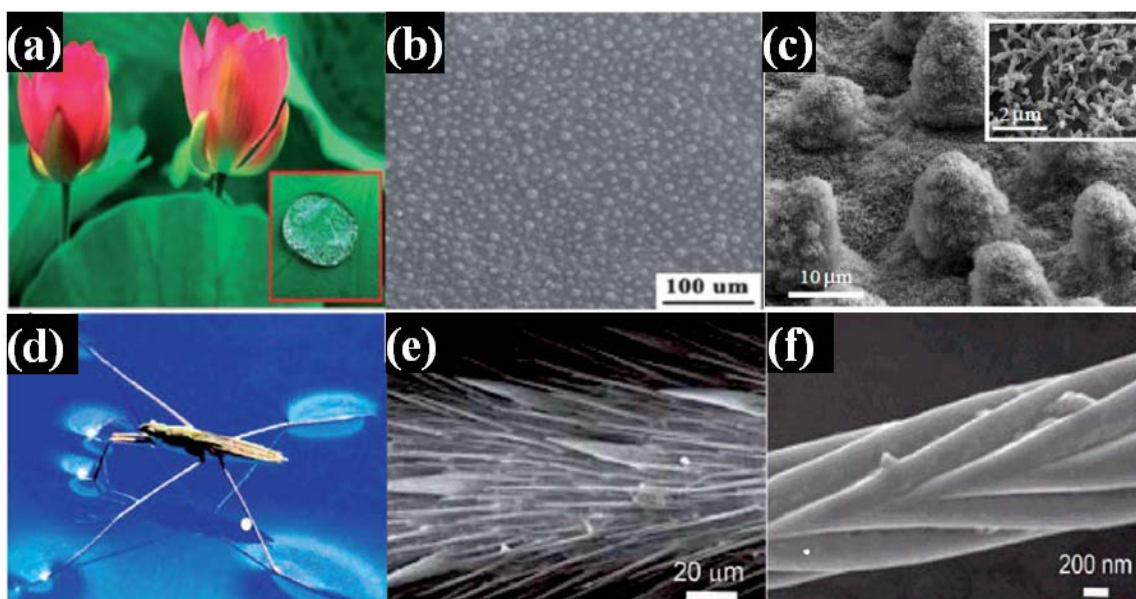


Figure 13: Natural superhydrophobic surfaces of (a) Lotus leaf and (d) Water strider. SEM images of (b) ,(c) lotus leaf and (e),(f) Water strider at different magnifications. Images a and b were adapted from references 79 (reproduced by permission of AIP). Image c was adapted from reference 75 by permission of the Royal Society. Images d, e, f were adapted from reference 78 (reproduced by permission of ACS).

Natural surfaces like lotus leaf,^[44] wings of insects,^[76] legs of water striders,^[77, 78] are some of the surfaces which show extreme water repellency with water contact angle exceeding 150° . Figure 13 shows two such natural surfaces using Scanning Electron Microscopic (SEM) images. On the other hand, superhydrophilic surfaces are observed in many water plants, mosses and in superhydrophilic leaves of *Ruellia devosiana*.^[75] Open air superoleophilic/underwater superoleophobic surfaces are observed in various carps.^[80] Figure 14 shows SEM images of some naturally occurring superhydrophilic surfaces. Patterned surfaces with superhydrophilic and hydrophobic zones were also observed in nature. Beetles of Namib desert (see Figure 15.a, b,c) have such patterned surfaces, which helps them to collect water from fog.^[81] All of these surfaces have shown hierarchical micro/nano surface morphologies under the electron microscope being composed of micro-nano scale bumps, pores, nanoscale hairs and other geometrical features.

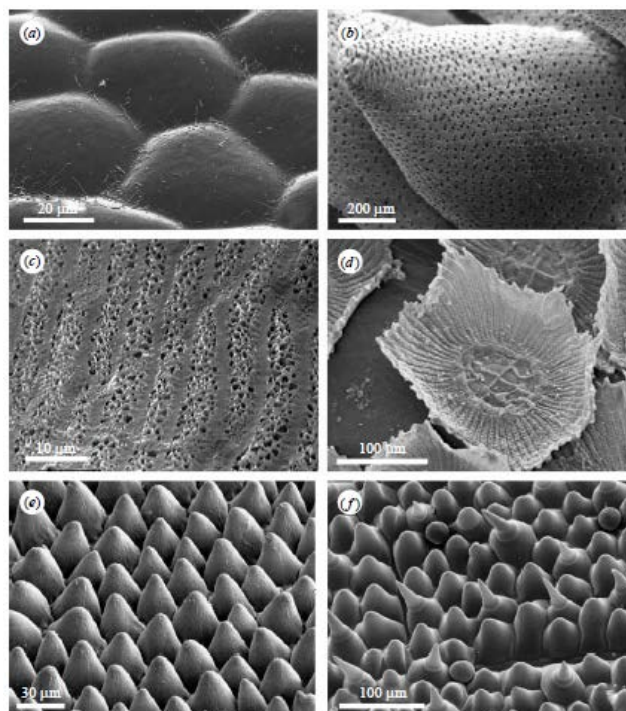


Figure 14: Scanning Electron Microscope images of superhydrophilic plant surfaces of (a) the water plant (*Anubias barteri*), (b) water-adsorbing moss (*Sphagnum squarrosum*) (c) water-adsorbing moss *Rhacocarpus purpurescens* (d) the Spanish moss (*Tillandsia usneoides*) (e) The leaf of *Calathea zebrina* (f) the superhydrophilic leaves of *Ruellia devosiana*. Images reproduced from reference 75 by permission of the Royal Society.



Figure 15: Naturally occurring patterned wettable surface of (a) of Namib desert beetle (elytra), Scale bar is 10 mm, (b) wax free hydrophilic zone in waxy superhydrophobic background, (c) scanning electron micrograph of the textured surface of the depressed areas. Scale bars are, respectively, 10 mm, 0.2 mm and 10 μm . Reprinted by permission from Macmillan Publishers Ltd: Nature,^[81] copyright 2001.

The technical potential ^[43, 70- 74] of these natural surfaces has prompted researchers to synthesize artificial surfaces of similar properties, through approaches ^[82] used in micro/nano technology. Not only water-repellent, but also highly oil-repellent ^[83] and alcohol-repellent and omniphobic

^[84] surfaces have been synthesized. Nanocomposite surfaces due to their inherent hierarchical micro/nano surface morphology were already explored as one possible route of synthesizing surface of extreme wettabilities. Most studies in the literature have used costly synthetic techniques (such as lithography, chemical reaction, CVD process etc.) which cannot be scaled up for practical applications. Synthesis of nanocomposite surfaces, via spray casting ^[27, 85-87] of nanoparticle-polymer dispersions is one such technique which can be scaled up for industrial scale production. ^[82]

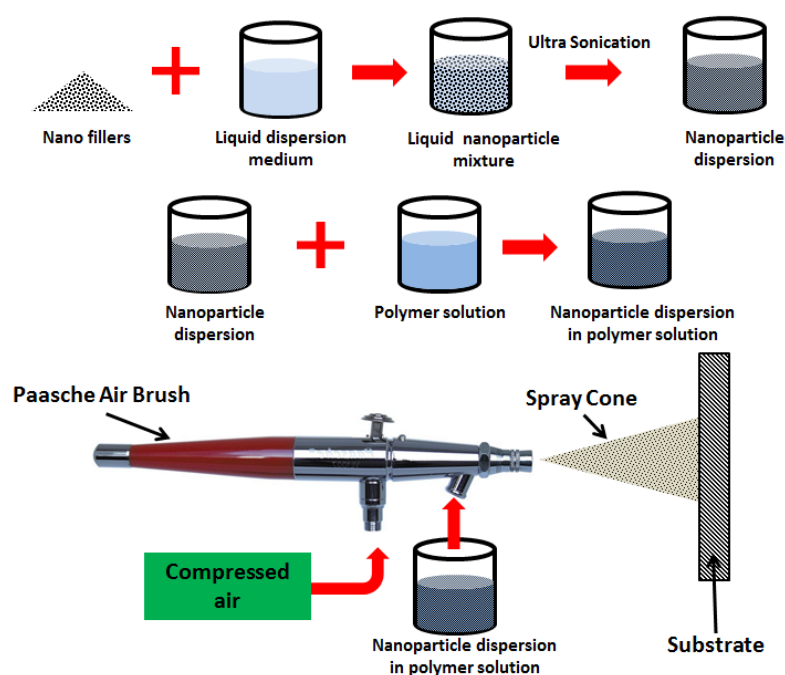


Figure 16: Schematic of spray casting process for applying polymer nanocomposite coatings on surfaces. All of the superhydrophobic composites were spray deposited by an air brush.

Figure 16 shows a schematic diagram of the synthesis process used to prepare the nanocomposite surfaces reported here. The present chapter reports few such surfaces with corresponding practical applications. The focus of this chapter is on application of superhydrophobic surfaces as icephobic (anti frost) materials.

2.2. Polymer nanocomposite coatings for anti-icing applications

Ice formation and accumulation is a common natural phenomenon which has severe effects in various human activities and infrastructure. Icing has adverse economic effects and safety issues related to aircraft, wind turbine, power grids, marine vessels, telecommunication devices, roads and transportation system, commercial and household refrigeration systems, etc.^[88 - 90] The problem of icing is very critical for the aircraft industry, wind turbine operation and power grid cables. The safety and performance of modern aircraft is significantly reduced even by light, scarcely visible ice on airfoils, compression inlets of air-breathing engines and air flow measurement instruments. Aircraft icing mainly happens during the holding time of around 4 min^[91] before landing, when supercooled water droplets (0–500 μm diameter)^[88, 92] impact on the surface. Since supercool water is in a metastable state, these droplets when colliding with the much cooler skin of the aircraft, they instantly freeze. Due to their practical significance, considerable amount of effort has been expended to develop surfaces that facilitate the efficient removal of ice or retard its formation. Extensive research on superhydrophobic surfaces indicates anti-icing behavior for such surfaces.^[28, 93] In those studies, freezing has been studied for room temperature droplets placed upon sub-freezing surfaces,^[93, 94] or supercooled water poured onto surfaces.^[28] However, in actual situations, the impact and accumulation of supercooled droplets on surfaces is a common and important mechanism of ice formation. Such mechanism has not been investigated yet and thus lacks a thorough fundamental understanding.^[95, 96]

Prior work^[97] investigated delayed freezing of inkjet-generated supercooled water microdroplets (accumulating one after the other) on various surfaces, including PTFE based superhydrophobic coatings, and ultra-smooth hydrophilic surfaces. The results revealed that target surface roughness has a dominant effect on ice nucleation, nuclei growth and freezing delay statistics compared to the presence of the superhydrophobic texture itself. Delay in icing of supercooled liquid droplets (-20°C) observed for some of the superhydrophobic surfaces (kept at -20°C) was

moderate and have values as high as 70 sec. Owing to very small roll off angles on these superhydrophobic coatings, the expected time for water droplets to roll off from the surface is much less than 70 sec under dynamic conditions. Hence, icing delays on these surfaces are expected to decrease ice accumulation. Moreover superhydrophobic surfaces with nanometer scale roughness are also expected to delay ice formation further. ^[28]

A significant amount of knowledge base has been developed on the use of bio inspired superhydrophobic self-cleaning surfaces as possible means for ice prevention. ^[28, 29, 57, 59, 60, 94, 97-100] Some alternate ways, like liquid infused *slip* surfaces, have also been proposed. ^[100] Except for few, ^[61, 101] all of the icephobic works have focused on the passive aspect of these surfaces to address the icing problem. The icephobicity there relied on the delay of ice nucleation via controlling the surface texture and wettability. Reduced heat transfer rate due to very low solid-liquid contact area on superhydrophobic surfaces, is another mechanism which helps in delaying ice nucleation under static condition. Under dynamic conditions, when the liquid droplet contact time with the self-cleaning surface is less than the freezing delay time, this renders the surface icephobic. ^[59, 102] Despite their significance and necessity, most advanced icephobic surfaces are still not optimal as far as performance is concerned. Superhydrophobic surfaces have been shown to retain their properties even down to -30°C at low humidity condition, ^[28, 29, 94] but fail to achieve the same under high humidity condition, ^[103] thus leading to high energy consumption ^[57, 99, 104] when removing the ice. Even just below -5°C and RH higher than 50%, significant accumulation of ice/frost occurs on the surfaces. Even state of the art *slip* surfaces accumulate enough amount of frost after prolonged exposure to humid environment when held at just -2°C. Although passive means of ice control are important for studying the icephobic properties of various surfaces, active means are equally important. A few recent works ^[61, 101] have used heating to remove or control accumulated ice/frost from the superhydrophobic surfaces. Either regular electrical panel heater or strip heaters were used in these works. To address the practical

icing problem (e.g aircraft icing), it is very crucial to achieve very fast response from the coatings in active mode since most of the ice accumulation occurs within 4 to 10 minutes before landing. To minimize the energy consumption and to achieve fast response time, application of skin heating seems to be an optimal choice. Though several publications have appeared on synthesizing superhydrophobic self-cleaning surfaces of higher electrical conductivities,^[105, 106] their icephobic properties were not explored. To the best of our knowledge, no study so far has been reported using skin heating of electrically conductive superhydrophobic (or any other icephobic) surface as means of active ice control. To achieve this goal, we report synthesis process of two different types of highly electrically conductive multifunctional polymer nanocomposite surfaces, also having superhydrophobic and self-cleaning properties. These surfaces comprise either a fluoro acrylic polymer (PMC) or PVDF-PMMA (60:40 weight ratio) blend as the matrix. PTFE nanoparticles and/or heat-treated carbon nanofibers were used as filler. High values of electrical conductivities were obtained in these composites. These surfaces were prepared via spray casting of filler-polymer dispersions. Compared to metallic surfaces and other costly superhydrophobic surfaces, these spray coated surfaces have several advantages. Firstly, these are made of polymer matrix which makes them flexible and easy to conform to surfaces of moderate complexity. Secondly, the synthesis process of these composites also makes them very inexpensive. Unlike other lithographically prepared surfaces, these surfaces also can be scaled up for industrial applications. Another advantage of these surfaces is that treated surfaces can be re-coated to get their lost hydrophobic properties back, if coatings are damaged during use. This is not possible with lithographically prepared self-cleaning surfaces. These composite surfaces with different polymer to CNF ratios were synthesized to evaluate their anti-frost and ice-phobic performance. The surfaces showed excellent electro-thermal as well as superhydrophobic self-cleaning properties even at subfreezing temperatures. Experiments were carried with skin heating and initial experiments show promising results for practical applications. Comparison of energy

expended on these surfaces to make them ice-free, clearly shows the ability of skin-heated superhydrophobic surfaces to bring down the energy cost significantly.

2.3. Passive icephobic properties of PTFE based superhydrophobic surfaces

2.3.1. Materials and method

Superhydrophobic surfaces:

Five superhydrophobic surfaces (samples 1-5, contact angles $\sim 150^\circ$) were produced by coating aluminum plates with polymer-based, large-area, water repellent coatings.^[27, 85, 107] The polymer matrix of the coatings was a mixture of Poly (methyl methacrylate) (PMMA, MW-9,96,000 from Sigma Aldrich) and Poly (vinylidene fluoride) (PVDF, MW-5,36,000 from Sigma Aldrich) with 2:3 mass ratio. Hydrophobic Poly- tetrafluoroethylene (PTFE, from Sigma Aldrich) particles of 260 ± 54 nm were added to the mixture and subsequently sprayed by a Paasche air brush to create a texture that induces superhydrophobicity. These five samples were prepared using three different types of coating formulation (varying PTFE particle wt%) and two different types of substrate surfaces. The coatings of samples 1–3 were applied on sand-blasted (“sb”) aluminum plates. The remaining two (samples 4 and 5) were applied on smooth aluminum plates. Initially PTFE particles were dispersed in acetone via bath sonication process of 10 minutes. To prepare the polymer blend of PVDF and PMMA, 10wt. % solution of PMMA in acetone and 20wt% solution of PVDF in DMF were used.

Aluminum (control) surfaces:

The reference samples 6 and 7 were the uncoated aluminum backsides of samples 4 and 3 (smooth and sandblasted, respectively). The smooth Al surface (sample 6) was moderately hydrophobic (contact angle 92°), while the sand blasted Al surface was even more hydrophobic (CA 124°).

Ultra-smooth surfaces:

These included one untreated silicon wafer (sample 8) and two different post-treated silicon wafer surfaces (samples 9, 10). Sample 8 was hydrophilic (contact angle 36°), as was sample 9 (CA 46°), while sample 10 was moderately hydrophobic (CA 88°).

2.3.2. Surface characterization

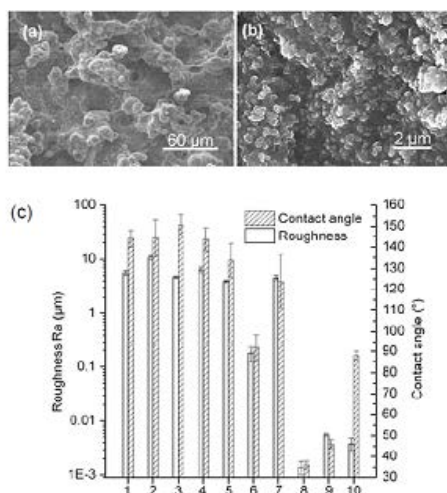


Figure 17: (a), (b) Scanning electron micrographs of a superhydrophobic coating (sample 2) studied in ref. 97, (c) Average roughness values Ra (DIN 4768) and advancing contact angles θ for selected surfaces studied in the same reference.

Surface morphology was evaluated by scanning electron microscopy (SEM); see example in Fig. 17.(a),(b) for sample 2 (CA 144°) which reveal typical hierarchical micro-to-nanoscale texture, a necessary requirement for high liquid repellency. Advancing water contact angles were measured by collaborators in Switzerland (Poulikakos et. al) ^[97] using drop shape analysis with a computer controlled liquid dispensing system. The advancing contact angles were recorded during expansion of droplets from 3- μ L to 5- μ L volume by continuously dispensing water through a needle (0.5 mm-dia.). Each contact angle measurement was repeated five times on five different locations on each sample plate at an ambient temperature of 21°C and a relative humidity of 60%. Roughness measurements were carried out by collaborators in Switzerland

(Poulikakos et. al) ^[97] using a stylus profilometer (diamond tip radius $2.5\mu\text{m}$) and, for the very smooth surfaces, an Atomic Force Microscope AFM (contact mode). The roughness values R_a , i.e. the arithmetic average of the roughness profile for each surface, are also plotted in Fig. 17(c).

2.3.3. Experimental setup

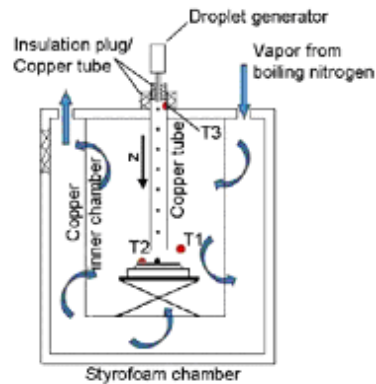


Figure 18: Schematic drawing of the setup showing flow of nitrogen gas (blue arrows) and thermocouples T1-T3 (red dots). This setup is available at the Swiss Federal Institute of Technology where these measurements were performed.^[97]

A cryogenic cooler was used to cool down a Styrofoam chamber. As shown in Fig.18, a separate inner test chamber was made with 1mm thick copper plate, which is separated from the outer chamber with a 5-mm gap. The cool nitrogen gas was led through the outer chamber and bled into the inner chamber through the gap. Visual access was made through a sidewall observation window, using a CCD Camera mounted on a binocular microscope. A piezoelectric jetting device (60- μm orifice diameter) was used to generate droplets (50–80 μm -dia.) at a rate of 80 Hz. The jetting device was mounted onto the 40-cm long copper tube that extended into the chamber (Fig. 18). The length of the copper tube was chosen in such a way to make sure the temperature of the droplets reaches -20°C , before impacting the surface of same temperature. The test samples were cooled by the flowing nitrogen gas. Droplets continuously impinged, one upon the other, onto the same sample location, so as to form, by successive coalescence, a growing sessile droplet until freezing occurred. Freezing delay times were defined as the time between the

first droplet impact and the onset of freezing, as determined by direct imaging through the microscope. These freezing delays were used to evaluate ice phobic behavior for each target surface.

2.3.4. Results: Freezing delay

Inkjet deposited droplets landed within an area of 300–500 μm across and coalesced into a single growing droplet before eventually freezing. Figure 19a shows a box plot of the time until freezing on each surface, based on a minimum of 20 data points per sample plate. Figure 19.b illustrates the concept of the box plot based on data obtained using sample 7. The results in Fig. 19.a show that all surfaces exhibited delayed freezing compared to the two untreated reference surfaces (6 and 7), as based on the median values of freezing delay. It is clear that samples 8-10 performed best; for example, on the “8_Wafer_Si” surface, droplets remained liquid 150 times longer (median values) than on “6_Ref_AL”. These three surfaces (8-10) were also the smoothest (average roughness 1.4, 3.8, and 5.6 nm, respectively).

For roughness comparable to, or smaller than the critical ice nucleus radius, freezing is predicted to be significantly delayed.^[94] The critical ice nucleus radius is the minimum size an incipient ice crystal needs to reach, in order to maintain a stable freezing process. For a water temperature of -20 °C, the radius of the critical nucleus r_c was 2.2 nm, as calculated from^[108] $r_c = 2\gamma_{IW} / \Delta G_{f,v}$,

where γ_{IW} is the water-ice interfacial tension (23 mJ/m²) and $\Delta G_{f,v} = \frac{\Delta H_{f,v}(T_m - T)}{T_m} = 21$

MJ/m³ is the volumetric free energy of bulk ice vs. bulk liquid, which follows from the Gibbs-Helmholtz equation; $\Delta H_{f,v} = 287$ MJ/m³ is the water volumetric enthalpy of fusion, $T = 253$ K (-20 °C) and $T_m = 273$ K (0 °C) (the ice melting temperature at one atmosphere). According to the above formulas, r_c for water at -20 °C is 2.2nm, in the same range as the roughness of samples 8-10, but three orders of magnitude smaller than the roughness of the hydrophobic samples 1-5 or

the reference surface “7_Ref_sb_AL”. Noting that samples 8-10 are either hydrophilic or moderately hydrophobic (Fig. 17.c), the freezing delays plotted in Fig. 19.a. indicate that under the present conditions, surface smoothness is more important for icephobicity than solid surface energy.

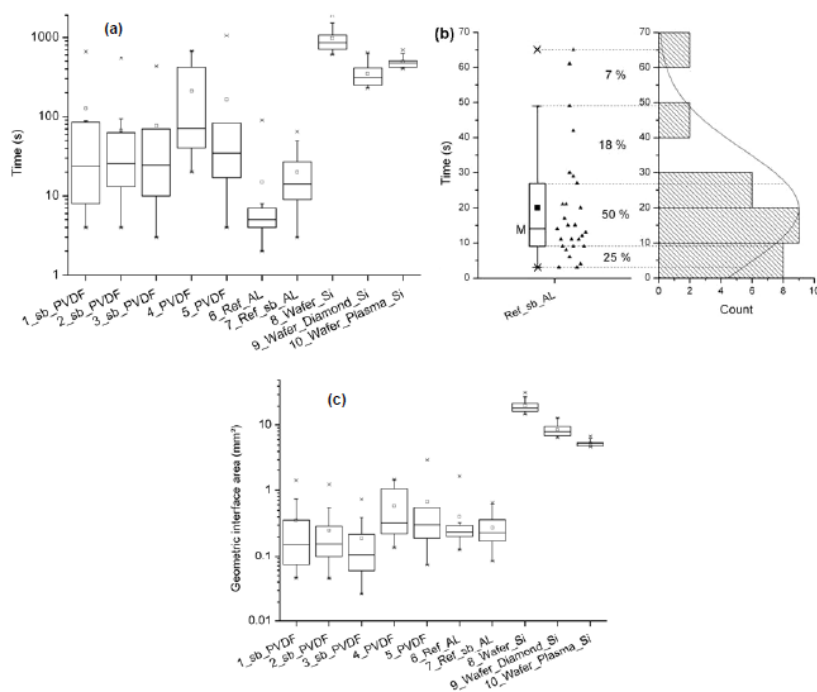


Figure 19. (a) Logarithmic box plot of the time to freezing (or freezing delay) of a growing (through successive impacts of ink-jetted droplets) sessile droplet on each of the ten surfaces considered^[97] in the experiments performed by our collaborators at ETH-Zurich. (b) Clarifying illustration of a (linear) box plot for the surface “7_Ref_sb_AL”, showing the time-to-freezing minimum and maximum (crosses), median (M), and the arithmetic mean (filled square). The middle 50% of the data distribution falls within the open box. The ends of the two “whiskers” extending from the box indicate the locations of the furthest non-outlier data points, (c) Geometric area^[97] of the liquid –solid interface at the onset of freezing for each surface.

2.3.5. Theoretical considerations

Although classical nucleation theory has been successful in explaining freezing statistics qualitatively, doubt has been cast over its quantitative predictability for heterogeneous

nucleation.^[109] According to the classical heterogeneous nucleation theory,^[108] the freezing probability depends not only on surface roughness R_a , but also on contact angle θ (i.e., wettability); the instantaneous rate at which critical nuclei are generated within the growing droplet is

$$J(\theta, R_a, t) = KA_{int}(\theta, t) \exp\left[-\frac{\Delta G_c(R_a, \theta_{IW})}{kT}\right] \dots\dots\dots(26)$$

where K , k are a kinetic constant and Boltzmann's constant, respectively, while A_{int} is the instantaneous liquid-solid contact area approximated^[97] by assuming the accumulated liquid mass to occupy a spherical section. A_{int} was found to vary as $\alpha t^{2/3}$, with α a function of θ . Thus,

$$J(\theta, R_a, t) = K\alpha(\theta)t^{2/3} \exp\left[-\frac{\Delta G_c(R_a, \theta_{IW})}{kT}\right] = J_0(R_a, \theta)t^{2/3} \dots\dots\dots(27)$$

The actual liquid-solid contact area cannot be accurately determined by measuring surface roughness.^[110] Particularly for superhydrophobic surfaces, where air micro-pockets are trapped underneath the liquid, the roughness cannot be used as a measure of the actual contact area. In the above expression of $J(\theta, t)$, $\Delta G_c(R_a, \theta_{IW})$ is the free energy barrier for formation of a critical sized nucleus, expressed in terms of average surface roughness and the ice/water contact angle θ_{IW} as,

$$\Delta G_c(R_a, \theta_{IW}) = \frac{16\pi\gamma_{IW}^3}{3\Delta G_{f,v}^2} f(R_a, \theta_{IW}) \dots\dots\dots(28),$$

where the wetting parameter f is,^[114]

$$f(R_a, \theta_{IW}) = \frac{1}{2} + \frac{1}{2}\left[\frac{1-mx}{g}\right]^3 + \frac{x^3}{2}\left[2 - 3\left(\frac{x-m}{g}\right) + \left(\frac{x-m}{g}\right)^3\right] + \frac{3}{2}mx^2\left(\frac{x-m}{g} - 1\right) \dots\dots\dots(29)$$

with $g=(1+x^2-2x\cos\theta_{IW})/2$ and $x=R_a/r_c$ (normalized length scale). It can be shown that for $x \leq O(1)$, $f(R_a, \theta_{IW}) \approx f(R_a)$, i.e. the freezing probability is predominantly determined by the roughness, whereas for $x \geq O(10)$, $f(R_a, \theta_{IW}) \approx f(\theta_{IW}) = [(2+\cos\theta_{IW})(1-\cos\theta_{IW})]/4$, i.e. the contact angle effect dominates.^[111] The contact angle θ_{IW} can be derived from Young's equation^[97]

assuming that $\theta_i = \theta$ (subscripts I, W indicate ice and water, respectively). Thus, $\cos \theta_{IW} = [(\gamma_I - \gamma_W) / \gamma_{IW}] \cos \theta$, where $\gamma_I |_{253K} \approx \gamma_I |_{273K} = 106 \text{ mJ/m}^2$, $\gamma_W |_{253K} = 78 \text{ mJ/m}^2$ and $\gamma_{IW} |_{253K} = 23 \text{ mJ/m}^2$.^[53, 112, 113] The relation between J and the median freezing delay time can be obtained from the probability density function for the time between events in the non-homogeneous Poisson process, yielding^[97]

$$t_{med}(R_a, \theta) = \left[\frac{5 \ln 2}{3 J_0(R_a, \theta)} \right]^{3/5} \dots \dots \dots (30)$$

Figure 20 shows median freezing delay times vs. contact angle θ (Fig. 20.a) and roughness R_a (Fig. 20.b). The data are separated according to roughness of the corresponding surface; for rough surfaces, $x \gg O(10)$, shown by closed symbols in Fig. 20.a, it is $f(R_a, \theta) \approx f(\theta)$, and thus the freezing delay time is independent of roughness. The model is fitted to the experimental freezing delay data $t_{med}(R_a, \theta)$ with K as the single fitting parameter; K is embedded in the expression of $J_0(R_a, \theta)$ in the above expression of t_{med} . The classical heterogeneous nucleation theory (using quantities corresponding to the actual temperature of 253K) is shown by Fitting curve 1 in Fig. 20.a and deviates significantly from the experimental data. A similar discrepancy was reported by Gorbunov et al.^[109] To remedy this, an extension to the classical theory had been formulated taking into account the reduction in excess entropy of water in the proximity of a surface, as compared to “bulk liquid”.^[114, 115] It is expected that the local fluid properties could be close to those of bulk water for temperature far below 253 K. This hypothesis was implemented in the classical nucleation theory by means of a lowered ice-water surface free energy. Based upon the property values of bulk water at 229 K, the enthalpy of fusion is $\Delta H_{f,v}$, the ice-water surface energy is γ_{IW} (much lower than the value at 253 K) and adjusted Young’s equation, new curves were plotted. The adjusted free energy values, based on the reduction of entropy within the hydration layer, affect the free energy barrier ΔG_c , which leads to a nucleation rate that better represents the experimental data (Fitting curve 2, Fig.20.a).

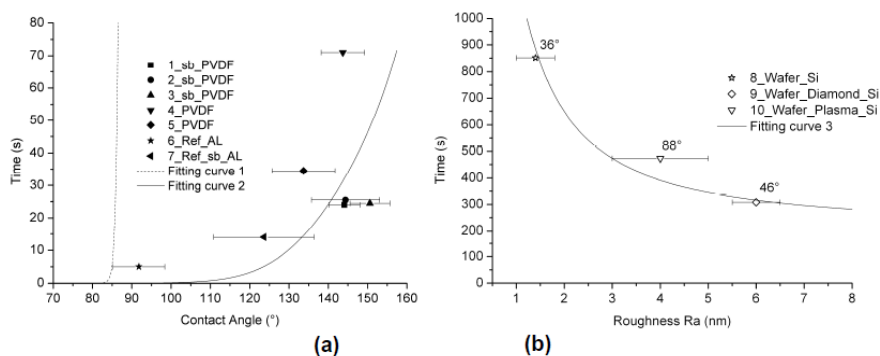


Figure 20. (a) Freezing delay time t_{med} (median values) vs. advancing contact angle for “highly” corrugated surfaces, $x \gg O(10)$. Contrary to the classical nucleation theory (Fitting curve 1), the extended model (Fitting curve 2) offers a better fit for the experimental data (symbols). (b) Freezing delay time (median values) vs. roughness for smooth surfaces, $x \leq O(10)$. The value beside each symbol indicates the measured contact angle of the respective surface. The extended model is indicated by Fitting curve 3. Excellent agreement between experiments and theory is apparent in both plots.

Figure 20.b shows the median freezing time vs. roughness with measured contact angle for the smooth surfaces $x \leq O(10)$. In order to illustrate the predominance of roughness on freezing probability for surface roughness close to the radius of the critical nucleus, the adjusted model (taking the corrected values of ΔG_c and r_c into account) is fitted to the data with the kinetic constant K and produces Fitting curve 3 in Fig. 20.b. This curve confirms the significant roughness dependency of freezing delay for very small values of R_a (samples 8-10). The results of Fig. 20 show good agreement between experiments and the extended classical nucleation theory, and reveal that ultra-smooth non-hydrophobic surfaces (samples 8-10) resist considerably longer against icing than typical hierarchical hydrophobic surfaces (samples 1-5).

2.4. Conductive superhydrophobic surfaces for active anti icing

2.4.1. PTFE-CNF-PVDF-PMMA conductive composite coatings

2.4.1.1. Materials and surface synthesis

Electrically conductive, nanocomposite surfaces of three different wettabilities were prepared by incorporating high heat treated carbon nanofibers (PR-24-XT-HHT CNF, Pyrograf III, Applied

Sciences, 40nm-100 nm diameter, length after sonication < 30 μ m) and PTFE nanoparticles (same as mentioned before) as filler either in PVDF-PMMA or in PMMA matrix. Initially two stock solutions of PVDF in DMF and PMMA in acetone were prepared. The concentration of polymers in both of these stock solutions is 10% by weight. The composite surfaces were prepared by spray casting nanoparticle-polymer dispersion on various substrates using a Paasche air brush. As initial step, the required amount of HHT CNFs and PTFE nanoparticles were added to a mixed solution of acetone and DMF. DMF weight concentration was kept at 20% in mixed solvent to prepare a surface with self-cleaning (S1) and moderately hysteretic property (roll-off angle 40°, S2). To prepare completely sticky surface (S3) the DMF concentration was changed to 30 wt% of mixed solvent. The total amount of mixed solvent was chosen in such a way, that the amount of HHT in mixed solvent is always 0.35 wt%. The ratio of CNF to PTFE particle was fixed at 1.1:5.76 to ensure high electrical conductivity.

The nanoparticle-solvent mixture was subsequently probe sonicated at 70% amplitude for 3 minutes in a probe sonicator (Sonics, Vibra-Cell, Model –VCX 750, 20 kHz, 750 watt). Subsequently, the required amount of polymer stock solution was added in the nanofiller dispersion followed by 30 sec of probe sonication at 30% amplitude for uniform mixing. The weight ratio of total polymer to CNF was kept fixed at 1:1.1. For the composite surface S1, both PVDF and PMMA stock solution were used and added in 60:40 weight ratio. For the other two surfaces, only PMMA solution was used. Well mixed nanoparticle polymer dispersion was then spray-casted on glass slides to form composite surfaces. Table 1 charts the wettability and electrical properties of these three surfaces.

Sample	Contact Angle (deg.)	Roll off angle (deg.)	Nano Filler	Polymer (matrix)	Solvents	Resistance (ohm)
S1	158±4	<10	CNF,PTFE	PVDF:PMMA 60:40	DMF:Acetone 20:80	404
S2	154±3	35-40	CNF,PTFE	PMMA	DMF:Acetone 20:80	265
S3	152±4	Sticky	CNF,PTFE	PMMA	DMF:Acetone 30:70	143

Table I: CONTACT ANGLE, ROLL-OFF ANGLE, COMPOSITION, SOLVENTS AND ELECTRICAL CONDUCTIVITY OF THREE CNF/PTFE COMPOSITES.

2.4.1.2. Surface morphology

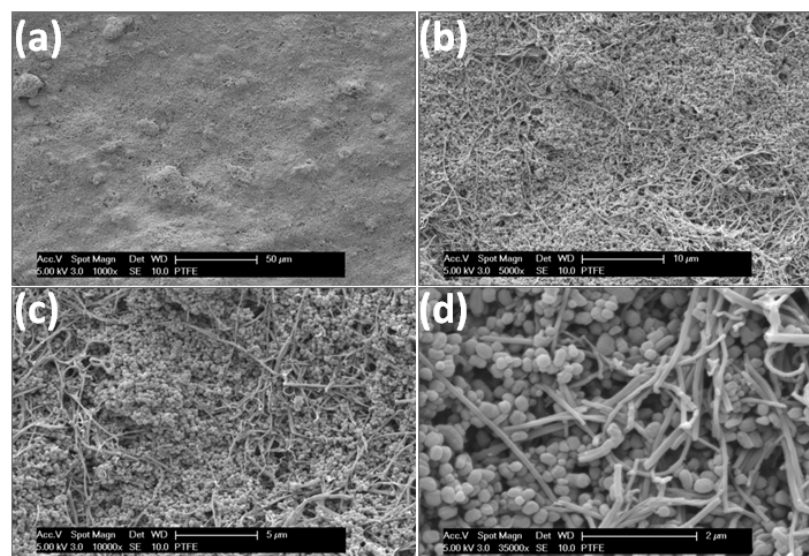


Figure 21: SEM images of CNF/PTFE/PVDF/PMMA coatings at (a) 1000× ; (b) 5000× ; (c) 10000× ; (d) 35000× magnifications.

Figure 21.a-d shows SEM images of the surface S1 at four different magnifications. As evident from these images, surface morphology comprises micro-nano hierarchical structures which were generated by spray process and the filler particles. The nanofeatures of this surface comprise of

spherical PTFE nanoparticle and cylindrical high aspect ratio CNFs. The distribution of nanoparticles and CNFs within the composites shows a high degree of uniformity even at the micro scale.

2.4.1.3. Electro-thermal characterization of composite coatings

Electrical resistance and conductivity of these three surfaces were measured by a Keithley 6517A electrometer. Using a Lab-View virtual instrument with this electrometer, I-V curve of these samples were generated. All composite surfaces show linear I-V curve, which indicates their Ohmic nature. Resistance of the samples was calculated based on these I-V curves. Figure 22 shows representative I-V curves of all three samples. Using an optical microscope, the average thickness of these coatings was estimated. Conductivity of the composite surfaces was calculated based on the thickness and resistance measurements. To show the skin heating capability of these surfaces, different voltages were applied across the two copper electrodes fixed at the two edges of coated glass slides. Temperature evolution of these surfaces under skin heating were recorded at -15°C and -30°C ambient temperature with 30% relative humidity and 2m/s air velocity inside an environmental chamber (see Fig. 24.a).

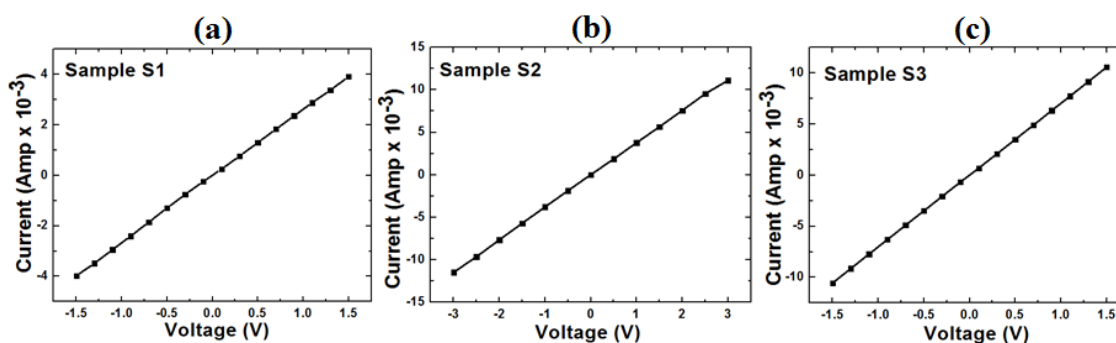


Figure 22: I-V curve of PTFE/CNF based (a) S1 (self-cleaning, roll-off angle $<10^{\circ}$), (b) S2 (high contact angle, roll-off angle $\sim 40^{\circ}$); (c) S3 (sticky) superhydrophobic nanocomposite surfaces.

The self-cleaning sample used for the temperature evolution experiments was thicker ($\sim 100 \mu\text{m}$), than sample S1 ($40 \mu\text{m}$) and had resistance of 55 ohm but with same wettability properties.

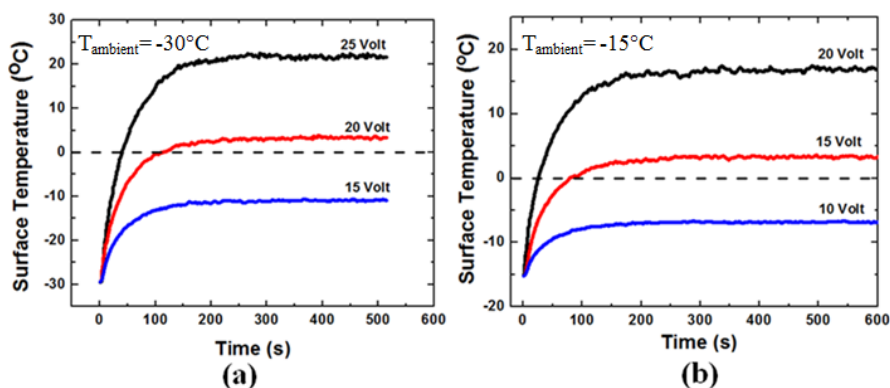


Figure 23: Surface temperature evolution of PTFE/CNF/PVDF/PMMA self-cleaning surface at (a) -30°C ; (b) -15°C ambient temperature at different voltages applied for skin heating. Relative humidity of 30% and air velocity of 2 m/s were maintained inside the chamber.

Figure 23 (a), (b) shows the temperature evolution curves of this self-cleaning sample at two ambient temperatures. All of the temperature evolution curves reach a specific steady state temperature depending upon the applied voltage and ambient temperature and air velocity. At steady state, the heat loss due to the convection process balances the heat generation rate due to applied voltage.

2.4.1.4. Icing experiment

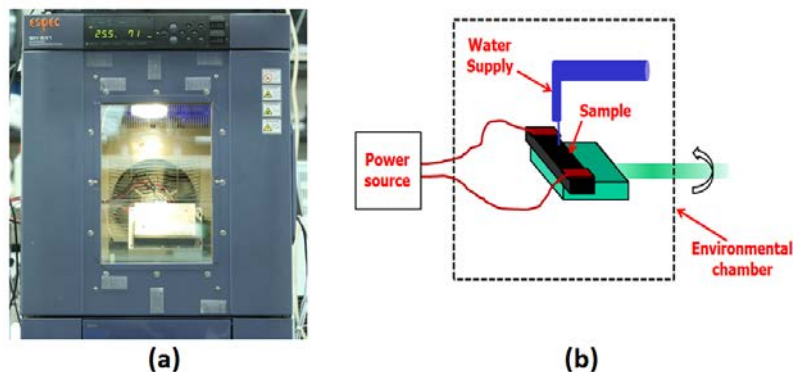


Figure 24: (a) Environmental Chamber; (b) Schematic of Experimental setup

The icephobic properties of these three surfaces were studied inside an environmental chamber (ESPEC Corp. Japan, Model SH-641, Bench top type temperature and humidity controller) as shown in Figure 24.a. A custom made rotary platform was used to keep the coated glass slide inside the chamber. The schematic of this set up is shown in Figure 24.b. As shown, the coated glass slides were connected to an external power source via alligator clips attached to the copper tape electrodes, placed at the two edges of the slide. The whole platform was mounted on a metallic rod, which was used to rotate the platform from outside of the chamber. A graduated scale attached with this rod, was used to measure the roll off angle during the experiment. Initially a sessile deionized water droplet of temperature 0°C was deposited on each of these surfaces, while their surface temperature was also at 0°C . Both the surface and the droplets were continuously cooled till the surface and atmospheric temperature reached -25°C . During this cooling process the water droplet on the surfaces froze within 5 minutes. When both the surface and atmosphere reached -25°C , the DC power source was turned on. For each surface, the time of total melting of sessile droplet was measured. Based upon the applied voltage and coating resistance, total power consumed (over the whole surface) until complete melting of the frozen droplet was calculated and tabulated in Table 2. It is quite evident that for the superhydrophobic self-cleaning surface, the amount of energy required for complete melting was highest.

Sample	Energy spent till complete melting of droplet (J)
S1	664
S2	615
S3	600

Table II: ENERGY SPENT TO COMPLETELY MELT THE FROZEN WATER DROPLET.

This observation can be explained by the very low rate of heat transfer from the surface to the frozen droplet, due to the lower surface-to-droplet contact area, a typical characteristic of

superhydrophobic self-cleaning surfaces. This explanation was further confirmed when the spent energy slightly decreased in the case of superhydrophobic surface with moderately high roll off angle of 35°-40° (S2), where the contact area between the surface and the droplet expected to be higher, thus resulting in higher heat transfer rate. The third (sticky) superhydrophobic coating follows the same trend and reveals the smallest amount of energy to melt the droplet completely, though not significantly different than the surface S2. One interesting observation made in these experiments was that the roll off angle of the molten water drop significantly increased from its room temperature value. The roll off angle of molten drop in surface S1 increased to 30° from below 10°. Similarly for surface S2 it increased to 50° from 35°. Most likely during the freezing process the water expanded into the rough asperities of these soft surfaces, thus offering sites for the melted water to attach, and in turn raising the value of the roll off angle.

In a separate set of experiments, surfaces with a frozen drop were kept at different tilt angle before the application of external voltage. Here both the surface and droplet (frozen) temperature were kept initially at -25°C. The time required for droplets to shed off from the surface was recorded for all the surfaces and for different tilt angles. Total spent power was also calculated based on these times along with respective power input to those coatings. Table 3 lists the details of all experimental measurements.

S 1		S 2		S 3	
Tilt angle (deg.)	Energy spent till droplet detachment (J)	Tilt angle (deg.)	Energy spent till droplet detachment (J)	Tilt angle (deg.)	Energy spent till droplet detachment (J)
90	153	90	193	90	NA
70	166	70	213	70	NA
50	196	50	235	50	NA
32	245	40	NA	30	NA
30	NA	10	NA	10	NA

Table III: ENERGY SPENT FOR SHEDDING FROZEN WATER DROPLET FROM THREE DIFFERENT SURFACES HELD AT DIFFERENT TILT ANGLE. NA INDICATES THAT NO DROPLET DETACHMENT OCCURRED AT THE CORRESPONDING CONDITIONS.

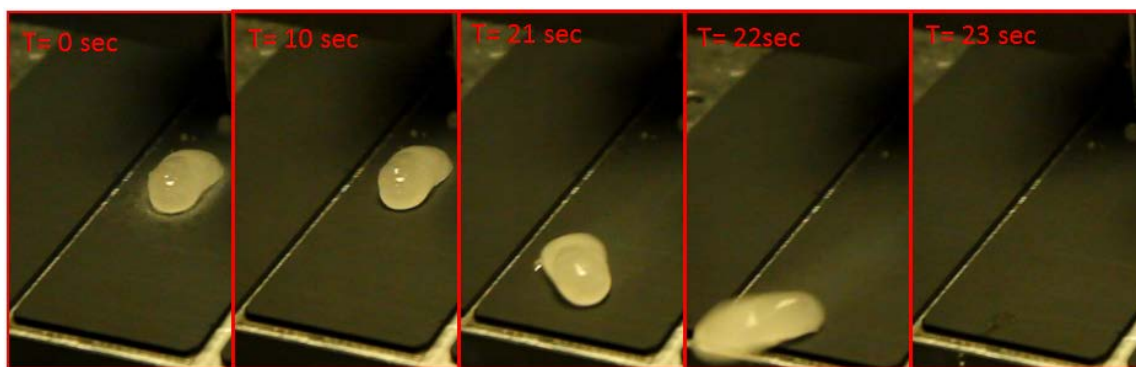


Figure 25: Sequence of ice from supercooled water shedding off from the surface even when most of the ice was not melted.

The energy consumption by the whole substrate, till the frozen droplet sheds off from surfaces S1 and S2, is significantly lower than the respective energies of complete droplet melting. During the freezing process, liquid water close to the interface expands in volume and becomes ice. This ice phase may anchor to different roughness sites of these surfaces; hence ice sticks to the surface. The smaller time for droplet detachment from the surface S1 and S2, clearly indicates that as soon as the ice close to the droplet surface interface melts and forms a thin liquid film, it sheds off from the surface due to the action of gravity force and small liquid-solid contact area. The droplets when sliding off from the surface comprised mostly of ice. Similar observation was also made while melting the ice formed via freezing of supercooled water of -10°C (see Figure 25 also for supercool water). Due to its higher surface tension, the small amount of water takes away the still frozen ice phase with it, while simultaneously shedding off from these surfaces. The energy consumption for droplet detachment from surface S1 is significantly lower even compared to the energy required for complete melting on surface S3 (which shows the best performance for sessile droplet melting in horizontal arrangement, in terms of energy consumption). With increase in tilt angle, this reduction is much more pronounced, as expected. At higher tilt angle, gravity force is higher; hence the greater is the force imbalance to make the droplet move away easily from the surface. The surface S1 shows almost 60% reduction in energy consumption when held at its roll off angle 32° (of molten drop) and 75% reduction at tilt

angle of 90° (compared to the lowest energy consumed in sessile droplet melting in horizontal configuration). For the surface S2, these values are 61% and 68% respectively.

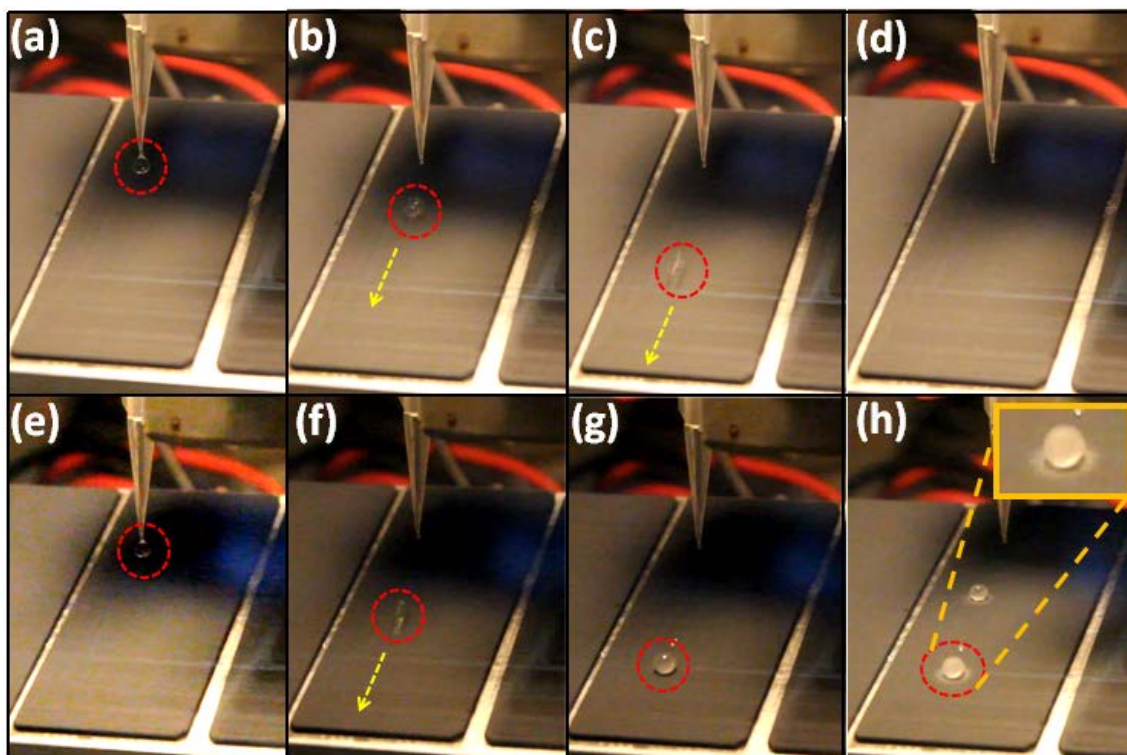


Figure 26. Sequence of supercooled (-11°C) water droplet interaction with self-cleaning surface held at (a)-(d) -5°C and (e)-(f) -16°C . Figures (a) – (d) were taken at 250 ms interval. Figures (e) – (g) were also taken at 250 ms apart. Figure (h) was taken 3 minutes after (g). The inset of image h shows the frost halos formed around the periphery of the frozen droplet on this surface.

In order to assess and compare the energy consumption of the self-cleaning surfaces with non self-cleaning superhydrophobic surfaces, another experiment was carried out. Here the calculated energy is consumed to maintain a minimum surface temperature (critical temperature) where supercool water droplet rolls off from the surface without freezing on the surface. A peltier cooler was used in this experiment to cool the surface (a detail of the setup is being already explained in Section 2.4.2.4). Initially, the critical temperature^[29] of these surfaces was experimentally determined. The lowest surface temperature at which 7 micro-liter supercooled water droplet of -

11°C rolls off from the surface tilted by 15° in -11°C ambient atmosphere was measured. This temperature was defined as the critical temperature of the surface at a given ambient temperature and tilt angle. The critical temperature of surface S1 was found to be -14°C. Hence this surface would be ice-free under freezing rain of -11°C supercool droplets, if the surface temperature was maintained above -14°C. Whereas for the other two surfaces this temperature should be above zero since, the water droplets stuck to them and eventually froze. Since the surface temperature is proportional to the input power or power density, for self-cleaning surfaces power consumption is significantly less. Based upon the temperature evaluation experiments, this translates into almost 45% reduction in power consumption under the given condition (-11°C ambient temperature and 40% RH, -11°C water temperature). For higher wind speeds, this difference in power consumption is expected to be even higher. Figure 26 shows sequences of two experiments carried out, over and below the critical temperature of the surface. In one case (top row), droplet rolled off from the surface without freezing on it. In another case (bottom row), where the surface temperature was below the critical temperature, the droplet froze after travelling few centimeters. Figure 26.h shows how frost halos ^[116] formed around the frozen supercooled water droplet periphery. When supercool water freezes it releases heat of fusion, which evaporates some amount of water from the droplet surface. This evaporated water eventually cooled down, condensed on the surface and froze around the frozen supercooled water droplet, thus creating these halos.

The surface S1 showed promising results in frosting and defrosting experiments as well (set up described in detail in Section 2.4.2.4). Here the surface was cooled down to -10°C by a peltier cooler, while the ambient temperature was maintained at 15°C with 90% relative humidity. Due to significant temperature difference, the moisture from the air condensed rapidly on surface S1. After sometime, these condensed drops froze on the surface. After half an hour, a significant amount of frost was accumulated on this surface (Figure 27.a). At that point, the surface was

heated either by the peltier itself or by an external power source connected to the two electrodes attached on the surfaces. In both of these cases, although the frost melted completely on these surfaces, some small amount of water remained (Figure 27.b); a gentle blow of air completely removed them from the surface (Figure 27.c). This shows that after the defrosting process, the surface retains its self-cleaning property. Subsequent contact angle and roll-off angle measurement at room temperature showed no variation from their respective original values.

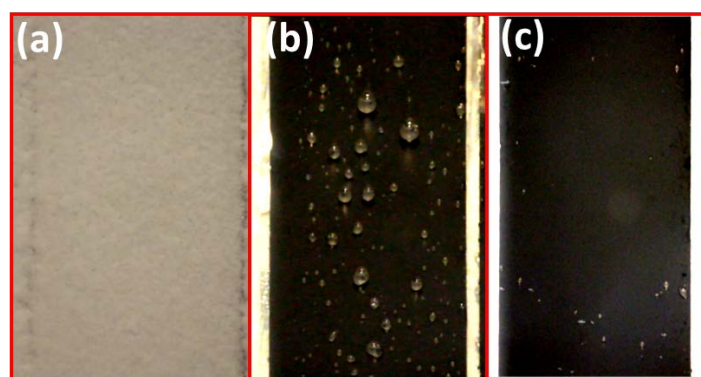


Figure 27: Image of PTFE/CNF coating (a) before, (b) after defrosting with peltier. Figure (c) shows the surface after been subjected to gentle air blow.

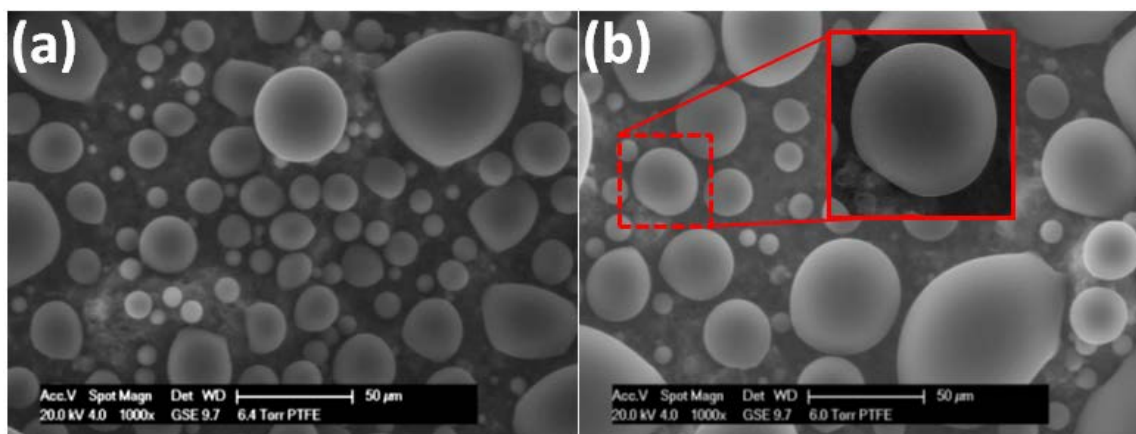


Figure 28: Condensation of water vapor in the form of micro droplets on the PTFE/CNF self-cleaning composite surface inside the environmental scanning electron microscope operated in wet mode. Figure (a) was taken at pressure 6.4 Torr during the condensation process. Figure (b) was taken at 6 Torr, during the process of gradual pressure reduction to facilitate evaporation of the droplets. For all these experiments, ambient temperature was lowered ($\sim 4^{\circ}\text{C}$) to achieve 100% relative humidity.

ESEM images under wet mode also confirmed the superior wettability properties of Surface S1. Initially water vapor was allowed to condense on the surface (Figure 28.a) at 6.4 Torr. Subsequently, evaporation (Figure 28.b) of the condensed water was induced by lowering the pressure to 6.0 Torr to check how these surfaces retain their wettability properties under condensation. In both of these two stages of the experiments, the shape of the condensed micro water droplets remained very spherical in shape, indicating high contact angle even at the micro scale (inset of Figure 28.b). During the evaporation step when droplet size got reduced gradually, no significant change in spherical shape was observed, pointing towards no water imbibition into the surface micro-nano asperities.

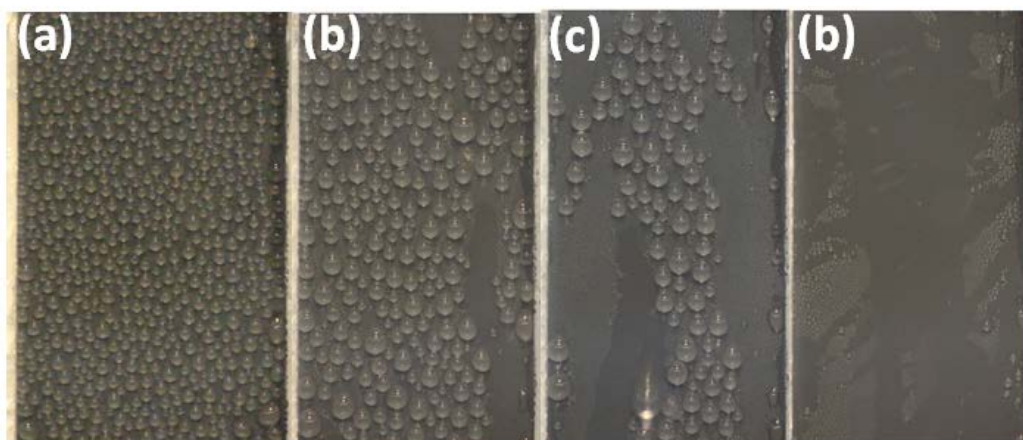


Figure 29: PTFE/CNF based self-cleaning under extremely humid environment of 90% RH and 15°C. (a) surface before condensate reaches critical size; (b) condensed droplet with diameter above critical radius glides down from the surface and exposes new area for condensate to form; (c) drop gliding down the surface and taking with it all droplets in its path; (d) surface after a gentle blow of air

To confirm this water repellency property at the macroscopic scale, these surfaces were kept inside the environment chamber under 90% relative humidity at 15°C. Surface temperature was kept at 2°C to allow the condensate to form on the surface (Figure 29.a). After reaching a critical size, condensed droplets slid off the surface, leaving behind a fresh area free of condensate (see

Figure 29.b) allowing fresh sites for condensation. Condensed drops, while gliding through the surface, also carried along all smaller sized condensed drops, including the micro-droplets providing further new sites for condensate to form. A gentle blow of air removed most of the micro condensed droplets from the surface, confirming its extreme wettability with micro condensate droplets formed in an extremely humid environment.

2.4.2. CNF-PMC electro-conductive composite coatings

2.4.2.1. Materials and surface synthesis

Electrically conducting superhydrophobic surface with self-cleaning property was synthesized by spray casting a dispersion of HHT CNFs and a fluorinated-group-containing acrylic co-polymer (PMC, Trade name Capstone ST-100, DuPont) in a mixed solvent system of acetic acid and acetone. HHT CNFs were initially probe sonicated at 40% amplitude for 1.5 minutes in the mixed solvent (acetic acid:acetone; 1:2 wt. ratio). CNF weight concentration of 0.81% was used to prepare the dispersion. Simultaneously 20 wt% PMC solution was mixed with acetic acid and acetone at 1:2:4 weight ratio and added to the probe-sonicated HHT CNF dispersion, in such a way that CNF:PMC weight ratio becomes 20:80, 30:70, 50:50 in three different dried composites. The water contact angles of these coatings were found out to be about 160° , while the roll off angles were less than 4° indicating their superior superhydrophobic and self-cleaning property.

2.4.2.2. Surface morphology

The morphology of these surfaces was characterized by a field-emission environmental scanning electron microscope (XL30 ESEM-FEG, Philips/FEI Co., Hillsboro, OR). The surface morphologies of these coatings are mostly similar and feature micro/nano hierarchical structure typical of spray coated superhydrophobic surfaces. The presence of CNFs makes the surface look like a fiber mat structure at the nanoscale, as evidenced from the SEM images (shown in Figure 30.a , b) of the 30:70 CNF:PMC surface. The highly re-entrant structures also enhance super-

hydrophobicity. At higher polymer content, the surfaces show significant presence of non-filamentous polymeric phase.

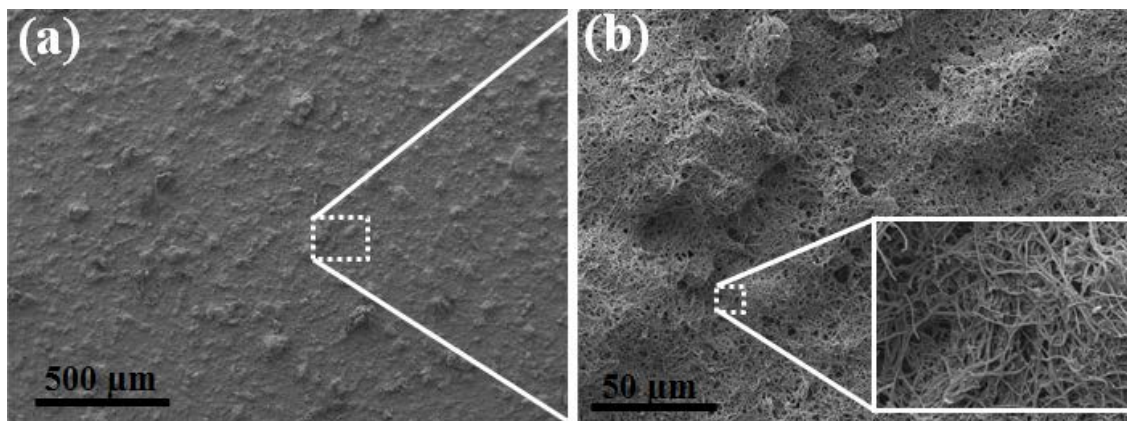


Figure 30: ESEM images of 30:70 CNF:PMC composite coating surfaces at (a) $100\times$ and (b) $1000\times$ magnification. Inset of image (b) shows the nano-filamentous structure generated by the HHT CNFs.

2.4.2.3. Electro-thermal properties

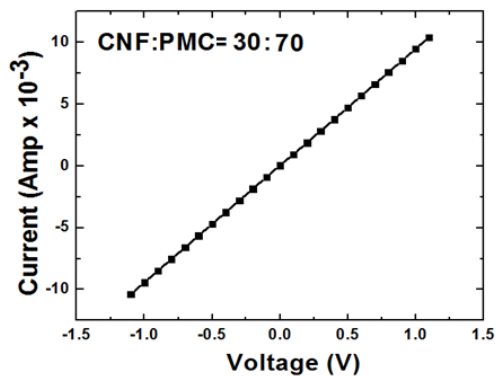


Figure 31: I-V curve of 30:70 CNF-PMC composite coating

Similar to the electro-thermal characterization carried out for the PTFE/CNF/PVDF/PMMA composites discussed in Section 2.4.1.3, I-V curves and temperature evolution tests were carried

out for the CNF-PMC coatings. Figure 31 shows the I-V curve, while Fig. 32(a) and (b) show the temperature evolution curves for 30:70 CNF:PMC at -30°C and -15°C ambient, respectively.

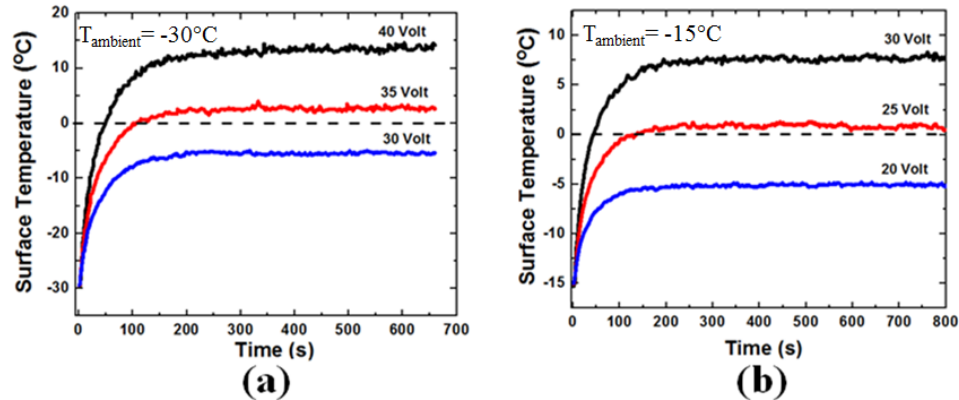


Figure 32: Surface temperature evolution of CNF-PMC 30:70 nanocomposite self-cleaning surface at (a) -30°C , (b) -15°C ambient temperature. Relative humidity of 40% and air velocity of 2 m/s were maintained inside the chamber.

A significant amount of fluctuation in the temperature profile is observed even at steady state, due to the chamber air blowing over the surface. For the measured air velocity of 2m/s, it is expected that turbulent boundary layers exist over these surfaces, thus resulting in the temperature fluctuations observed.

2.4.2.4. Icing experiment

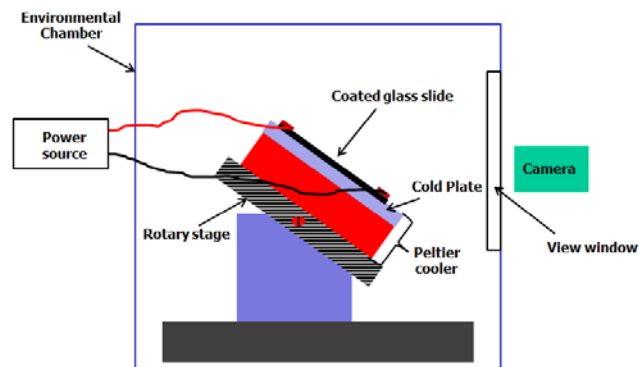


Figure 33: Schematic diagram of experimental set up used to evaluate the performance of CNF-PMC coatings in defrosting experiments.

PMC-CNF self-cleaning surfaces with different proportion of PMC and CNF were prepared. In order to evaluate their performance, microscope glass slides coated by these surfaces were fixed onto the cold plate of a thermoelectric peltier cooler (CP-061, TE Technology) with thermally conductive glue. The peltier cooler was mounted on a rotary stage and positioned at 30° with respect to the horizontal for better viewing. The schematic of the experimental setup is shown in Fig. 33. Initially, three surfaces with different ratio of CNF and PMC were studied. The ratios of CNF:PMC were 20:80, 30:70, 50:50, respectively. The surfaces were first covered with a very thin plastic film to prevent premature condensation on them, while cooling them to -5°C. The environmental chamber was maintained at 15°C and 60% relative humidity. When the surface temperature (measured by a K-type thermocouple) reached -5°C, the plastic film was removed to let frost form on the surface. Frost was allowed to accumulate on the surfaces for the subsequent 30 minutes. Afterwards, the peltier cooler was set in reverse mode (acted as a heater) to bring the coating temperature to 20°C. A digital SLR camera (Canon EOS T1i) was used to record the events until the surface reached room temperature. At the initial stage of frosting, it was observed that the surface with highest polymer content (20:80) showed delay in frost formation. The surface lost its superhydrophobic self-cleaning property, as the area below the water drops was observed to be very dark, indicating a Wenzel wetting state. On the other two surfaces (30:70, 50:50), the contact area below the water drops looked very shiny, indicating a Cassie wetting state. A gentle blowing of air removed these droplets from the surfaces. Based upon this experimental observation, the 30:70 composition was chosen for further study.

The next defrosting experiment was carried out with a glass control surface and two coated surfaces. The 30:70 CNF:PMC formulation was used in two coated samples, which had hierarchical roughness. The third surface was connected to an external power source via two copper electrodes. The second surface was left as is without any electrodes. The experimental procedure was same as before until frost formation. After frost was allowed to accumulate for

half an hour on these surfaces, an external DC voltage of 40 V was applied on the third surface, while keeping the peltier in cooling mode. Figure 34 shows a sequence of images during the defrosting experiment. The last image shows how efficiently the frost was removed from the surface, while two other surfaces were still covered with frost. Compared to peltier heating (which occurs undercoating), skin heating seems to be much more effective. Unlike the previous case, no trace of water was observed on the skin heated surface after the frost melted.

During the skin-heating-assisted defrosting process, it was observed that the mixture of frost and molten water withdraws itself by dewetting the surface. Another interesting observation in this experiment was the significant presence of ice/frost in the retracting frost layer. When frost melted, it formed a thin layer of liquid film, which tended to form a very high contact angle with the surface due to its inherent superhydrophobic self-cleaning property. By this process, the little amount of water took away the frost from the surface; this mechanism is due to the very high surface tension of water. The critical temperature of this surface at -20°C and 50% relative humidity and 15° tilt angle was measured to be -25°C , indicating a very significant reduction in energy consumption required to maintain an ice-free surface under supercooled water droplet/freezing rain condition. Though these surfaces performed very well, their long term durability may be an issue. Hence a detailed study is required to estimate their long term durability (in terms of retaining repellency) after many cycles of surface defrosting, thermal cycle, etc. Evaluation of their icephobic properties at high impact velocity of water drops also must be examined thoroughly.

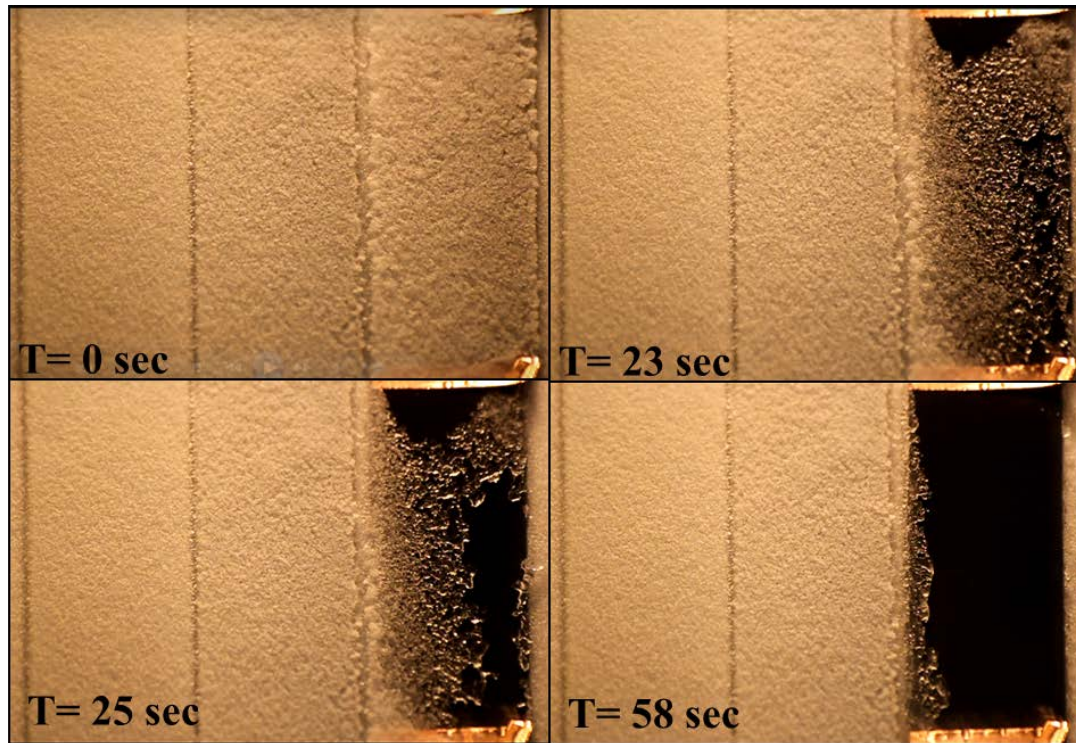


Figure 34: Sequence from a defrosting experiment (a) at the fully frosted state $t=0$, and (b) 23s, (c) 25s (d) 58s after the onset of skin heating for the rightmost surface. The three surfaces (from left to right) were glass, coated glass, and coated glass with active skin heating.

3. SUPERHYDROPHOBIC, ELECTRICALLY CONDUCTING, POLYMER COMPOSITES FOR GHz AND THz ELECTROMAGNETIC WAVE ATTENUATION AND THz DEVICES

3.1. Introduction

Electrostatic dissipation, microwave absorption and EMI shielding of sensitive electrical/electronic circuitry and devices, antenna systems, aerospace and military equipment (e.g. lightning-protection aircraft composite panels), stealth technology etc., are just few of many technologies where metal-based materials have been considered almost exclusively to this date. Flexible and lightweight, electrically conducting, polymer-based coatings have tremendous potential for such technologies, as recent studies indicate.^[35,62,117-120] Added functionalities, such as chemical inertness and water repellency, further contribute to the value of polymer-based coatings by preventing contamination and corrosion when exposed to outdoor conditions.

While electrical conductivity of super hydrophobic polymer based coatings/films has been measured in the sporadic works^[87,121-124] published in this area, and the potential of such materials has been mentioned^[87,124] in conjunction with EMI shielding, no study exists on EMI shielding properties of super-repellent, polymer-based films. Apart from the operational frequency domain (1GHz to 12GHz) of traditional instruments, it is also important to measure their SE in higher frequency range such as in THz domain owing to increasing research activity in this particular domain. Electromagnetic waves in the terahertz frequency range (0.1 – 10 THz) have remained the least explored and developed in the entire spectrum, thus creating what is widely known as the “THz gap.” In recent years, there has been an unprecedented growth in the development of terahertz devices, circuits and systems due to their promising applications in astronomy, chemical analysis, biological sensing, imaging and security screening.^[125-129] It is predicted that THz-based communication systems with data rates of 5-10 Gb/s or higher will

replace today's wireless LAN systems in 10 years.^[130] With the increasing speed of the THz electronic circuits and systems, electromagnetic interference shielding in the THz region is becoming more important.^[131,132] THz EMI shielding materials may also find applications in security and defense to protect information detectable by THz imaging and sensing techniques. In addition, effective THz attenuation devices are required in many quasi-optical systems (e.g. THz spectroscopy and imaging systems).

Among many THz quasi-optical components under development, THz polarizers are in high demand in spectroscopy, polarization interferometry, polarimetric detection (e.g., polarization of cosmic microwave background), and other areas.^[133] THz polarizers are highly anisotropic devices that present maximum transmission (T_{\perp}) with incident wave polarization perpendicular to the alignment axis, while having highest attenuation (T_{\parallel}) with polarization parallel to the alignment direction. Conventional THz polarizers have been realized by metal wire-grids,^[134] resulting in expensive, heavy, and bulky components, not suitable for many practical applications. To overcome this problem, micro-strip grids have been produced on substrates (e.g., silicon, polymer) for THz polarizers, using special techniques, such as nanoimprinting lithography and chemical etching.^[135-137] In addition, polarizers based on highly aligned single-walled carbon nanotube (SWNT) films (either on substrates or free-standing) have been demonstrated to have promising performance in the THz region.^[138,139] However, the available approaches either require complex (i.e., costly) or chemically aggressive fabrication steps, or are hindered by limitations in carbon nanotube film formation, growth, and transfer. Due to the above, existing approaches limit the choice of substrates and are frequently detrimental to the environment by generating hazardous waste. Therefore, innovations in materials and processes for cost-effective, environmentally friendly, scalable and potentially high performance THz quasi-optical components, such as polarizers, are of immense interest for a number of advanced technology applications.

The coating fabrication process^[140] used to prepare the THz polarizers, discussed in section 3.2 of this chapter is inherently low-cost, and all ingredients are commercially available. If these materials could be patterned using a ubiquitous low-cost method (e.g., inkjet-printing), one could bypass the complex photolithography, nanoimprinting, or chemical etching processes, and the cost-effective manufacture of flexible THz quasi-optical components, such as polarizers and filters, might be realizable. The idea of inkjet printing conductive inks to fabricate low cost electrical components has been explored recently^[141,142] in the fabrication of radio frequency antennas. The inks employed in those works were based on metal nanoparticles that require an additional thermal step (100°C –120°C) to produce the final product. In general, metal nanoparticle inks can produce highly conductive traces,^[142] but due to their higher concentrations of solids (which are necessary for depositing continuous, electrically conducting traces), metal nanoparticle inks are more vulnerable to deposit non-uniformities caused by the coffee-stain effect.^[143] Carbon fiber-based inks require considerably lower concentrations of solids for depositing conducting traces, as the large aspect ratio of fibers allows percolation at a lower threshold compared to the metal nanoparticle inks.^[140] In addition, non-spherical particles are far less susceptible to the coffee stain effect.^[144] The attractiveness of carbon fiber-based inks has been extolled in Ref. 142 and the references cited therein.

Preliminary work on superhydrophobic CNF/PTFE polymer composite coatings showed their potential as effective attenuators of both in GHz and THz radiation, indicated by their EMI SE (see introduction chapter) in these frequency ranges. SE and conductivity of these composites can be increased if the superhydrophobic aspect of these coatings is set aside. Moreover based upon high attenuation of the composites, new THz devices can be prepared. All these new possibilities provide the motivation for the work presented in the first section of this chapter. The second section of the chapter is about the design and fabrication of quasi-optical THz polarizers. The dispersions of a fluoroacrylic co-polymer with carbon nanowhiskers (CNW) are dispensed using

standard inkjet printing procedures to fabricate these polarizers. First, the EMI shielding effectiveness of continuous (large-area) CNW composite coatings is characterized in the 570GHz–630GHz frequency range. The inkjet printing process of the polarizers is then presented, followed by measurement results for a prototype THz polarizer. An average degree of polarization of 0.35 is achieved for a CNW coating thickness of 1 μm .

3.2. PTFE-CNF based, electrically conducting, superhydrophobic composites as THz and GHz film attenuators

3.2.1. Experimental

A solution blend of poly-vinylidene fluoride (PVDF) and poly-methyl methacrylate) (PMMA) forms the composite polymer matrix, which has a good degree of hydrophobicity and interfacial adhesion properties. PVDF with its environmental durability, hydrophobicity combined with its chemical inertness, is an ideal choice for the hydrophobic component in the binder polymer, while adhesion and particle dispersion is imparted by the acrylic PMMA. Sub-micron PTFE particles are used as hydrophobic fillers to tune the coating microstructure and reduce surface energy,^[27] whereas the electrical conductivity is manipulated by heat-treated, vapor-grown carbon nanofibers (CNFs).^[34,145]

3.2.2. Solutions/dispersions and spray application

To prepare the composite coatings, 60/40 wt.% solution blends of PVDF (530 kDa; Sigma–Aldrich, USA) in Dimethylformamide (DMF) and PMMA (996 kDa; Sigma–Aldrich, USA) in acetone were mixed first. CNFs (average fiber dia. 100 nm, PR24 XT-HHT Pyrograf III; Applied Sciences Inc., USA) and sub-micron PTFE particles (average dia. 260 ± 54.2 nm; Sigma–Aldrich, USA) in dispersions were added as fillers to create sprayable solutions which, after application on glass and cellulosic substrates, were heat-dried at 90°C for 1.5 hrs to remove any residual solvent. The CNFs are free of CVD carbon with highly graphitized structure developed by high

temperature treatment, resulting in higher electrical and thermal conductivity compared to as-grown fibers^[146]. The composite films were super-hydrophobic and had electrical conductivities spanning over six orders of magnitude for the following weight composition range: Polymer matrix/PTFE/CNF 1/5.76/0.068-1.1.

3.2.3. Conductivity, contact angle and roll-off angle measurement

The dried coating thickness was measured using an optical microscope calibrated for depth measurement (top vs. bottom of the coating). Typical coating thickness was near 100 μm . The electrical conductivity of the coatings applied on glass slides was measured with a Keithley 6517 electrometer/ ammeter by the two-probe method. The coating areas selected for contact with the measuring probes were coated with a conductive silver paint to ensure good electrical contact. A Lab-view based program was used to generate I–V curves and extract the electrical resistance of the coatings, which was then used to determine conductivity using the measured values of the coating thickness, width and length. Electrical conductivity of the coatings rose with CNF loading. Water droplet contact and roll-off angle measurements were performed using an in house goniometer type optical setup described previously.^[27]

3.2.4. Scanning electron microscope observation

Figure 35 shows SEM micrographs of the surface morphology of the composite coatings for the two extreme CNF loadings studied (a–b 0.068, c–d 1.1). Surface morphology was altered from predominantly PTFE clustered spheres with some CNF strands to a mix of PTFE spheres and nanofibers (compare Fig. 35b and d) with 15 fold increase in CNF loading. With increasing loading of CNFs, electrical conductivity of these coatings improved dramatically because of the formation of highly percolating network created by the high aspect ratio CNFs (as observed in Fig 35.d). Higher curvature and re-entrant morphology imparted by the CNFs also facilitate improved wettability properties.

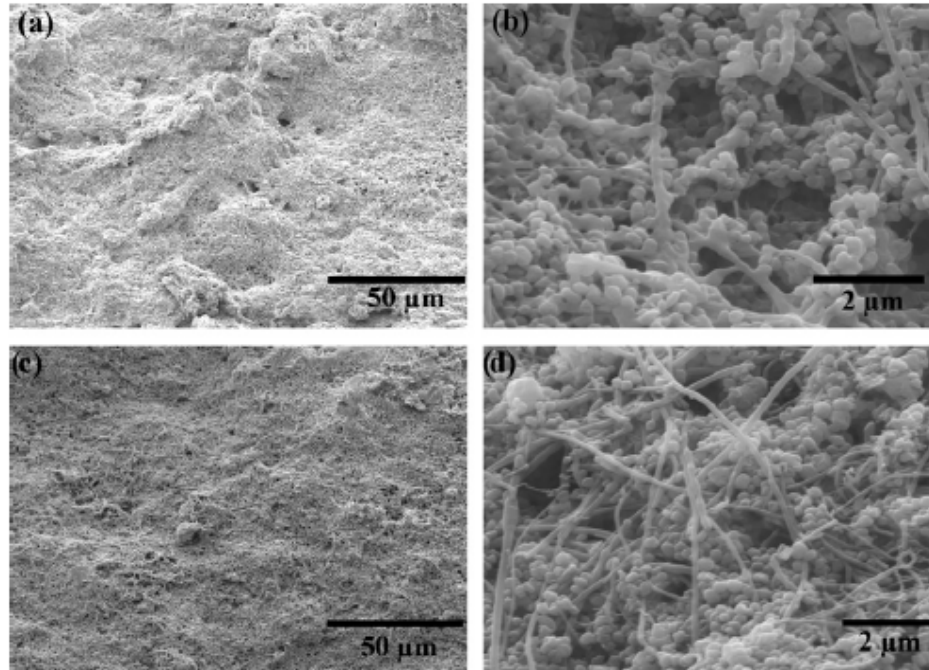


Figure 35: SEM images of composites with CNF loading of (a), (b) 0.068 ; (c), (d) 1.1 at different magnifications.

3.2.5. Definition and measurement of S parameter

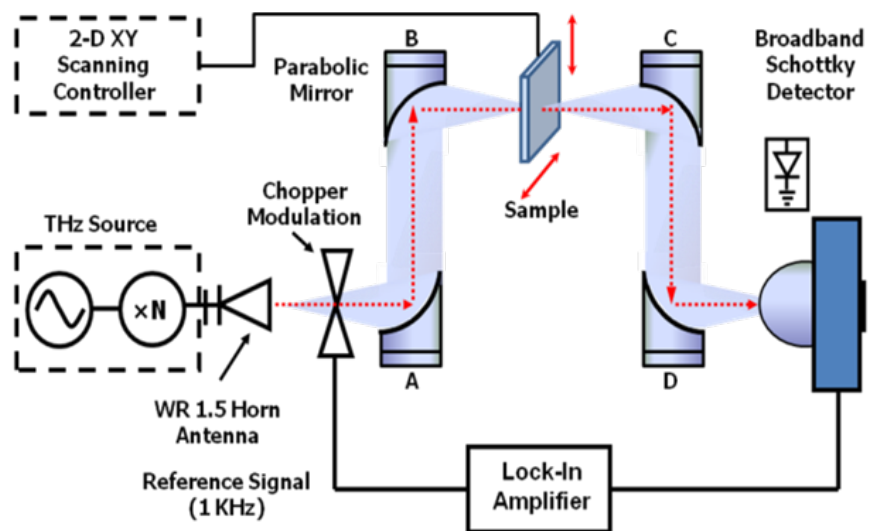


Figure 36: Frequency domain terahertz spectroscopy system ^[140] (available at Notre Dame University).

The details about the S parameters and shielding effectiveness have been discussed in the introduction chapter of this thesis. EMI shielding measurements in the X-band (8.2 GHz to 12.4 GHz) were carried out by a two-port vector network analyzer (HP 8719D, described in the introduction chapter) and calibration tool (HP X11644A WR-90). Shielding experiments in THz domain were carried out by the frequency domain terahertz spectroscopy system depicted in figure 36.

3.2.6. Results

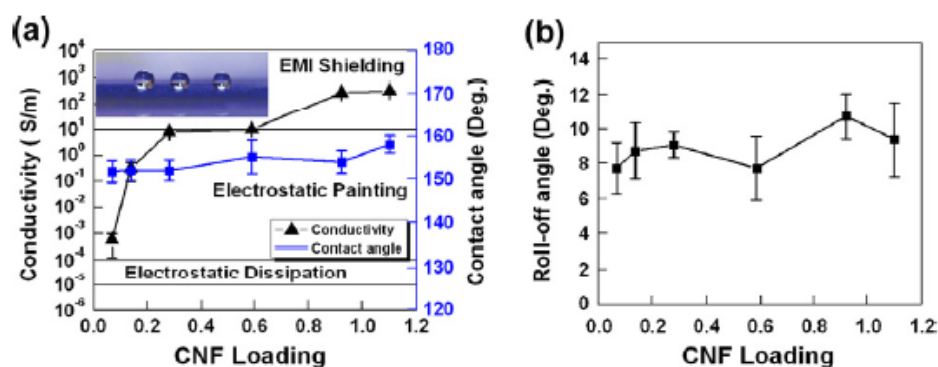


Figure 37: (a) Electrical conductivity and sessile water contact angle for various (PVDF+PMMA)/PTFE/CNF composite coatings as a function of CNF loading expressed in terms of CNF/(PVDF+PMMA) weight ratio. In all cases, the PTFE/polymer weight ratio was 5.76. The conductivity regimes suitable for different applications are marked by the horizontal lines. (b) Water droplet roll-off angle on coatings with different CNF loadings.

Figure 37 shows the results of wettability tests and conductivity measurements for composite coatings with different CNF loadings expressed in terms of CNF/polymer weight ratio. As shown in Fig. 37.a, static water contact angles for all CNF loadings remained above 150° . At the maximum CNF loading of 1.1, contact angle reached a value of 158° . As Fig. 37.b indicates, water droplet roll-off angles for all CNF loadings remained close or below 10° , confirming the self-cleaning water repellent nature of these coatings. As expected, Fig. 37.a shows an increase in conductivity of the composite coatings with rising content of conductive CNFs. It can be seen

that the electrical percolation threshold for the coatings falls within the 0.068–0.138 CNF loading range, which corresponds to CNF content of 1–2 wt.%. It is clear from Fig. 37 that CNF loading can be used as a tuning parameter to vary conductivity of the coatings by more than five orders of magnitude without compromising superhydrophobicity. A maximum conductivity value of 309 S/m was obtained for coatings with CNF loadings around 1.1.

3.2.6.1. Shielding results in the X-Band

S-parameter S_{11} quantifies reflection from the coatings, while S_{21} quantifies transmission through them. Through these measurements, it was observed that these two parameters under 2-port network test is reciprocal, i.e., $S_{11} = S_{22}$ and $S_{12} = S_{21}$, which means that the EMI shielding effect of the present composite coatings is similar at their front or back side. The S parameter values can be used to calculate the transmitted and reflected power as a percentage of input wave power in the two port configuration. The average reflected and transmitted power output (percent of input power) for different coatings with varying CNF loading are thus plotted in Fig. 37, which indicates that as CNF loading rises, the reflected power output rises, hence the absolute value of S_{11} decreases.

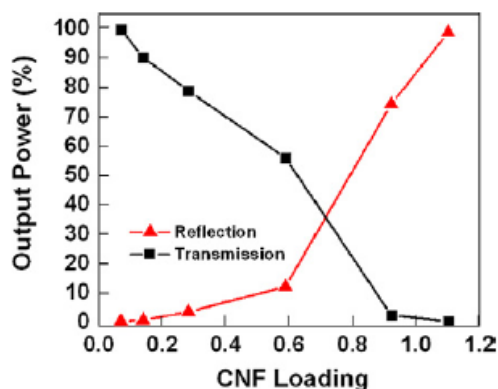


Figure 38: Variation of transmitted and reflected power with amount of CNF loading expressed in % of incident power.

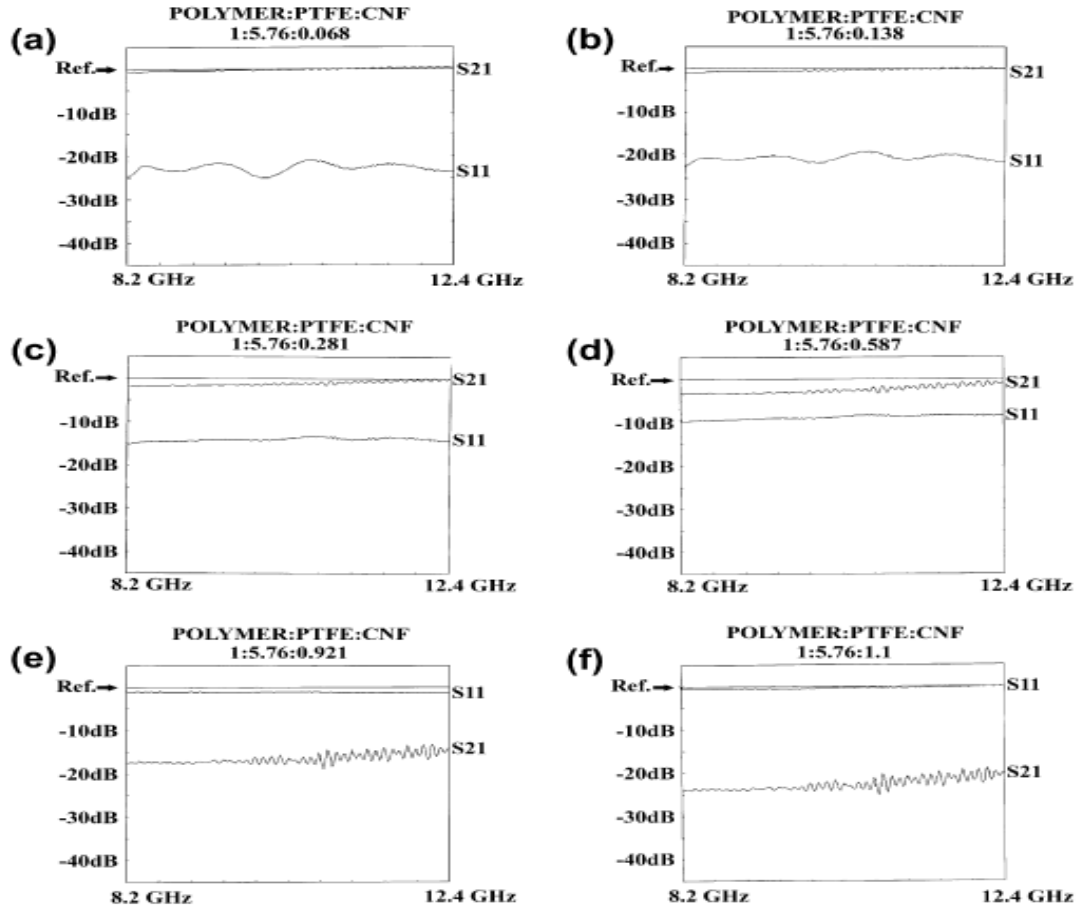


Figure 39: S parameters, S_{11} (reflection) and S_{21} (transmission), for coatings with different CNF loading in the 8.2-12.4 GHz frequency range (X-band), as obtained by means of the two-port measurement setup shown in Fig. 12.

This is evident from the values of S_{11} in Fig. 39.a–39.f. When the reflected power increases, it automatically lowers transmission, as absorption by these thin coatings is expected to be negligible. This is confirmed by the increasing absolute value of transmission parameter S_{21} at higher CNF loadings in Fig. 39. S_{21} (in dB) is the negative of shielding effectiveness of the coatings and increases in absolute value with increasing CNF loading, (see Fig. 39). The maximum attenuation was ≈ 25 dB in frequency range of 8.2–12.4 GHz (used by many radar systems) for coatings with CNF loading of 1.1 (highest). The percentage transmitted power drops from nearly 100% to 0.5% as CNF loading is increased from 0.068 to 1.1. An important outcome

of the measurements drawn in Fig. 39 is that both transmission and reflection parameters S_{11} and S_{21} remain fairly flat in the frequency range 8.2–12.4 GHz. This indicates that the present coatings are equally effective in shielding over this entire frequency range.

3.2.6.2. Shielding results in THz frequencies

The SE of these coatings in the 570-630 GHz range was measured by frequency domain terahertz spectroscopy (at Notre Dame University). The 570-630 GHz frequency domain THz spectroscopy system^[147] is shown in Fig. 36. Details of the measurement techniques have been discussed elsewhere.^[140] For 2-D mapping of SE, the source was fixed at one frequency, and the sample was scanned by the 2-D stage.

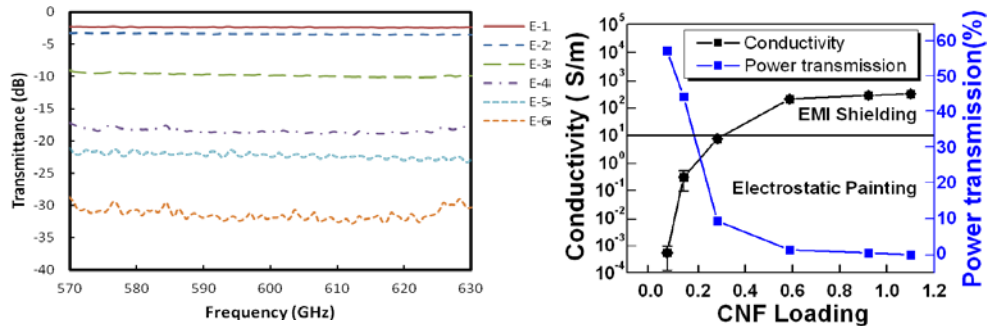


Figure 40: (a) Transmission vs. frequency plot for samples with different CNF loadings; (b) Variation of conductivity and percentage transmitted power with CNF loading.

Figure 40.a shows the THz power transmission measurement results, for six samples with CNF content same as studied in GHz studies with increasing order of CNF loading denoted by E1 to E6. For samples E-1 to E-6, a gradually increasing SE of 2.4 dB to 32.0 dB is consistent with the rising filler concentrations for those samples. The transmittance curves for samples E-1 to E-5 are quite uniform in Fig. 40.a, over the entire range of 570 GHz to 630 GHz. The ripples observed for sample E-6 are attributed to measurement noise.

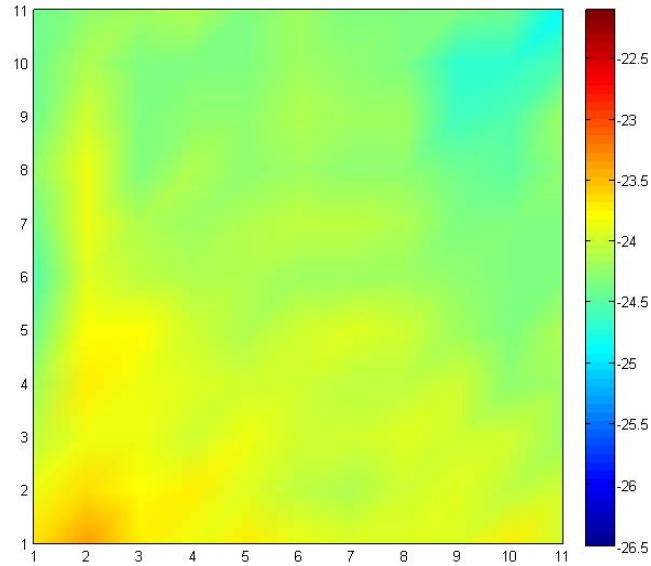


Figure 41: 2-D transmission map of sample E-5

To study the spatial coating uniformity in terms of attenuation, 2D scanning measurements for samples at 600 GHz were performed. The dimension of the scanning area was 10 mm×10 mm, and the scanning step size was 0.5 mm. As shown in Fig. 41, the transmittance of the scanned region of E-5 varies from -24.63 dB to -23.63 dB with uniformity of ~5.2%. Satisfactory practical applications of such coatings are possible with this amount of transmittance variation.

3.3. PMC based conductive patterns as THz polarizer

An electromagnetic (EM) wave polarizer usually consists of well-aligned grids with a period much less than one wavelength, and ideally, the finer the grid, the better the polarizer performance. However, in practice, a polarizer's performance (i.e., extinction ratio, T_{\perp}/T_{\parallel}) is limited by the finite conductivity of the metal wires or microstrips forming the grids. For THz polarizers patterned from thin film materials, the shielding effectiveness of the corresponding thin film, which increases monotonically with conductivity,^[134] sets an absolute upper limit for the polarization efficiency that can be achieved. Consequently, the SE of uniform CNW composite coatings had to be examined first.

3.3.1. Material and nanocomposite synthesis

PMC was used as received in the form of a 20 wt.% dispersion in water. The CNWs (solid core, 110 nm–170nm dia., 5–9 μm length) were procured from Sigma-Aldrich, USA. Reagent grade formic acid, acetic acid, and acetone were obtained from Sigma-Aldrich and used as received. For the continuous coatings, the CNWs were first dispersed in acetone and formic acid (2:3 mass ratio) and probe sonicated (Sonics ® vibra cell , 750 W, High Intensity Ultrasonic Processor, 13mm diameter tip at 70% amplitude) for 3min. CNW concentration in the acetone/formic acid medium was fixed at 1 wt. %. Finally, 20 wt. % PMC dispersion in water was gradually added to the suspension until the CNW/PMC mass ratio reached unity, from which point the suspension was bath sonicated for an additional 10 min. The final dispersions were applied onto cellulosic paper substrates by means of an airbrush atomizer (Paasche, VL siphon feed, 0.55mm spray nozzle). Spray cast films were dried at 90°C under a convective air space heater for 5min. Although the dispersion and thus the coating composition were fixed, coating thickness was varied by applying additional spray layers.

3.3.2. Results and discussion

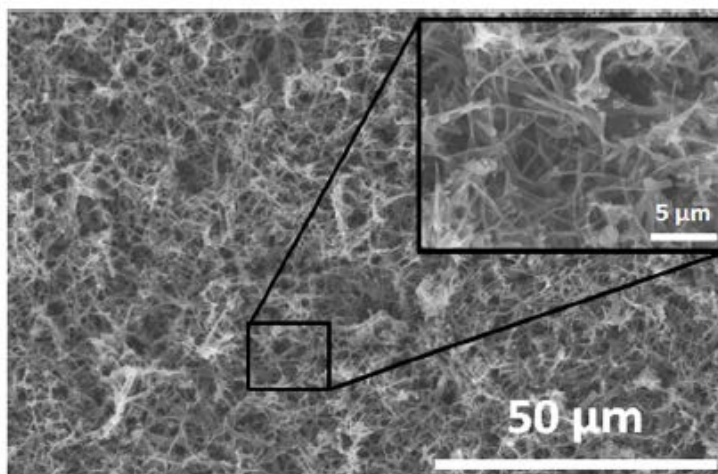


Figure 42: Scanning electron micrograph of a CNW/PMC (1:1 mass ratio) coating.

The SE of four coatings was measured (respective average thicknesses 24 μm , 42 μm , 61 μm , and 70 μm) and compared with the base SE of the uncoated paper substrate. The electrical conductivities of the coatings were measured by the two-probe method and found to be 118 S/m, 147 S/m, 209 S/m, and 386 S/m, respectively. The rising conductivity with coating thickness is attributed to the increased compactness of the thicker coatings, which were created by repeated spray-on layers. The prolonged drying time thus caused the dried solid phase to be less porous. Hence, thicker coatings had reduced thickness per unit deposited solid mass and displayed disproportionately higher electrical conductivity. Figure 42 shows a scanning electron micrograph of the surface structure of a CNW/PMC (1:1 mass ratio) coating. The presence of the percolated CNWs in the PMC matrix is apparent. The shielding effectiveness of the coatings in the 570–630GHz frequency range was measured by collaborators by the frequency domain terahertz spectroscopy instrument shown in Fig. 36. The THz radiation was provided by a VDI (Virginia Diodes, Inc.) frequency extension module (FEM, or multiplier chain) which converted a microwave (10–20GHz) signal from a synthesizer to THz radiation, covering the range from 570 to 630GHz. The average output power in this range was approximately 1 mW. The THz energy was coupled to a zero-bias Schottky diode broadband detector^[148] through four off-axis parabolic mirrors A-D (see Fig. 36).

Figure 43 shows the THz power transmission measurement results using the frequency domain THz system described above (Fig. 36) for five CNW/PMC coating samples with thickness varying from 0 μm (control, no CNW coating) to 70 μm . The control curve (uncoated paper) is indistinguishable from that of another sample (not shown in Fig. 43) coated with PMC only, thus confirming that transmission losses through the CNW/PMC composite coatings are attributed entirely to the CNWs. The THz transmittance (in dB) or EMI SE is defined by $\text{SE (dB)} = 10 \log_{10} (P_{\text{tran}}/ P_{\text{inc}})$, where P_{tran} and P_{inc} denote transmitted and incident THz powers. In these measurements, the Schottky detector worked in the square-law region, therefore the output

voltage response was proportional to the power detected. For the five samples, a gradually increasing average SE of 1.0 dB (control, no CNW coating) to 40 dB (for the thickest coating) is shown in Fig. 43 in the frequency range of 570–630 GHz, which is consistent with the increasing coating thickness of these samples. The transmittance curves for the first four samples are quite uniform over the entire frequency range in Fig. 43. The fluctuations observed for the 70 μm -thick coating (bottom curve) are attributed to measurement noise when the transmitted THz power is significantly low. We also measured the SE of a double-sided sample with a 70 μm -thick coating on each side. The THz SE of this sample far exceeded the system's dynamic range, thus suggesting attenuations much higher than 40 dB, and in turn, promising extraordinary performance of THz polarizers printed with this formulation and at double thickness.

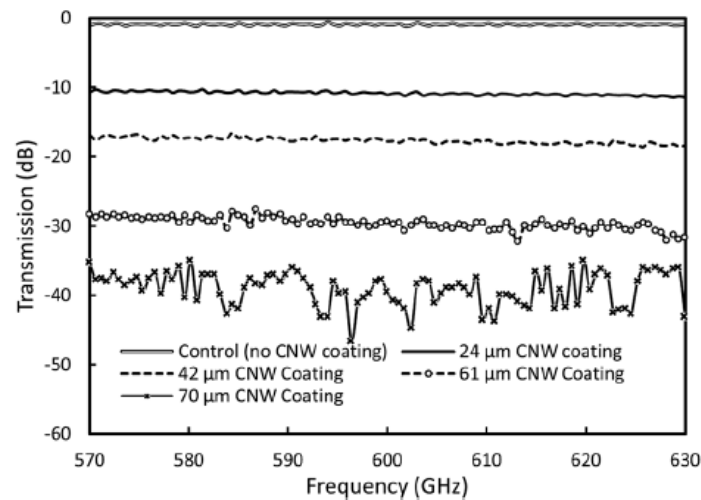


Figure 43: THz power transmission measurement results for composite coating samples with CNW/PMC mass ratio of 1:1 and average thicknesses as stated on the legend.

As shown in Fig. 44(a), the prototype polarizer was designed on $t=25\ \mu\text{m}$ thick Mylar film for operation at 600 GHz. Mylar thin films were chosen as polarizer substrates because of their low insertion loss (i.e., 0.35 dB for 25 μm thickness according to our measurement) at THz frequencies. Both the width (a) and spacing (d) of the composite strips are 100 μm , which is

roughly $1/5$ of the wavelength (λ_0 free space wavelength, assuming thin substrate) at 600 GHz. The printed dispersion was made by adding CNWs in acetone and bath sonicating for 10 min. Next, acetic acid was introduced into the suspension and the bath sonication was continued for another 10min. Finally, 20 wt. % PMC in water was added to the suspension until the CNW/PMC mass ratio reached unity (as in the continuous coatings characterized earlier); sonication was maintained for an additional 10 min. The final dispersion was diluted with water to a level such that the collective concentration of CNWs and PMC in the solution was less than or equal to 1.5 wt.%. Ink jetting was performed by a MicroFab JetLabVR 4XL system equipped with a $60\ \mu\text{m}$ diameter nozzle. The printing was performed in the drop-on -demand mode at a dispensing frequency of 500 Hz. The device consistently generated monodisperse droplets with diameters in the range $70\text{--}75\ \mu\text{m}$. The spot pitch was maintained constant at $40\ \mu\text{m}$, translating into a printing line speed of 20mm/s . The distance of the device orifice from the substrate was $0.5\ \text{mm}$. During the inkjet printing process, the designed pattern was printed one time to produce a coating thickness (h) close to $1\ \mu\text{m}$. This thickness estimate was made based on the content of each droplet, the droplet pitch, the line width, and the densities of each constituent (PMC $1.5\ \text{g/cm}^3$, CNW 2.3g/cm^3 , acetone $0.79\ \text{g/cm}^3$, acetic acid $1.05\ \text{g/cm}^3$). Thicker coatings for better performance can be achieved by repeating the same process more times. Figure 44.d shows an optical microscope image of a typical inkjet-printed THz polarizer on Mylar film. Although not perfectly produced, well-aligned CNW composite coating strips with designed width ($100\ \mu\text{m}$) and interspacing ($100\ \mu\text{m}$) were observed, demonstrating the capability of printing THz quasi-optical components without complex fabrication procedures. In addition, an inkjet printing resolution of less than $50\ \mu\text{m}$ is possible with current inkjet printing techniques. Linearly patterned CNW samples as shown in Fig. 43.a, are expected to show anisotropic EM wave polarization properties in analogy to SWNTs.^[149] As shown in Fig. 44.c, when the E-field of the incident THz wave is orthogonal to the CNF strip lines ($\phi = 90^\circ$), the induced magnetic currents (due to H-field) are not affected and re-radiate to the other side of the polarizer, causing minimum

insertion loss. However, when the polarizer is rotated parallel (or $\phi=0^\circ$) to the E-field (see Fig. 44.b), the polarizer allows minimum transmission.

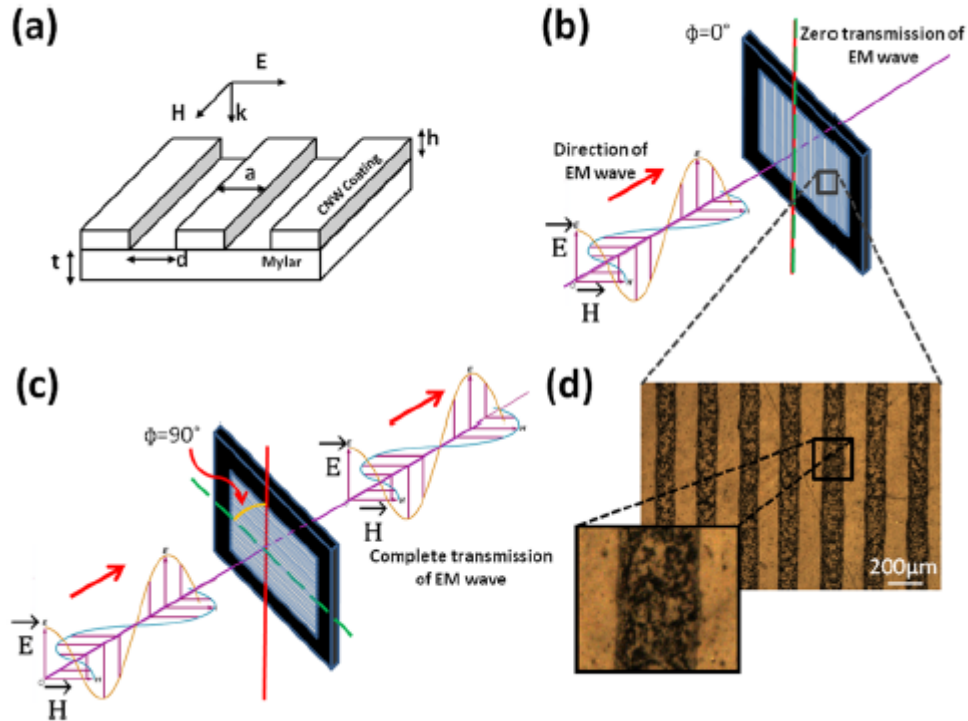


Figure 44: (a) Design of the THz polarizer fabricated on 25 μm -thick Mylar film, with 100 μm -wide microstrips separated by 100 μm spacing. The prototype polarizer had 1 μm CNW/PMC film thickness (h) and was characterized in the frequency band of 0.57–0.63 THz with the frequency domain THz spectrometer of Fig. 36. (b) Parallel orientation (0°) for minimum transmission, and (c) perpendicular (90°) orientation for minimum attenuation. (d) Optical microscope image of the inkjet-printed prototype THz polarizer. The dark lines consist of the CNW/PMC film material. The magnified detail shows the spatial non-uniformity of a typical strip. The dark areas depict high content of CNWs, while the bright areas indicate lower particle presence.

The inkjet-printed polarizer prototype was measured in the range of 570–630 GHz using the frequency domain THz system described previously. As shown in Fig. 45.a, the polarizer placed at perpendicular orientation (90°) showed maximum transmission averaging $T_{\perp}=0.93$, while the parallel orientation (0°) gave the lowest average transmission $T_{\parallel}=0.86$. A 45° oriented polarizer recorded a transmission level in between of T_{\perp} and T_{\parallel} , as expected. The observed fluctuations in

these plots are attributed to system noise and minor artifacts not fully removed in our tests. Nonetheless, the fluctuations in Fig. 45(a) are small enough (within $\pm 1\%$), showing fairly high measurement accuracy. To ensure that the observed anisotropic phenomena were indeed introduced by the aligned CNW microstrips, the corresponding absorbances, defined as $A = -\log_{10}(T)$, were calculated as in Ref. 138. Figure 45(b) displays the calculated absorbance for 0° (parallel), 45° , and 90° (perpendicular) orientations. The isotropic absorbance, which corresponds to randomly oriented CNW microstrips, was calculated as $(A_{//} + 2A_{\perp})/3$ and is plotted in Fig. 45(b) using the grey line. It is observed that the isotropic curve agrees very well with the values at 45° , indicating that the prototype polarizer works as intended. For all the data in Fig. 45(b), the 25 μm Mylar film substrate contributed only 0.35 dB to the absorbances.

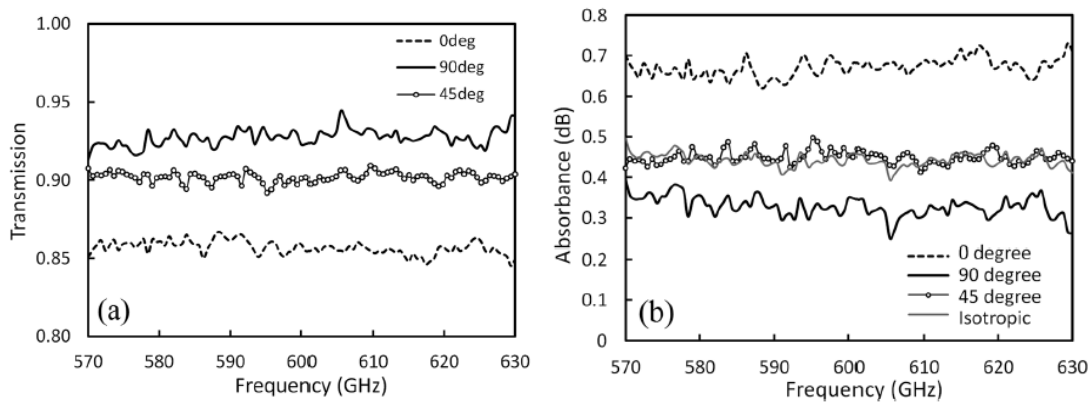


Figure 45: (a) THz transmission (T) spectra of the prototype CNW polarizer for three different polarization orientations: 0° , 45° , and 90° . (b) Corresponding absorbances, defined as $A = -\log_{10}(T)$, for the above three orientations and following Ref. 138.

Finally, the degree of polarization (P) of the THz polarizer was calculated using $P = (A_{//} - A_{\perp}) / (A_{//} + A_{\perp})$, and is plotted in Fig. 46. An average value of $P=0.35$ was measured over the entire frequency range of 570–630 GHz. The insertion loss (defined as $10\log(T_{\perp})$) of the polarizer with incident wave polarization perpendicular to the alignment axis (ideally maximum transmission) decreases with decreasing values of a and d (see Fig. 44.a), while the fractional

power transmission with incident wave polarization parallel to the composite strip direction (ideally minimum transmission) increases with $(a+d)/\lambda_0$.^[150]

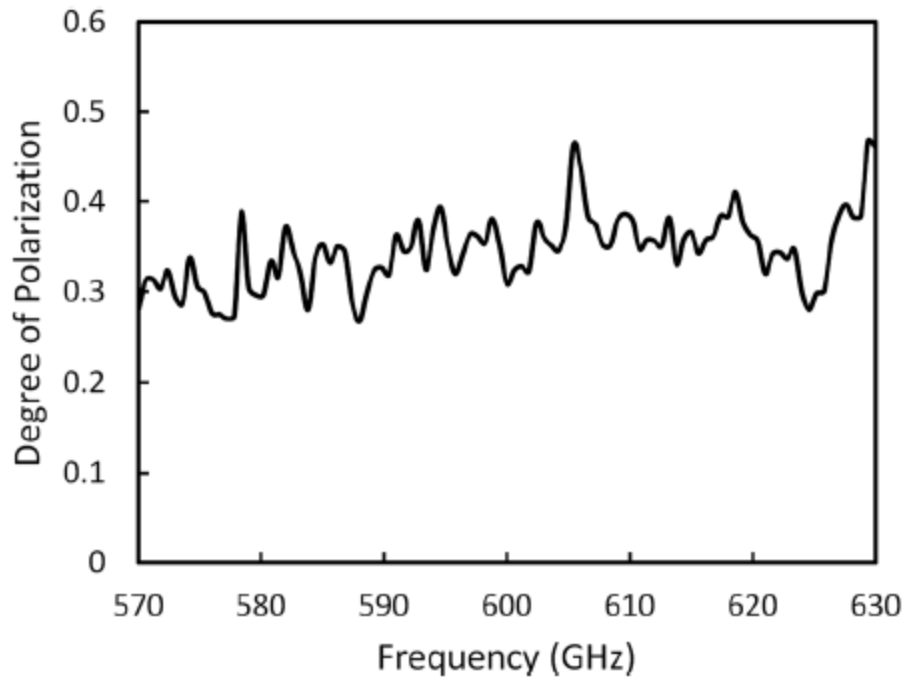


Figure 46: The degree of polarization (P) of the prototype THz polarizer over the frequency range of 570–630 GHz. An average degree of polarization of ~ 0.35 is seen for this polarizer with coating thickness of only $1 \mu\text{m}$.

Thus, the performance of the polarizer shown in Fig. 44(a) including extinction ratio (T_{\perp}/T_{\parallel}) and degree of polarization (P) could be greatly enhanced by using finer grids with smaller dimensions a and d . Compared to an ideal polarizer having a unit degree of polarization, this sample shows relatively low P and extinction ratio. However, the prototype has been proven to work as a polarizer, and its performance can be improved by increasing the composite coating thickness and decreasing both the composite strip width (a) and spacing (d). For example, Fig. 43 shows that an extinction ratio well over 30 dB can be realized with a coating thickness of $70 \mu\text{m}$. In addition, a dual-layer polarizer structure could be adopted to further improve the polarizer

performance, and as a result, a 60-dB extinction ratio is attainable near 600 GHz for a polarizer with dual-layer (70 μm each) coatings, as evidenced by the CNW composite coating THz EMI properties demonstrated in Fig. 43. Such levels of extinction far exceed the recently achieved^[139] values of 37 dB in the range 0.1–2 THz by winding nanotube sheets on U-shaped polymer frames and stacking them in 75 layers. In conclusion, we have developed an approach for cost effective manufacturing of THz quasi-optical polarizers based on inkjet printing of CNW/polymer composite coatings. The EMI properties of large-area CNW/PMC coatings have been studied in the frequency range 570–630 GHz using a frequency domain terahertz spectrometer. Shielding effectiveness of 40 dB has been achieved in the above bands with 70 μm -thick coatings, defining the feasible polarizer extinction ratio level. A prototype polarizer was designed and inkjet-printed on Mylar thin film with CNW composite coatings for operation near 600GHz. The measured transmission and absorbance vary with polarization orientation. The degree of polarization of this sample was 0.3–0.4 over the entire frequency range of 570–630 GHz, for a polarizer coating thickness of only 1 μm . The polarizer performance can be improved by using finer grid dimensions, increasing coating thickness and adopting multi-layer polarizer structures. The results and method reported in this paper serve as proof of concept for approaching a variety of cost-effective quasi-optical THz components, such as attenuators, polarizers and filters.

4.SUPEROLEOPHOBIC AND CONDUCTIVE CARBON NANOFIBER /FLUOROPOLYMER COMPOSITE FILMS

4.1. Introduction

Stable polymer-particle dispersions suitable for spray casting of nanostructured carbon composite coatings are important for a variety of industries seeking simple methods to apply large-area, functional surface treatments ^[27, 85,105, 151-156]. Such dispersions, when deposited on a suitable substrate and dried, can produce composite films with tunable mechanical, electrical, and hydrophobic/hydrophilic properties. ^[85,105] Select methods for producing dispersions have focused on blending solution-processed polymers or aqueous based polymeric dispersions with dilute nanofiber suspensions. ^[157] Polymers are generally chosen based on their adhesion properties, mechanical strength, and surface energy, while nanoparticle fillers are selected not only to alter surface energy and surface texture, but also to impart additional functionalities, such as electrical conductivity, magnetic actuation, etc. Nanofillers, such as CNTs or CNFs, in order to be combined with polymer dispersions or solutions must be dispersible and stable in liquids, which generally requires the use of either sonication, chemical functionalization, co-solvents or a combination of these techniques. ^[158] CNFs have the advantage of being less costly for industrial scale production. ^[159] But CNFs are also very long (typically > 100 μm) – as compared to CNTs (< 10 μm) - which complicates their solution dispersion and processing. Relatively few works have demonstrated water repellency of composite coatings containing CNFs or CNTs dispersed in fluorinated polymers. ^[105, 160] Moreover, studies demonstrating CNF-based polymer composites with oil repellent properties are lacking.

Herein we report fabrication of novel CNF-fluoropolymer composite films obtained from multi-solvent dispersions comprising formic acid, acetone and water. Prior to blending CNFs into the aqueous-based fluoropolymer dispersion, CNFs are dispersed in a formic acid/acetone solvent system by ultrasonic processing. The fluoropolymer used is a commercially available

fluoroacrylic co-polymer (PMC), which provides better substrate adhesion when compared to traditional perfluorinated polymers, such as polytetrafluoroethylene (PTFE or Teflon). The high-aspect-ratio CNFs used in this work serve two purposes, namely to: a) create hierarchical surface roughness features within the polymer matrix as required for liquid repellency,^[161] and b) add additional functionality of electrical conductivity by a percolated fiber network when present in high enough concentrations. To enable solution dispersion, instead of treating CNFs with strong acids, such as sulfuric or trifluoroacetic acid,^[158] we use formic acid, a relatively weak carboxylic acid, which is completely compatible with the water-PMC dispersion, and hence facilitates efficient mixing of CNFs in polymer dispersions. Using this approach we obtain a number of such dispersions capable of producing superhydrophobic (water sessile contact angle, $CA > 150^\circ$), self-cleaning (sliding angle $< 10^\circ$), and superoleophobic (oil sessile $CA > 150^\circ$) composite coatings when spray cast and dried on either smooth or low-cost textured surfaces (i.e., sand paper). Using sand paper of varying grit sizes, conformal coatings with different concentrations of CNFs were fabricated featuring different micro and nanoscale roughness. Nanoscale features were tuned by using different CNF concentrations in the polymer matrix.

In the following, we study the influence of micro/nanoscale roughness of these coatings on sessile contact angle and roll-off angle for both water and oil. Finally, we demonstrate, as an example, the application of the present technique with an alternative carbon nanofiller; by replacing the long hollow-core CNFs with similar diameter but shorter solid-core carbon fibers (henceforth termed nanowhiskers), PMC-carbon nanowhiskey inks were prepared and ink-jetted producing linear patterns with feature size $\sim 100\mu\text{m}$. These inks can be formulated to display good substrate adhesion and electrical conductivity, in addition to their water and oil repellent properties, which are envisioned for the microelectronics industry. To date, only CNT-based suspensions (no polymer matrix) have been demonstrated for ink-jet applications (e.g. thin film transistors, etc.) with no studies been reported on the wettability or adhesion of the deposited ink patterns.^[162-172]

4.2. Experimental

4.2.1. Materials and preparation of CNF/PMC composite

Carbon nanofibers (PR-24-XT-HHT; Pyrograf III) were obtained from Applied Sciences Inc., USA. These CNFs were hollow with partially cup-and-cone structured graphitic walls and well characterized pretreatment-dependent mechanical properties.^[173] Typical diameter of these as-received CNFs was 100 nm with characteristic length ~130 μm . The PMC was obtained from DuPont as a 20 wt. % dispersion in water (Capstone[®] ST-100). Reagent grade formic acid, acetic acid, and acetone were obtained from Sigma Aldrich (USA) and used as received. Deionized water and mineral oil (White, Heavy; Sigma Aldrich Product #330760; surface tension 28.54 mN/m, density 0.862 g/cc) were used as probe liquids for contact and roll-off angle measurements.

The CNF dispersions were prepared as follows. Initially CNFs were dispersed in formic acid in five different concentrations of 0.5, 1.0, 1.5, 2 and 3 wt. %, using a high power probe ultrasonic processor (Vibra-Cell, VCX-750, Sonics & Materials, Inc.) operated at 70% amplitude for 5 minutes. Subsequently, an equal volume of acetone was added to the CNF dispersions and sonication was continued for another 5 minutes. It was found that sonication not only separated the CNF clusters, but also broke down the initially long fibers to lengths within the range 10-30 μm . Separately, as-received aqueous PMC dispersion was diluted by mixing with formic acid and acetone to obtain a volume ratio of 1:1:2 (20 wt. % PMC in water : formic acid : acetone). Diluted PMC and each of the five different CNF-in-formic-acid dispersions were then mixed in such proportion that the CNF content in the final dispersion was either 10, 20, 30, 40 or 60 wt. % of the PMC polymer. The final CNF/PMC dispersions were applied by spray deposition on microscope glass slides and on sand paper of varying grit sizes corresponding to different microscale roughness. An airbrush atomizer (Paasche, VL siphon feed, 0.55mm spray nozzle) was used to spray the dispersions. Spray cast films were dried at 90°C under a convective air flow space heater for 30 minutes. Care was exercised to control the final thickness of the composite

films on sand paper so that they conform to the micro-texture of the underlying terrain rather than completely smoothen the substrate. Specifically, four spray passes were used to apply thin conformal coatings on sand paper. In this case, an upper bound estimate of the average coating thickness was 5 μ m, as based on the projected area of the substrate (an under-estimation of the actual textured surface area) and the mass of deposited dry CNF/PMC material. Thicker films, on the other hand, required several tens of spray passes over the smooth glass slides used for the electrical conductivity measurements.

Stable PMC-carbon nanowhisiker dispersions for ink-jetting were produced by a similar process. Carbon nanowhiskers (150 nm dia., 6-8 μ m long; were procured from Sigma-Aldrich, USA. The nanowhiskers were first combined with acetone and sonicated for 10 min. Next, acetic acid (an alternative carboxylic acid) was introduced into the suspension and the sonication was continued for another 10 min. Finally, 20 wt. % PMC in water was added to the suspension and sonication was maintained for 10 min. For ink-jetting, the final dispersion was diluted with water to a level such that the collective concentration of carbon nanowhiskers and PMC in the solution was less than or equal to 1.5 wt. %. Ink jetting was performed by a MicroFab JetLab[®] 4XL system equipped with a 60 μ m diameter nozzle.

4.2.2 Coating characterization

Composite film thickness was measured using a calibrated high-quality optical microscope (OLYMPUS-BX51). Conductivity of CNF/PMC composite films deposited on glass slides was measured by a Keithley 6517 electrometer using the two-probe technique. Silver paint electrodes were applied locally on the films to minimize contact resistance between the films and the probes. A JEOL JEM-3010 (300 kV) instrument was used to obtain high resolution transmission electron microscope (TEM) images of the particle fillers. A scanning electron microscope (Philips XL30 ESEM-FEG) was used to analyze the surface morphology of the dry films. A backlit optical image setup employing a high speed camera (Red Lake Motion Pro, USA) and a tilt stage were used to measure sessile droplet CAs and liquid mobility on the composite films. A micro-syringe

was used to dispense 6-8 μl droplets of deionized water or mineral oil on the treated surfaces. Measurements were carried out by placing sessile water or oil droplets on a horizontal surface and subsequently tilting it until roll-off occurred. The droplet roll-off angle was defined as the minimum tilt angle required for droplet rolling. In many cases, especially with oil, roll-off did not occur even at 90° tilt. At least ten different CAs and roll-off angle measurements were made at different locations on each of the CNF/PMC composite coatings.

The present approach relies on static CA to designate super-repellency and on droplet roll-off angle to assess liquid mobility (the ability of a surface to shed liquid). The static value of CA is smaller than its advancing counterpart, which is suggested ^[174] as a more reliable measure of repellency. To this end, the value of static CA offers a more conservative criterion for super-repellency (i.e. $\text{CA} > 150^\circ$). As also reported in Reference 174, liquid mobility correlated with the difference between the forward (maximum) and rear (minimum) CAs in a sliding droplet configuration on an inclined plate. However, this approach is not possible in the present study, as in many cases the droplets (especially oil) did not slide down the tilted surfaces, but rather remained stuck to them. We thus resorted to measure droplet roll-off angle, which offers an unambiguous criterion of liquid mobility on a surface when droplet rolling occurs.

4.3. Results and discussion

4.3.1. Dispersion considerations

Superoleophobic composite design and fabrication is considerably more difficult to achieve than superhydrophobicity, mainly because the former requires the creation of special hierarchical surface texture using very low surface energy materials.^[175] For instance, micro-roughness having high degree of tip curvature, such as micro hoodoos or mushroom like features, is required instead of simple micron sized beads (bumps) so that low surface energy liquids (e.g. oils) can be maintained at a metastable Cassie-Baxter (non-wetting) state rather than the Wenzel (wetting) state. High-temperature-treated CNFs having highly graphitic walls are inherently hydrophobic.

^[176] Practically, high aspect ratio nanostructured materials can be self-assembled or grown into

hierarchical structures (in the absence of a binding polymer matrix), which can display self-cleaning behavior, also known as the lotus effect.^[177] In general, however, due to their high surface energy, such nanostructured materials (such as exfoliated clay platelets) need to be surface functionalized with hydrophobic macromolecules to display the lotus effect. Nanostructured carbon materials, such as CNFs and CNTs, can assemble into such structures provided that they are carefully grown in a unidirectional manner on select surfaces (i.e., CNT nanoforests on silicon wafers) from precursors using vapor deposition.^[178] But these structures are delicate and lack durability due to the absence of an embedding and adherent polymer matrix. Simple and cost-effective techniques to fabricate durable and reusable CNF- or CNT-in-polymer composite films displaying the lotus effect are being sought because these nanomaterials are also electrically conductive.^[179] There are two main problems to overcome: a) Difficulties in creating efficient and stable dispersions of long CNFs in a suitable solvent/polymer system, and b) identifying the right combination of surface morphology and surface energy of polymer matrix and filler material to cause lotus behavior. Owing to the hydrophobic nature and high aspect ratio of high-temperature-treated CNFs, their direct dispersion in water alone is very challenging. Addition of polar and water miscible solvents, such as acetone, may improve dispersion, but even in that case, CNFs begin to agglomerate and precipitate in solution at a fast rate. It has been reported^[158] that introduction of TFA (trifluoroacetic acid) as a co-solvent improves the stability and dispersibility of CNTs in various organic solvents. In the present case, we demonstrate good performance with a much less aggressive carboxylic acid, namely formic acid, as co-solvent to disperse long CNFs efficiently. CNFs can be dispersed in formic acid to a certain extent. They still form large agglomerates in time, which practically hinders casting of films of uniform morphology. To this end, it is important to choose a polymer that will not only provide liquid repellency for the resulting composite coating, but also facilitate a high degree of CNF dispersibility and stability in the continuous phase prior to spraying. The PMC polymer used in the present work has amine-based acrylic cationic (hydrophilic) and fluorinated (hydrophobic)

segments.^[180] The acrylic segment promotes better adhesion, as compared with its liquid-repellent, perfluorinated counterpart. In the presence of water, the hydrophobic side chains of the polymer tend to orient towards the hydrophobic wall of the CNFs (Fig. 47). The pH value of the dispersion has a critical role in charging of cationic segments associated with the PMC chemistry, and hence on the stabilization of the dispersion. In the absence of formic acid, the pH is very close to neutral as only water and acetone co-solvents are present in the dispersions. Under such nearly neutral pH conditions, the polymer is not properly ionized, and as a result, the CNFs tend to come close to each other and eventually form large aggregates in the co-solvent, as schematically shown in Fig. 47 (top row).

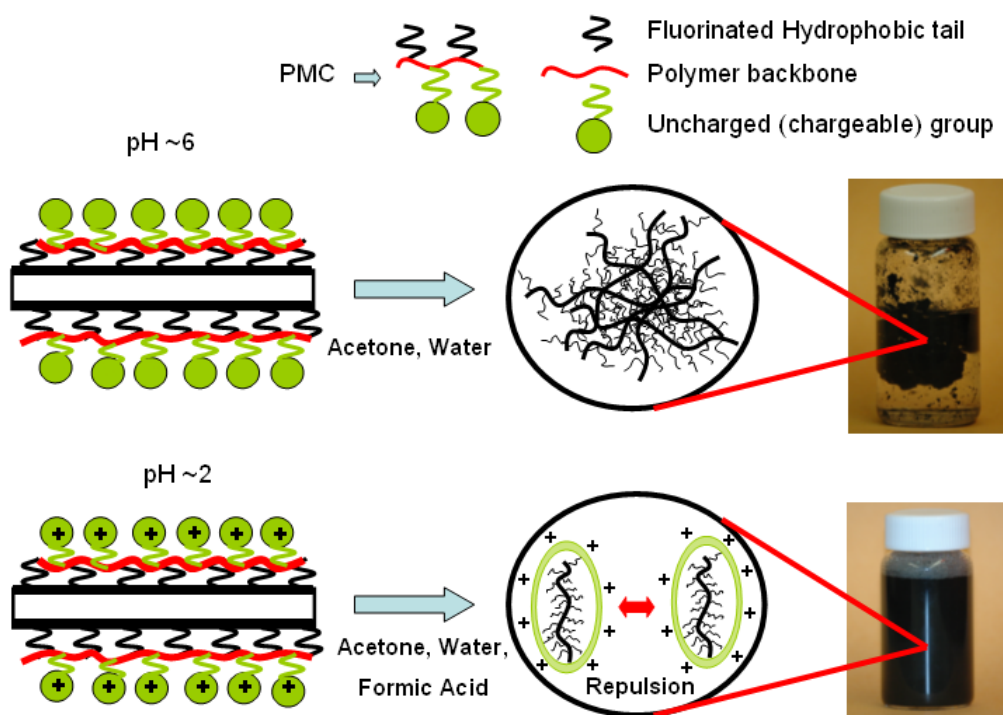


Figure 47: Schematic of the effect of formic acid on CNF dispersion stability. CNFs phase separate in the absence of formic acid (top panel), whereas CNFs disperse and produce ink like stable dispersions (bottom panel) in the presence of formic acid.

Introduction of formic acid into the system reduces the pH of the multicomponent solvent and starts ionizing the PMC. This allows CNFs with adsorbed PMC to be stabilized and separated by charge repulsion forces, which oppose hydrophobic interactions. Thus, aggregated CNFs start to disperse in the suspension after formic acid addition (Fig. 47 bottom row). Ultrasonic processing drastically improves this dispersion further by breaking up the aggregated CNFs.

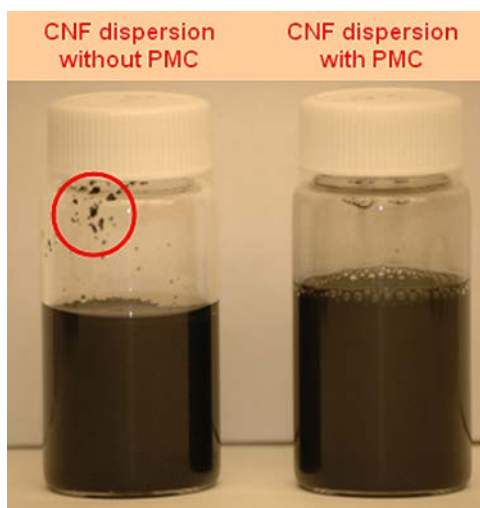


Figure 48: Role of PMC during CNF dispersion in acetone, formic acid and water mixture. (Left) Without PMC, large aggregates form (red circle); (Right) With PMC, superior CNF separation prevents aggregate formation.

To further assess the role of PMC on CNF dispersion quality in the acetone/water/formic acid solvent system (continuous phase), dispersions were prepared with formic acid as described above, but without PMC. The left vial in Fig. 48 contains a dispersion with 1 wt. % CNF in an equal volume mixture of acetone, water and formic acid. When the vial was shaken mechanically after the dispersion was prepared, small CNF agglomerate deposits started to appear on the vial walls (red circled region in Fig. 48). Although the size and occurrence frequency of these agglomerates is much smaller than that in water or water/acetone mixtures in the absence of PMC, these agglomerates drastically reduce sprayability. On the other hand, when the CNF

dispersions were prepared with PMC, no aggregate deposits on the vial walls were noticed (see right vial in Fig. 48) and dispersion sprayability was very efficient and repeatable. It is thus concluded that the role of PMC in obtaining an aggregate-free suspension is critical.

Analysis of TEM images (Fig. 49) of CNFs extracted from PMC-free (control) and PMC-containing dispersions indicate that PMC forms a thin polymeric layer on the CNF walls (Fig. 49.b), which can further facilitate CNF dispersion. In the presence of formic acid in solution, adsorbed PMC could be charged since the pH of the continuous phase is lowered by the acid. In other words, the presence of formic acid increases the cationic behavior (pH \sim 2.3) of the adsorbed polymer layer, which in turn, makes the CNF walls positively charged. Hence, CNFs start to repel each other and thus overcome the forces associated with hydrophobic interactions, eventually dispersing efficiently in the continuous phase.^[114] It is important to note that formic acid did not chemically functionalize or oxidize the CNF walls, as indicated by the absence of distortions on the walls of formic acid-treated CNFs (Fig. 49.a). Such distortions have been previously observed after exposure of CNFs to nitric acid.

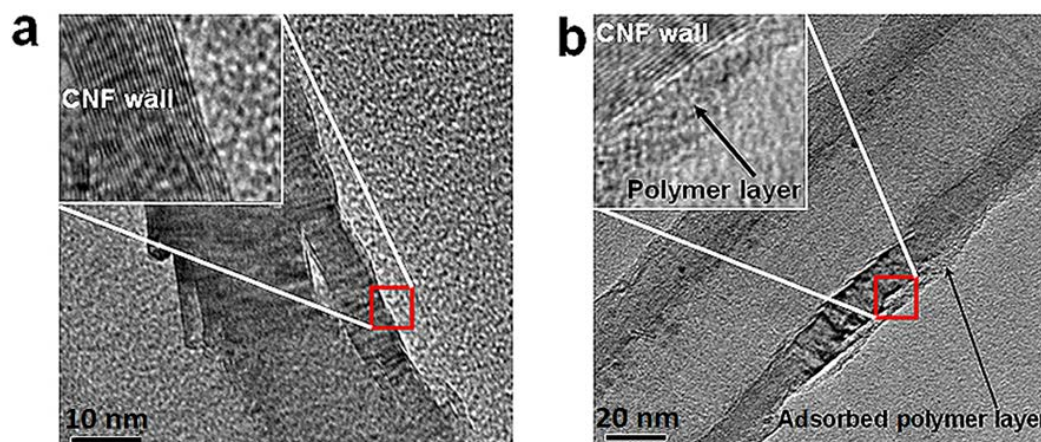


Figure 49: High resolution TEM image of CNF walls (a) after formic acid treatment; inset shows enlargement of intact graphene layers of CNF wall, indicating no chemical modification; (b) after treatment with formic acid and fluoropolymer dispersion diluted to 0.01 wt%; inset shows detail of polymeric layer adsorbed over the outer CNF wall composed of intact graphene layers.

4.3.2. Coating surface morphology

The surface micro morphology of a thick (150 μm) composite film deposited on smooth paper and containing 25 wt. % CNFs in the PMC polymer matrix is shown in the SEM micrographs of Fig. 50. The film surface appears to be made up of randomly distributed micro bumps of different sizes and shapes (Fig. 50.a) resembling the lotus leaf surface morphology. Surprisingly, the higher magnification image (Fig. 50.b) indicates that these bumps are in fact made up of CNF bundles bound together by the polymer matrix. Therefore, CNFs form the required re-entrant, sub-micron roughness features within the larger (micron-scale) texture in these composites, thus causing high static water/oil contact angles.

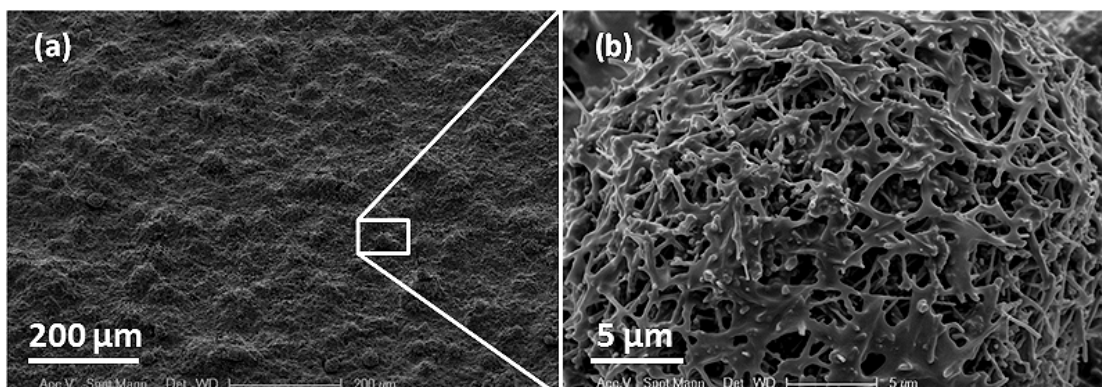


Figure 50: Scanning electron microscope images showing surface morphology of a thick coating (on smooth paper) comprising 25 wt. % CNFs within the PMC polymer matrix. (a) Low magnification surface topology, and (b) enlargement of sub-micron surface roughness due to CNF bundles held together by the polymer.

4.3.3. Large-area coating wettability and effect of underlying substrate roughness

The liquid repellent properties of spray cast CNF/PMC composite coatings applied on glass slides and having varying CNF concentrations are reported in Fig. 51.a, where static water and oil contact angles are plotted along with water and oil droplet roll-off angles as a function of CNF concentration (in wt. % of the dried composite coating). For both water and oil, sessile contact

angle increases and levels off with increasing CNF content. A transition from hydrophobic to superhydrophobic state is observed when CNF concentration reaches 30 wt. %. The same trend is apparent for oil, where superoleophobicity ($CA > 150^\circ$) is reached at 60 wt.% CNF concentration.

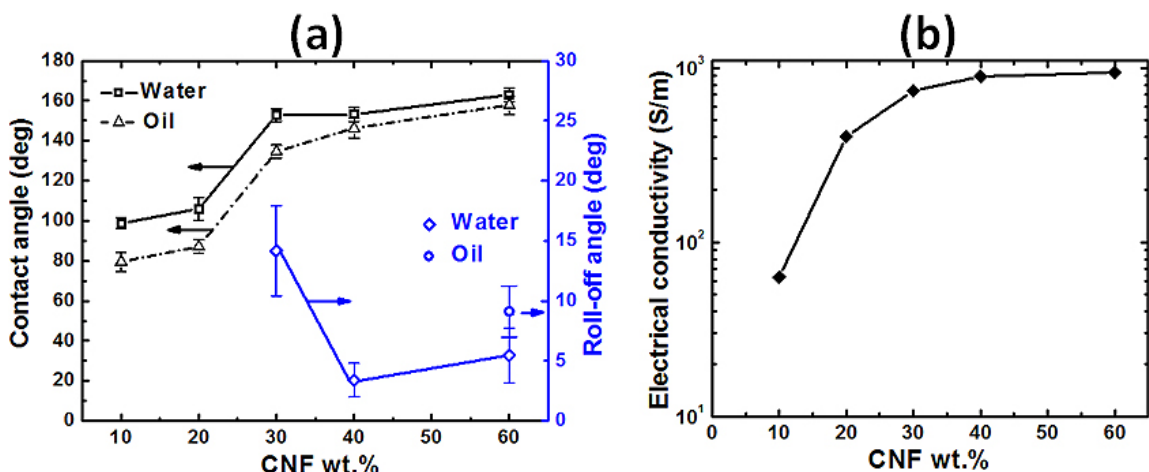


Figure 51: Variation of (a) sessile contact angle and droplet roll-off angle for water and oil, and (b) electrical conductivity with CNF loading for thick composite coatings applied on smooth glass slides.

Water droplet mobility (rolling) is observed at a minimum CNF concentration of 30 wt.%, but the roll-off angle is about 14° , slightly above the acceptable range for self-cleaning behavior (below 10°). At CNF concentrations above 30 wt.%, the water roll-off angles are well within the self-cleaning regime. Oil droplet mobility is observed only at 60 wt.% CNF loading, with the roll-off angle $\sim 9^\circ$ indicating self-cleaning behavior. In lower CNF loadings, the coatings display a “sticky” oleophobic surface (no droplet rolling) even when static CAs reach almost up to the superoleophobic threshold (for example at 40 wt.%). These films also display the additional functionality of electrical conductivity (Fig. 51.b); this quantity increases from 63 S/m (at 10 wt. % CNF) to 940 S/m (at 60 wt. % CNF) being well within the electromagnetic interference (EMI) shielding range.^[105]

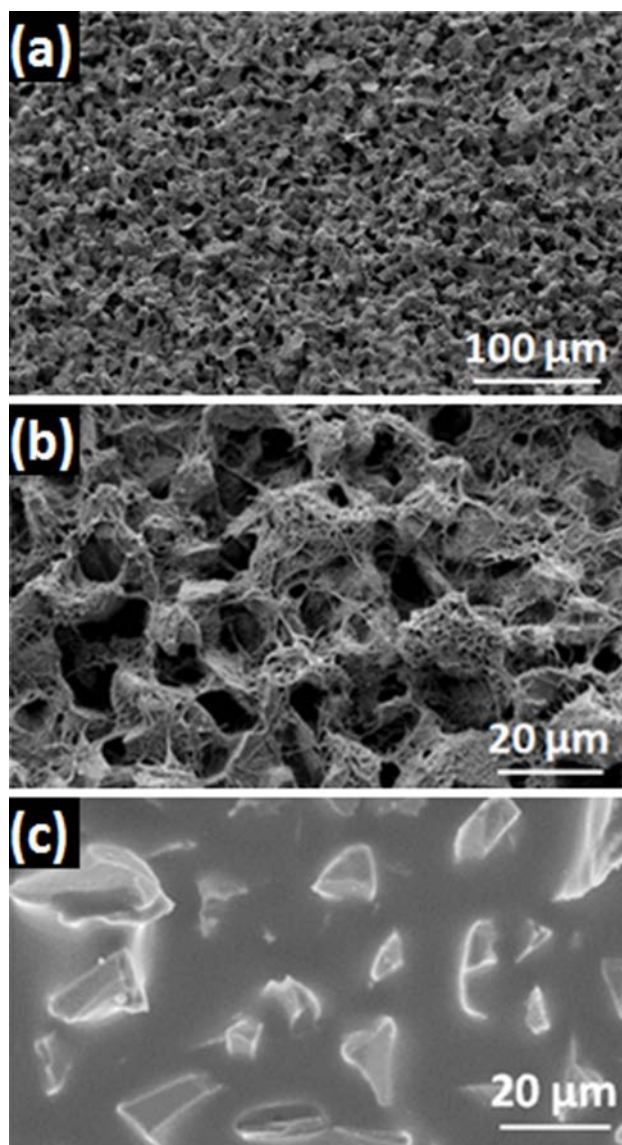


Figure 52: (a) Scanning electron microscope image showing morphology of a conformal superhydrophobic CNF/PMC composite (25 wt. % CNF in total solids) spray-deposited on a 600 grit sand paper (average roughness 15 μm). (b) Higher magnification image showing coverage of sand paper micro roughness with the CNF/PMC composite web. (c) SEM image showing surface morphology of the bare 600 grit sand paper.

In order to study the effect of underlying substrate roughness on coating repellency, thin conformal coatings were deposited on silicon carbide sand papers of different grit sizes. Sand papers of grit size 280, 600, 1200 and 1500 were used for this purpose with corresponding mean surface roughness of 45, 15, 9, and 5 μm respectively. Figures 52.a, b display the morphology of

a 25 wt. % CNF-containing polymer composite coating deposited by spray on a 600 grit sand paper substrate. Highly microporous polymer films with pores separated by thin polymer walls (sponge-like) are known as polymer foams; the associated surface morphology is commonly referred to as microcellular morphology.^[181] Formation of such microcellular morphology is seen in Figs 52.a, b and is attributed to the underlying substrate roughness, as compared to the morphology on a smooth glass substrate (Fig. 50.a) which is lacking the micro-porous feature. Figure 52.c displays the same 600 grit sand paper substrate in its bare state. In order to allow SEM observation, the sand paper sample was first coated with a 5-nm thick layer of platinum/palladium. Comparison of Figs 51.b and 51.c reveals the conformal character of the deposited CNF/polymer film.

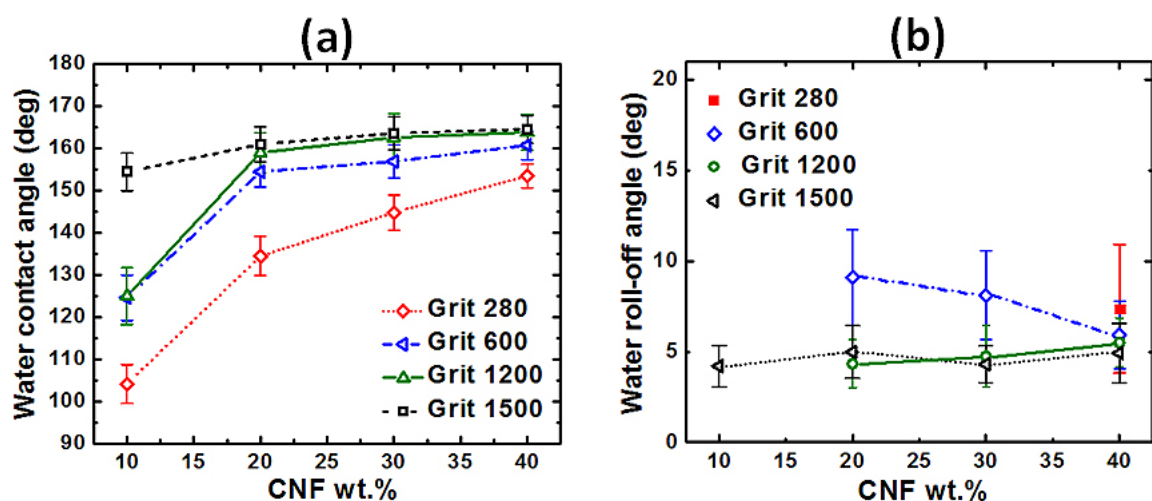


Figure 53: Variation of water (a) sessile contact angle and (b) droplet roll-off angle with CNF loading for conformal composite coatings deposited on sand papers of different micro-roughness (grit size in legend). Increasing grit size indicates reduced roughness.

Detailed water sessile contact angles and droplet roll-off angles as a function of CNF concentration in total solids and substrate roughness are presented in Fig. 53. For any given composition, water CA increases with decreasing mean substrate roughness, while water droplet

mobility increases (i.e. roll-off angle decreases) with decreasing roughness. In particular, significant changes are observed when the mean substrate roughness reduces from 45 μm to 15 μm for all composite films. Only for the finest sand paper (5 μm mean surface roughness), superhydrophobic self-cleaning behavior is observed at all CNF loadings. For the roughest substrate with surface roughness of 45 μm , superhydrophobic self-cleaning behavior is attained only at the highest CNF loading (40 wt.%). For the other two substrates with mean surface roughness between 9 and 15 μm , self-cleaning superhydrophobic behavior is observed for CNF concentration at or above 20 wt. %, as compared to the 30 wt. % threshold required for such behavior on the films applied on smooth glass substrates (Fig. 50). This observation confirms the importance of underlying substrate texture on superhydrophobic behavior.

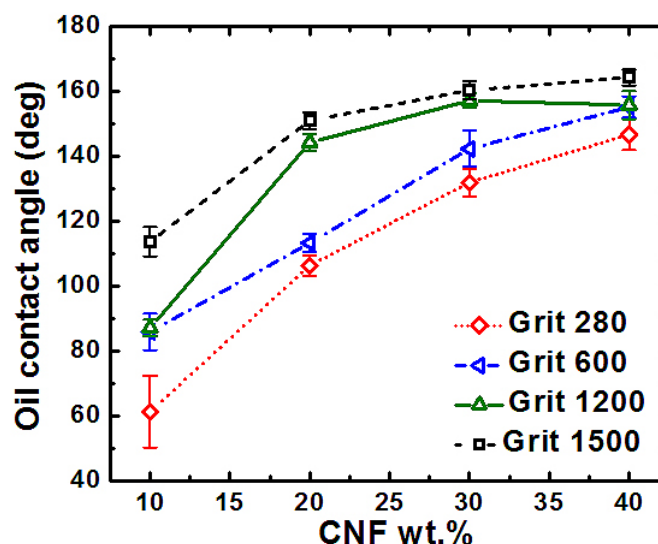


Figure 54: Variation of oil static contact angle with CNF loading for conformal composite coatings deposited on sand papers of varying micro-roughness (grit size in legend).

In the case of oil repellency (Fig. 54), for substrate roughness below 15 μm , significant jumps in static CAs are observed as the CNF concentration rises from 10 wt. % to 20 wt. %. On sand papers with grit sizes of 1200 (9 μm mean roughness) or 1500 (5 μm), composites with CNF

concentrations near or above 20 wt. % resulted in superoleophobic behavior with static oil CAs exceeding 150° . However, oil mobility on these apparently superoleophobic films was not observed (no droplet rolling even at 90° tilt angles), thus classifying these films as “sticky” superoleophobic composites. We argue that this behavior is due to the disappearance of microcellular structure when the mean substrate roughness decreases. Based on an earlier study of PMC/zinc oxide composites,^[152] self-cleaning superoleophobic behavior was observed when the PMC polymer matrix assumed microcellular structure, as created by a controlled solvent inversion technique during spray atomization.^[152]

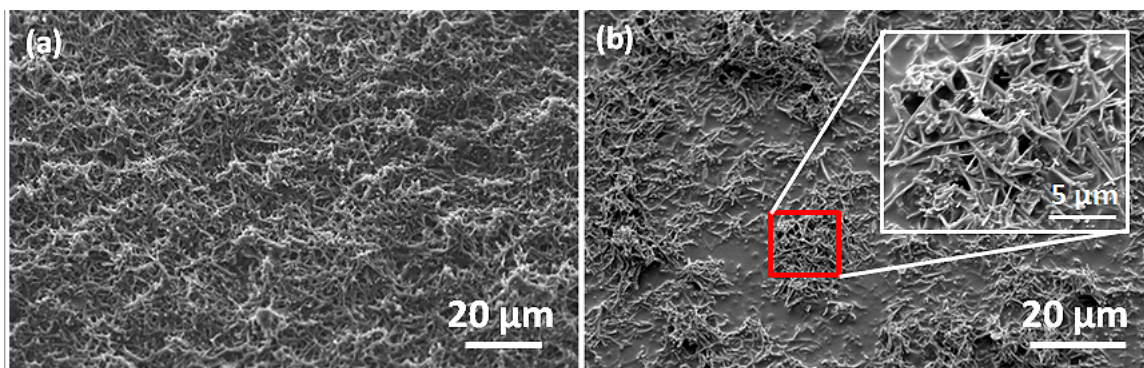


Figure 55: Scanning electron micrographs showing surface morphology of CNF/PMC (25 wt. % CNF in solids) composite films spray cast and dried on (a) 1200 grit, and (b) 1500 grit sand paper surfaces. The inset in (b) shows an enlargement of the red marked area.

Inspection of the ESEM micrographs in Fig. 55 indeed shows that the microcellular morphology is absent on coatings applied on the 1200 and 1500 grit (finest) substrates. As mentioned earlier, self-cleaning, low-surface-tension liquid (oil) repellency can only be achieved when dual-scale (micro/nano), uniformly-distributed roughness features with strong surface curvatures are created on very low surface energy (perfluorinated) surfaces. Absence of such features on the 1200 and 1500 grit surfaces in Fig. 55 probably causes increases in oil CA hysteresis, although the existing surface texture -due to randomly assembled CNFs in the PMC

polymer matrix- appears to be sufficient to cause high static oil CAs. Nonetheless, even though the corresponding static oil contact angles are high, oil droplets tend to stick on these coated surfaces.^[182]

4.3.4. Microscale application: Ink-Jet printed patterns

Inkjet printing is an attractive method for depositing spatially alternating wettable and non-wettable patterns.^[183] The dispersions developed for the CNF/PMC composite fabrication cannot be used for ink-jet printing purposes, as the long CNFs cause frequent device orifice clogging. Instead, we produced carbon nanowhisker-PMC ink suspensions and generated conducting and liquid repellent line patterns with feature size of 100 μ m. Figure 56 shows ink-jet printed superhydrophobic micro-ribbons generated on a Mylar substrate from a dilute carbon nanowhisker/PMC (wt. ratio of 1:1) dispersion. The printing was performed in the drop-on-demand mode at a dispensing frequency of 500Hz. The device orifice diameter was 60 μ m, and generated monodisperse droplets with diameters in the range 70-75 μ m. The spot pitch was maintained constant at 40 μ m, translating into a printing speed of 20mm/s. The distance of the device orifice from the substrate was 0.5mm. Although the dark streaks in Fig. 56 show spatial non-uniformities caused during drying (coffee stain effect^[143]), the lines were confirmed to be conductive. The intermittent area in between the dark lines in Fig. 56 has the wetting properties of the underlying substrate, thus requiring no further treatment.

The example of Fig. 56 shows the potential of the present technique, but also displays the spatial uniformity challenges that must be overcome when applying these linear patterns.^[184,185] Such patterns may be of value in microelectronic applications where conductive lines need also be liquid repellent. These composite lines are both electrically and thermally conductive due to presence of CNFs as filler. Patterning these composite films in specific geometric shapes, different non-metallic electromagnetic devices (such as polarizers, band-pass filters, etc.) can be

prepared; due to their high liquid repellency, these devices will be corrosion resistant, offering an advantage over metals.

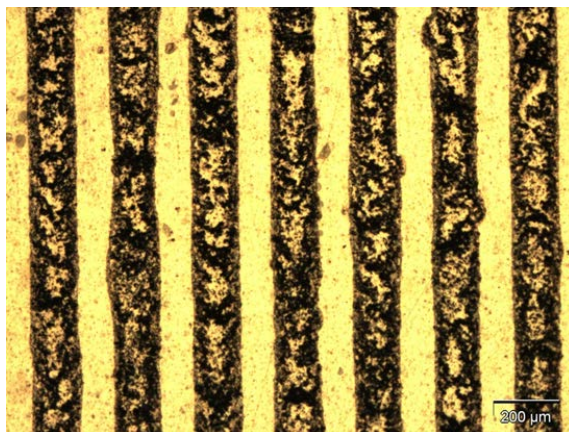


Figure 56: Hydrophobic and conducting carbon/fluoropolymer composite lines printed on a hydrophilic Mylar substrate (yellow background) from a dilute carbon nanowhisker/PMC solution using an ink-jet nozzle of 60 μm dia. The carbon nanowhisker concentration in the dried composite film is 50 wt. %. The dark areas depict high content of nanowhiskers, while the bright areas indicate lack of the particle filler.

5. CARBON NANOFIBER-MAGNETIC NANOPARTICLE NANOHYBRID AND ITS APPLICATION IN FABRICATION OF POLYMER NANOCOMPOSITE OF HIGHLY ANISOTROPIC PROPERTY.

5.1. Introduction

Many novel properties of hollow cylindrical structures filled with inorganic materials have motivated researchers to investigate such nanohybrid/nanocomposite materials in different areas of nanotechnology,^[186-191] drug delivery and medical devices,^[192,193] field ionization,^[194] electrochemistry^[195-197], hydrogen storage^[198] and memory devices,^[199] sensors,^[200,201], nanoreactors,^[202-204] probes^[205] and catalysis,^[202,206] etc. CNTs and CNFs, among the most investigated hollow cylindrical structures, possess exceptional mechanical, thermal and electronic properties.^[207] The term CNT is used herein to define short (up to a few microns) hollow carbon structures, while the term CNF is reserved for typically longer (several tens of microns) carbon structures. The hollow cavity of CNFs and CNTs can be filled ^[36] with other materials to synthesize a whole new class of nanohybrids well-suited for specialized applications. Owing to their graphitic structure, CNTs and CNFs ideally serve as chemically inert, passive cylindrical containers, which makes them most suitable for hosting metal or metal oxide nanoparticles,^[36] magnetic nanoparticles,^[36] fluorescent nanoparticles,^[208] polymers,^[209] C₆₀ molecules,^[37,210] organic molecules,^[211,212] etc.

To design a novel nanosystem with desirable properties, it is often required to combine different intercalated nanostructures, each with its own unique properties. The properties of each filling constituent in such nanohybrids can be retained or even enhanced upon intercalation within the host structure. Additional properties or functionalities can also be imparted by the nanoscale interaction between the host shell and the intercalated material. Several approaches have been reported in the literature to encapsulate various nanophase materials inside the hollow cavities of CNTs and CNFs. Metal-based materials have been added to the hollow cavities of CNTs and

CNFs by arc discharge growth of carbon nanotubes,^[213,214] volatile metal complex filling and decomposition,^[215] and capillary suction^[216-220] of molten metal salts. Although functionalization of outer and inner surfaces of CNTs using organic chemistry techniques^[37,221,222] have allowed efficient filling with metal nanoparticles, the related methods are frequently complex and difficult to scale up. As compared to CNTs, CNFs have several advantages, including their relatively high electrical and thermal conductivities, thick/strong walls, low cost, etc.

Nanoparticles frequently exhibit size-dependent physical, thermal, electrical and chemical properties;^[223,224] consequently, these properties may be significantly affected/compromised by the encapsulation techniques. To potentially overcome complications in interpreting measurements involving encapsulated particles with diverse sizes, recent studies^[40,202,225] have intercalated preformed nanoparticles of *uniform* size in the CNTs and CNFs. Compared to CNTs, CNFs are better suited for this approach because of their comparatively large hollow cavity (~30-70nm inner dia.), which allows the nanoparticles to invade more easily as compared to CNTs which have narrower diameters. On the other hand, the much longer CNF lengths make it more difficult to attain efficient packing of the intercalated particles, thus requiring additional processing steps (e.g. ultra-sonication).

Among the many types of nanoparticles encapsulated inside CNTs, magnetic materials in CNTs have been reported;^[36,226,227] however, no report of magnetic nanoparticles intercalated inside CNFs has been published so far. Recently, research articles have appeared on synthesizing gold^[40] and other metal^[228] nanoparticles *inside* the CNF cavity using complex chemical routes, which result in very low packing efficiencies. Encapsulation of magnetic nanoparticles in CNFs averts adverse environmental effects, such as oxidation or other chemical/physical modification, which may lead to deteriorating properties of such nanocomposite materials when targeted for electrical or magnetic applications.

In this study, we report a novel nonchemical technique to encapsulate magnetite (Fe_3O_4) nanoparticles of uniform size (average $\sim 10\text{nm}$) into vapor grown CNFs by ultra-sonication assisted capillary imbibition and self-sustained diffusion. It is an efficient, physical method to achieve comparatively dense packing of these nanoparticles inside the hollow cavities of the fibers. CNF filling was achieved by capillary imbibition and diffusion-driven concentration gradients established during solvent evaporation from the dispersion. The paper reports a systematic study of the processing parameters, such as concentration and ratio of CNFs to magnetite nanoparticles, dispersant medium, type and duration of ultrasonication, and drying temperature. CNFs loaded with densely packed magnetite nanoparticles have been attained by controlling these process conditions. Such hybrid materials may find applications as nanofillers in magneto-active or electro-active functional polymer nanocomposite metamaterials with anisotropic mechanical, thermal, electrical or magnetic properties, magnetic-field controlled heat transfer nanofluids, sensors, opto-electro-magnetic devices, etc. The present technique could also prove useful for studying other dispersible nanomaterials by facilitating future studies of nanoscale confinement.

5.2. Materials and processes

Two types of commercially available hollow-core CNFs (Pyrograf III, Pyrograf Products Inc., USA) were employed in this study; CNFs heat treated either at 1500°C (PR24-XT-LHT) or at 3000°C (PR24-XT-HHT). Both types of CNFs were produced from pyrolytically stripped carbon nanofibers, which featured thick walls of poorly ordered pyrolytic carbon formed during the synthesis process. The poorly ordered walls were graphitized by subsequent heat treatment (at the manufacturer) leading to quasi defect-free walls. Most of the CNFs used in this study were open ended and had mechanically strong wall structure. Both CNF types had 100nm average outer diameter and $10\text{-}30$ micron length (reduced lengths from the as-received state after 10 minutes of bath sonication). LHT fibers had larger inner diameter (90% have $45\text{-}70\text{nm}$) as compared to the

HHT fibers (90% have 20-40nm). The LHT fibers had short-range order in their wall structure, whereas HHT fibers featured highly graphitic walls.

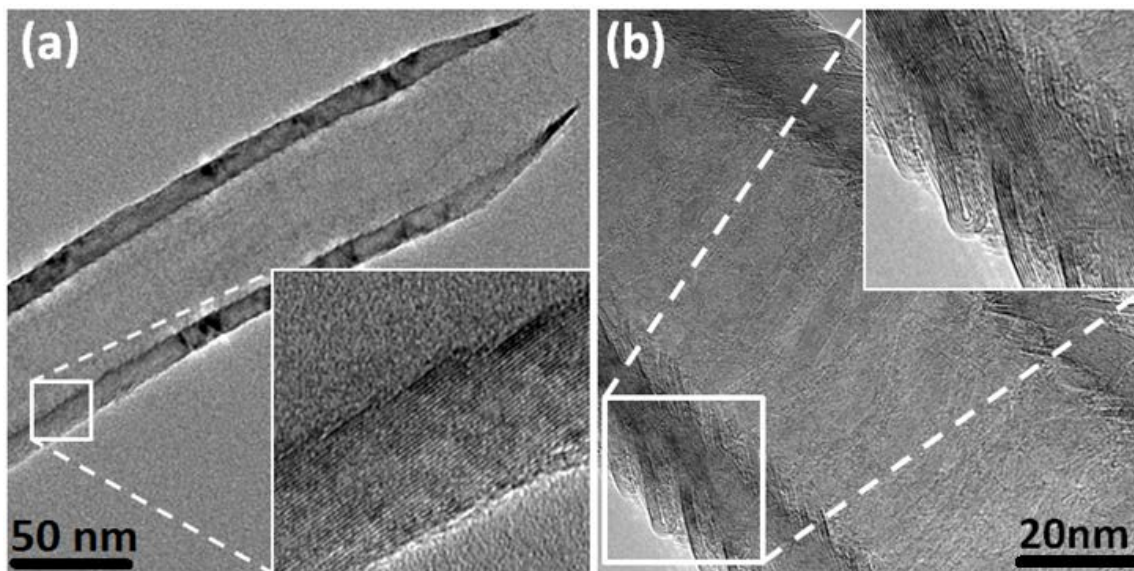


Figure 57: HRTEM micrographs showing portions of: (a) 1500°C-treated (LHT) CNF, and (b) 3000°C-treated (HHT) CNF. The insets show magnified details of the graphitic wall structure for each fiber.

The HRTEM images in Fig. 57 show both types of CNFs (LHT in a, HHT in b) along with structural details of their walls, which consist of stacked cones of graphene layers at an angle to the fiber axis (herringbone structure). Due to their higher degree of graphitization, HHT fibers have higher thermal and electrical conductivity than the LHT CNFs.^[34] The stacked cones create a ratchet-like morphology along the CNF inner wall surface, which serves as an anchor for the nanoparticles reaching the CNF channels. Details of the CNF structure have been discussed elsewhere.^[34] The surfaces of HHT-CNFs (surface energy as per manufacturer is ~135mN/m) are more hydrophobic than the LHT-CNFs (surface energy ~155mN/m).^[229] In view of their larger inner dia. and lower hydrophobicity, LHT nanofibers were preferred for nanoparticle intercalation.

Oil based EMG-911 and water based EMG-508 Ferrofluids (Ferrotec Inc. USA) were used as source of single-crystal superparamagnetic magnetite (Fe_3O_4) nanoparticles (average size 10nm), which were diluted in either toluene (ACS grade $\approx 99.9\%$, Fisher Scientific), acetone or water. The magnetite nanoparticles in EMG-911 were functionalized by the manufacturer with fatty-acid molecules to assist long term stability. In the case of water-based EMG-508 Ferrofluid, a low molecular weight anionic surfactant was included as dispersant. Dry magnetite particle powders were obtained from NanoAmor and had a characteristic particle size of 15-20nm. Bath ultrasonication (Cole-Palmer Model No: 08895-04, USA, 40kHz, 70W) and probe sonication (Sonics, Vibra-cell, Model VCX 750, 20kHz, 750W) were used to prepare the dispersions and facilitate the imbibition of the nanoparticles in the CNF cavities.

5.2.1. Dispersion procedures

1 to 10mg of CNFs were dispersed in 20ml liquid (toluene for oil-based Ferrofluid, acetone or water for water-based Ferrofluid) and bath sonicated for 10 min. Magnetite nanoparticles were added to the respective CNF dispersion either before or after the second sonication step, which featured bath sonication or probe sonication (70% amplitude), each maintained for few seconds to 360min based upon the design of experiment to resolve the influence several process parameters. To investigate the importance of nanoparticle material dispersion properties, Ferrofluid magnetite nanoparticles were substituted by 2.5 mg of dry uncoated magnetite nanoparticles added into the dispersion of 10mg of LHT-CNF in 20ml toluene.

5.2.2. Drying of suspensions

The sonicated suspensions, as produced by the above-mentioned steps, were dried either at room temperature or at 120°C (hotplate, Cimarec, USA) inside a chemical fume hood until all the solvent had dried out. Upon complete drying, a black powder deposit was obtained consisting of CNFs with magnetite nanoparticles.

5.2.3 Washing of dried powder to remove nanoparticles from CNF wall exterior

Intercalated CNFs also carried adsorbed magnetite nanoparticles on their exterior surfaces which were remained attached by molecular forces. The dried CNF and nanoparticle hybrids were subsequently suspended in toluene (when EMG-911 Ferrofluid was used), or acetone or water (for EMG-508 Ferrofluid) to remove the magnetite nanoparticles from the CNF outer surfaces by means of bath sonication (1-30min). The effect of sonication time was evaluated (in terms of removal of the exterior particles without apparent effect on the intercalated nanoparticles), and 15min was found to be optimal. As such, this cleaning time was used in most experiments. Unless otherwise mentioned, 10mg of CNF, 20 ml toluene, 4.16 mg of magnetite (from EMG-911) and 120°C drying temperature were used in the experiments.

5.3. HRTEM characterization of filled CNFs

Dilute dispersions of nanoparticle-encasing CNFs with cleaned outer surfaces were deposited on TEM lacy carbon 300 mesh copper grids. The weight percentage of CNFs in the dispersions was approximately 0.003%. A cellulosic tissue paper was placed beneath the TEM grid to absorb the solvent quickly and facilitate drying. Subsequently, HRTEM analysis was carried out in a JEOL-3010F (300 kV e-beam) transmission electron microscope. The filling efficiencies of CNFs obtained from different experiments were determined qualitatively from TEM images. HRTEM characterization was performed both in normal and tilt specimen modes. Tilt mode analysis was needed to distinguish whether the magnetite nanoparticles were encapsulated inside the CNFs or were attached to the exterior CNF wall surface.

5.4. Results and discussion

5.4.1. Effect of nanoparticle dispersibility

In order to assess the influence of nanoparticle dispersibility on intercalation efficiency we performed experiments using magnetite nanoparticles supplied either in Ferrofluids or in dry

nanoparticle powders. 5mg of magnetite nanoparticle (from EMG-911) was diluted in 20ml of toluene. The final solution contained approximately 0.015 wt.% of magnetite nanoparticles. Separately, 2.5mg of dry magnetite nanoparticle powder was dispersed in 20ml toluene by probe sonicating for 5min. Subsequently, 10mg of PR-24-XT-LHT CNFs were added in each of these two dispersions, which were then bath sonicated for 30min, and subsequently probe sonicated for 10min. Toluene was then dried from these two dispersions by heating at 120°C. After 24 hours, the solvent had completely evaporated, leaving behind a black solid deposit. These solid deposits were then redispersed in 20ml toluene and bath sonicated for 5min; this step was intended to wash away most nanoparticles attached to the CNF wall exterior. 2-3 drops from each dispersion were then deposited on lacey carbon film supported on copper TEM grids for subsequent HRTEM analysis.

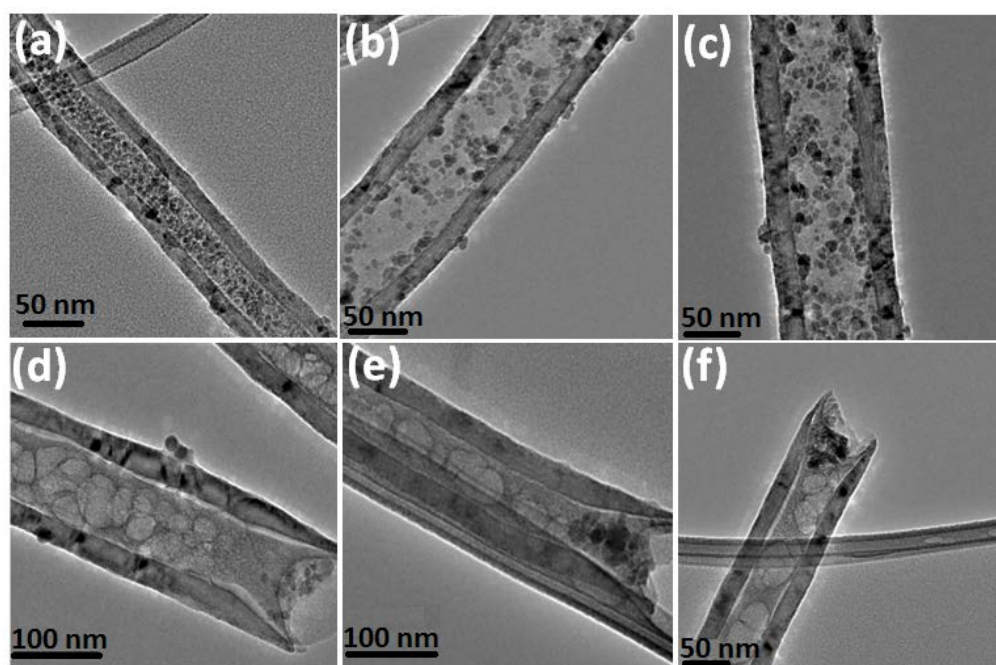


Figure 58: HRTEM images of CNFs containing magnetite nanoparticles originating from: (a-c) EMG-911 Ferrofluid; (d-f) non functionalized, dry magnetite nanoparticle powder. The liquid dispersant used in both cases was toluene. The cellular structures seen in the CNF cavity in (d-f) were created by the drying of the solvent that had imbibed into the CNF cavity. The edges of the supporting carbon film are visible in (a), (b) and (f).

Nanoparticle intercalation from the Ferrofluid-based dispersion (Fig 58.a-c) is visibly higher than the dry-nanoparticle-based dispersion (Fig 58.d-f). In the latter case, the nanoparticles reached only the CNF ends (some time blocking them), while in the former case, the nanoparticles were present along the entire CNF length at high concentrations. The stability of the two respective nanoparticle dispersions inside closed vials was examined using 10mins of probe sonication and 10 mins of wait time. The EMG-911 magnetite nanoparticles are surface-functionalized with fatty-acid molecules, which makes their dispersion in toluene very stable in the long term (as confirmed in Fig. 59.a). In the case of the non- functionalized, dry powder magnetite nanoparticle dispersion, the nanoparticles start to sediment within minutes after the completion of the sonication step (Fig. 59.b).

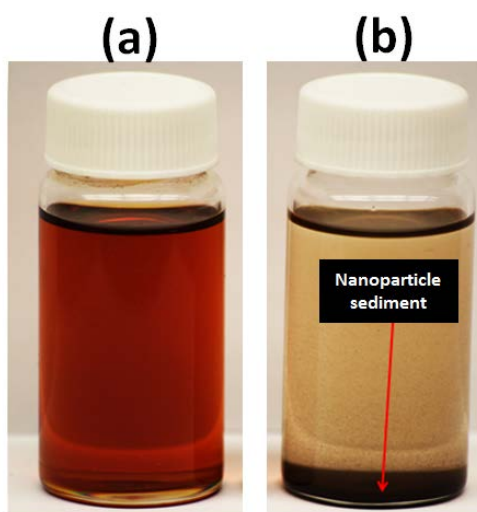


Figure 59: Visual comparison of magnetite nanoparticle dispersions (in toluene) prepared with: (a) functionalized nanoparticles supplied in EMG-911 Ferrofluid, and (b) non-functionalized dry powder nanoparticles. The dispersions were subjected to 10 min of probe sonication, and left to sit for 10 minutes before the two images were taken.

In turn, when nanoparticles are stably dispersed in the liquid medium, the number of collisions between the nanoparticles and the CNF open ends remains high, thus raising the intercalation efficiency; see Fig. 58(a-c). The well dispersed nanoparticles easier penetrate further into the

CNF cavity, which is completely wetted by the toluene. For the non-functionalized nanoparticles, the formed clusters are not as agile, and may block access to the CNF cavity, thus preventing other nanoparticles from reaching deeper inside the CNF (Fig. 58.d-f).

5.4.2. Effect of dispersion medium

The selection of the solvent/dispersion medium critically affects the particle intercalation efficiency. Ideally, a liquid with low surface tension and low viscosity is preferred, in order to readily pre-wet the CNF inner walls and carry the well dispersed nanoparticle into the cavity. Experiments with three different liquids, namely, water, toluene and acetone were performed to select the best performing intercalating medium. 0.5 mg of dispersible magnetite nanoparticle (from EMG911) was diluted with 20ml acetone, water and toluene separately. When acetone or toluene was used as a dispersion medium, EMG-911 ferrofluid was used as the nanoparticle source. For the water based dispersion, EMG-508 Ferrofluid was used as the nanoparticle source. 0.1mg of CNFs was added into each of these dispersions and bath sonicated for 30min. Following sonication, the acetone based dispersion was left to dry at room temperature. The toluene and water dispersions were dried on a hotplate. After complete evaporation of the liquid dispersion media, a black colored dried deposit comprising magnetic nanoparticles and CNFs remained at the bottom of the drying vial. Each of these dried samples was re-dispersed in the respective solvent using 5min of bath sonication to rid the outer CNF surfaces of the attached nanoparticles. Few drops of these re-dispersed nanofiber dispersions were then dispensed on TEM grids for TEM observation. Figure 60 compares particle intercalation efficiency for the three different dispersion media. Toluene (surface tension 28.40 mN/m) is highly efficient in intercalating magnetic nanoparticles inside the CNFs. Acetone, although having the lowest surface tension among the three liquids (surface tension 25.2 mN/m), showed poor intercalation efficiency. In this case, only 1% or less of the CNFs had nanoparticles inside their cavities (see example in Fig. 60.c). Those nanoparticles, when present, occupied a very small span of the CNF length.

Intercalation from water (72 mN/m) was also very poor, with only 2-3 CNFs (see Fig. 60.b) on the entire TEM grid (hundreds of CNFs) seen to have few intercalated nanoparticle clusters inside their cavities.

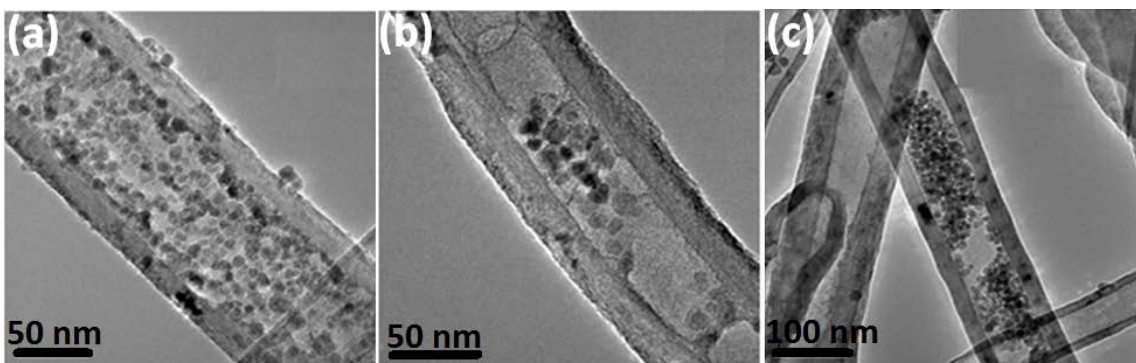


Figure 60: Magnetite nanoparticles intercalated in CNFs. The respective dispersion liquid was: (a) Toluene, (b) Water, (c) Acetone.

This outcome indicates that low surface tension of the solvent may not be the only important parameter for efficient intercalation; the solvent's molecular structure seems to play a more significant role in nanoparticle intercalation. Since toluene has a molecular structure (benzene ring) closer to the hexagonal structure of carbon/graphene layers of CNFs, the intercalation of nanoparticles suspended in toluene may be more energetically favorable compared to the other cases (acetone, water). Due to its superior performance, toluene was selected as the dispersion medium in all remaining experiments.

5.4.3. Influence of process parameters

Further experimental efforts focused on how intercalation efficiency is affected by different process parameters, such as sonication time and type, concentration of CNFs and nanoparticles in the dispersions, ratio of CNF to magnetite nanoparticles, and finally drying temperature. Intercalated CNFs were also studied in tilt mode inside the TEM to distinguish the presence of

nanoparticles inside and outside the CNFs. LHT CNFs were used for all these studies, as mentioned earlier. In addition to the LHT CNFs, HHT CNFs were also intercalated with magnetite nanoparticles by this method.

5.4.3.1. Sonication time

To evaluate the effect of sonication time, nanoparticle-CNF dispersions were either bath sonicated or probe sonicated for different time periods. Three bath sonicated samples (10min, 60min and 360min) and four probe sonicated samples (10 sec, 100 sec, 1000 sec* and 1 hour*) were prepared and evaluated via subsequent HRTEM observations.

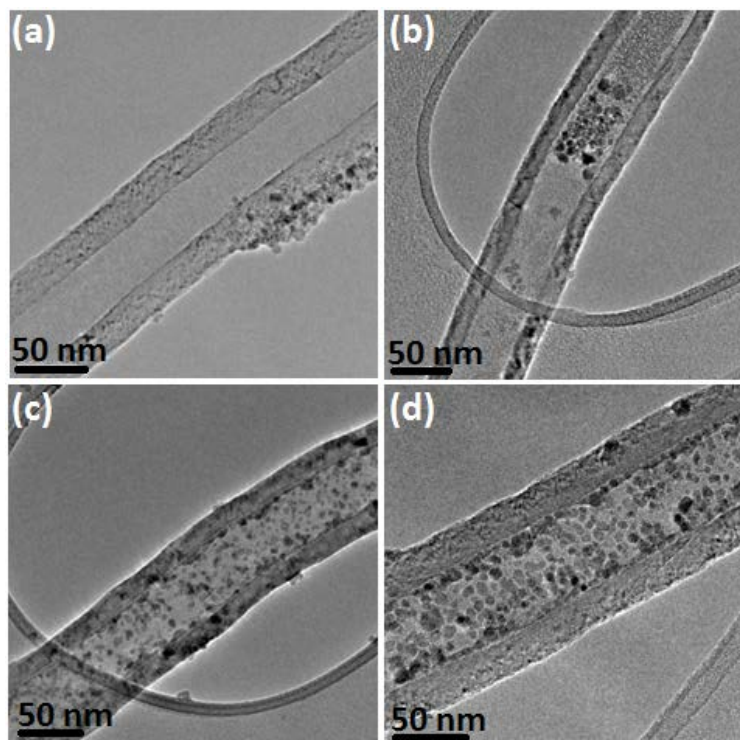


Figure 61: Typical nanoparticle-intercalated CNFs produced after (a), (b) 10 min; (c) 60 min; (d) 360 min of bath sonication. The curved edges of the supporting carbon film are visible in (b), (c) and (d).

* Probe sonication in these cases was performed for 1 min at a time, to avoid excessive heating (and likewise evaporation losses) of the liquid. After sonication, the dispersion was cooled for 1 min in room temperature water before the cycle was repeated, until the total sonication time reached the desired value.

Figure 61 shows HRTEM images of intercalated CNFs, as produced with varying periods of bath sonication. As evident from these micrographs, intercalation density was too low in the 10min bath-sonicated sample (Fig. 61.a, b). Most of the CNF cavities in this sample were vacant (Fig. 61.a), with only sporadic CNFs seen to contain small intercalated nanoparticle clusters (Fig. 61.b). A significant number of CNFs had magnetite nanoparticles attached to their outside surfaces, whereas their inside cavities were found vacant (Fig. 61.a). In the 60min bath sonicated sample, approximately 80% of the open ended tubes with internal diameter higher than 40nm were observed to contain nanoparticles inside their cavities. Almost all of these CNFs had high intercalated particle density (Figure 61.c). In the 360min bath sonicated sample, almost all open ended CNFs with sufficiently large diameter (>40 nm) were densely packed with nanoparticles; in addition, the intercalated nanoparticle number density was higher than in the 60min bath-sonicated sample (compare Figs 61.c, d). More importantly, the dense packing seen in Fig. 61.d was seen throughout the CNF length. Hence, it was concluded that prolonged bath sonication facilitates higher nanoparticle intercalation and more uniform packing along the CNF length.

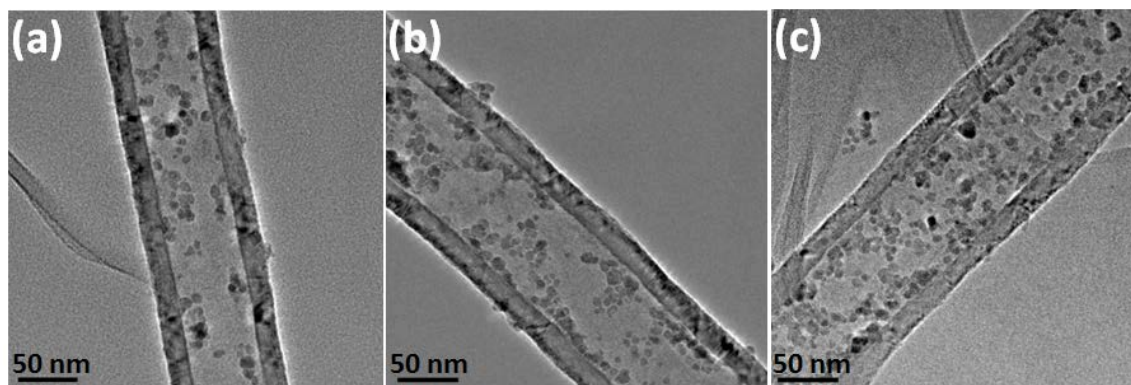


Figure 62: Nanoparticle-intercalated CNFs after: (a) 10s, (b) 100 sec; (c) 1000 sec of probe sonication.

Probe sonication was evaluated in a separate set of experiments. Here CNFs were first bath sonicated in toluene, and subsequently 1mg of dispersible magnetite nano particles (from EMG-911) were mixed in by probe sonication. Figure 62 depicts the intercalation results for probe sonication times of 10s, 100s, 1000s and one hr. With increasing probe sonication time, intercalation density increased, showing similar trend as the bath sonicated experiments. With probe sonication it was also observed that the ends of some CNFs were plugged with densely packed nanoparticles, due to which further penetration into the CNF cavity was hindered. With increased probe sonication time, this situation was observed more frequently.

Figure 63 shows a typical HRTEM image of a capped CNF after 1hr of probe sonication. Due to the very high energy density of the probe sonication process, nanoparticles were able to invade the inner cavity of tubes with comparatively smaller diameter CNFs.

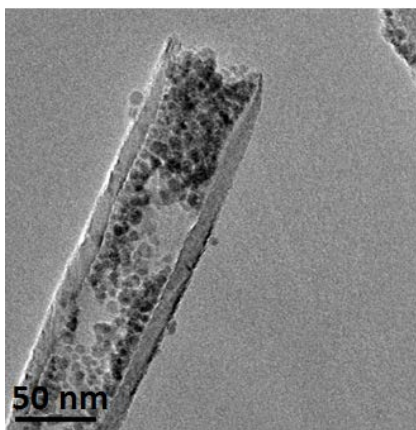


Figure 63: Nanoparticle-intercalated CNF with one end capped by clustered nanoparticles.

5.4.3.2. Sonication type

To investigate the influence of sonication type on intercalation efficiency, two additional samples were prepared. In one case, the nanoparticle-CNF dispersion was bath sonicated, while in the other, probe sonication was used. In both cases, total sonication time was 10min. To avoid

excessive heating during probe sonication, the dispersion was sonicated for one minute at a time and left to cool for one minute inside a water bath held at room temperature; this cycle was repeated ten times. Subsequently, each dispersion was dried at 120°C and the standard cleaning step and TEM sample preparation protocol were followed. Figure 64.a-c shows the morphological characteristics of nanoparticles packed inside the CNFs prepared using probe sonication. The corresponding HRTEM micrographs of intercalated CNFs which uses 10 minutes of bath sonication(in intercalation step) have been shown earlier in Figure 61.a, b.

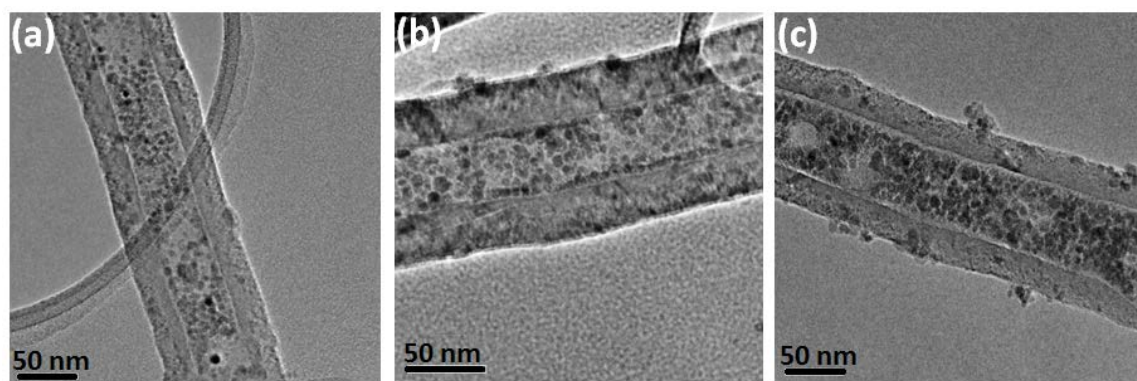


Figure 64: Intercalated CNFs from 10 min of probe sonication. The curved edge of the supporting carbon film is visible in (a).

Interestingly, probe sonication proved to be far superior to bath sonication in terms of intercalation efficiency. HRTEM observations of the probe sonicated sample showed that most of the open ended tubes were densely packed with nanoparticles. On the other hand, most CNFs from the bath sonicated samples were vacant with nanoparticles mostly observed outside the CNFs (Fig. 61.a). Very few CNFs from the bath sonicated sample revealed highly localized, small particle clusters inside their cavities (Fig. 61.b). As compared to bath sonication, probe sonication has higher energy density and it creates more rapid mixing of nanoparticles and CNFs in the suspension. This increases the probability of collisions of nanoparticles with the CNF open ends, and ultimately the particle invasion of the cavity. Further, because of the higher energy

density, the number of CNFs invaded by the liquid medium is much higher during probe sonication. The higher energy of probe sonication also helps the liquid medium to easily wet the interior of the CNFs throughout their length and indirectly helps to intercalate more nanoparticles.

5.4.3.3. Concentration of solids in dispersions

The concentration of solids is expected to significantly influence the rheological properties of the dispersions. High solids concentration increases the viscosity or may alter the effective surface tension of the dispersion. Since the intercalation process highly depends on the properties of the dispersion medium, the solids concentration also is expected to affect the intercalation process. In the present context, concentration of solids is contributed by both CNFs and magnetite nanoparticles. To investigate the influence of the combined CNF and nanoparticle concentration, two intercalation experiments were performed. In one case, 10mg of CNF and 4.16 mg of nanoparticle (from EMG 911) were mixed; in another case, 1mg of CNF and 0.416 mg of the same nanoparticles (from EMG 911) were used to prepare separate dispersions in 20ml toluene. The CNF to nanoparticle mass ratio was kept fixed (~ 2.4) in order to nullify its effect on the experimental observations (this effect is examined in the following section). Representative HRTEM images of cleaned (stripped of the particles deposited on outer walls) samples are shown in Fig. 65. Intercalated CNFs from the higher solid-concentration dispersion show intercalated nanoparticles throughout the entire CNF length with high packing density (Fig. 65.a and b). For the low solids concentration dispersion, most open ended CNFs show very densely packed nanoparticles at some locations inside their cavity; however, these densely packed nanoparticles occupy a very small fraction of their overall length (Fig. 65.c, d). This can be explained as follows. In the dispersion with lower solids content, CNF cavities were filled with toluene carrying fewer nanoparticles. After complete evaporation of the solvent outside the CNFs during drying, the toluene inside the CNF cavity also started to evaporate, thus shrinking in volume. In turn, capillary action collected the small number of nanoparticles into a shorter span of the CNF

length, eventually concentrating them to very high packing (see dense morphology in Fig. 65.c, d). In this process, the edges of the densely packed nanoparticle volume took the shape of the liquid meniscus, thus supporting the above mechanism. Furthermore, when the initial solids concentration is low, the interaction probability between the nanoparticles and CNFs during the sonication process and the drying stage is also lowered, thus contributing to lower nanoparticle packing overall. Nonetheless, most of the CNFs prepared from the low solid concentration dispersion were found to be intercalated by particles, albeit partially. During the drying process, the concentration of nanoparticles increases many-fold around the CNFs as the liquid dispersion medium evaporates. When the starting nanoparticle concentration is low, the final concentration of nanoparticles per unit drying volume is also very low. Consequently, the number of nanoparticles encapsulated per CNF is also expected to be much lower in this case as compared to the case of higher solids concentration.

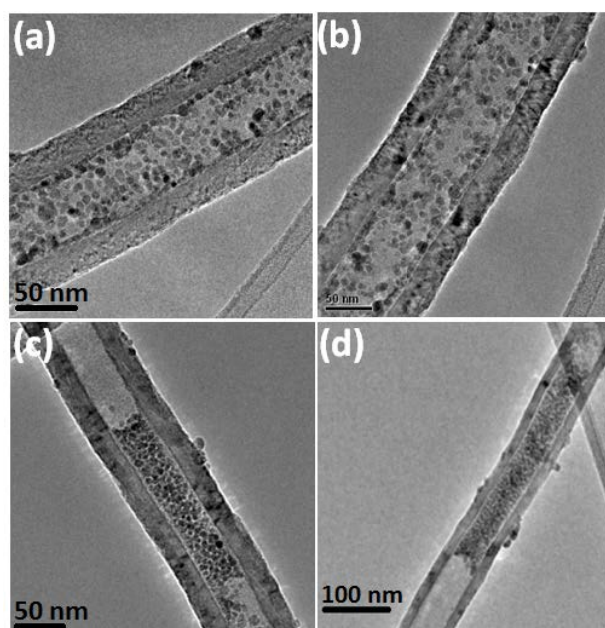


Figure 65: Intercalated CNFs obtained from experiments having: (a), (b) 10 mg CNF – 4.16 mg magnetite nanoparticle (from EMG 911) , 0.1 wt% solid concentration in 20 ml toluene ; (c),(d) 1 mg CNF-0.416 mg magnetite nanoparticle (from EMG 911), 0.01 wt% solid concentration as starting dispersion

5.4.3.4. CNF to nanoparticle mass ratio

Two samples with fixed amount of CNF (10 mg) and different amounts (1.04 mg and 4.16 mg) of magnetite nanoparticle (from EMG 911) were prepared in 20 ml toluene. Both samples were bath sonicated for 6 hrs. Subsequently, standard drying and cleaning procedures were followed. Representative HRTEM micrographs of these samples are shown in Fig. 66. As the relative amount of nanoparticles decreased, the density of intercalated nanoparticles decreased drastically (compare Fig. 66.a and b). This observation clearly shows the capability of the current method to control the number of intercalated magnetite nanoparticles inside the CNF cavity by changing the amount of Ferrofluid with respect to the CNF content. Since the response of the magnetite-intercalated CNFs under an external magnetic field is expected to be proportional to the number of nanoparticles inside the CNF cavity, tuning the number of intercalated nanoparticles inside the CNFs by this process will tune the response of the filled CNFs under a given external magnetic field.

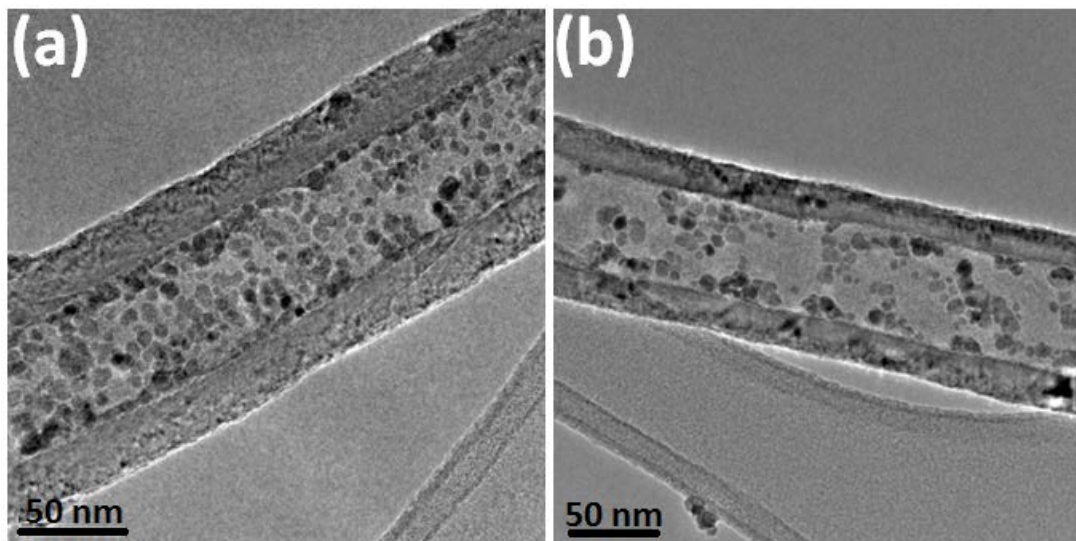


Figure 66: Intercalated CNFs obtained with Nanoparticle: CNF mass ratio of (a) 0.416:1 (b) 0.104:1 dispersion in 20 ml toluene dispersion. The curved edges of the supporting carbon film are visible in both images.

5.4.3.5. Drying temperature

The present intercalation method is utilizing two important physical mechanisms to encapsulate the nanoparticles inside the CNF cavity. The first mechanism relies upon the high energy density of bath and probe sonication. The second mechanism aiding the intercalation process is the known^[230,231] concentration gradient driven flow accomplished by evaporating the liquid dispersion medium either by heating (e.g. hotplate) or naturally at room temperature. Hence the drying temperature is a crucial parameter in this intercalation process and is expected to have significant influence on this mechanism. Important temperature-dependent properties which may influence the intercalation process are the diffusion coefficient of nanoparticles, fluid properties, dispersion properties and evaporation rate of liquid dispersion medium. All prior experiments used 120°C (drying temperature) for evaporation of the liquid dispersion medium (i.e. toluene or water). One additional experiment was carried out where the dispersions were dried at room temperature in a chemical hood. As done in prior standard experiments, 10 mg of CNF and 4.16 mg of nanoparticle (from EMG 911) were bath sonicated in 20 ml of toluene for 6 hrs. Representative images of the filled CNF samples are compared in Fig. 67. Figure 67.a shows a representative CNF from the room-temperature dried sample and reveals a smaller number of intercalated nanoparticles as compared to the sample dried at 120°C (Fig. 67.b).

The higher intercalated nanoparticle packing in the sample dried at 120°C can be explained by the higher particle diffusion coefficient at that higher temperature. The diffusion coefficient D of nanoparticles in the dispersion is given by Stokes-Einstein's equation,^[39]

$$D = \frac{kT}{6\pi\eta R_c} \dots\dots\dots(31)$$

where R_c is the nanoparticle radius; k Boltzmann's constant; T the temperature and η the viscosity of the liquid. Apart from the proportional relationship between D and T , higher temperature also decreases the liquid viscosity, further raising diffusive agility, in turn,

facilitating the intercalation process. In the room-temperature dried sample, significant amounts of polymeric deposits were observed inside the CNF cavity. Polymeric deposits sometimes form peapod^[230,231] like morphologies, as reported elsewhere. In addition to nanoparticles and CNFs, surfactant molecules (fatty acid surfactant) were also present in the dispersion. These surfactants also invade the CNFs during the drying/ intercalation process and form deposit patterns similar to those seen in Fig. 67.a.

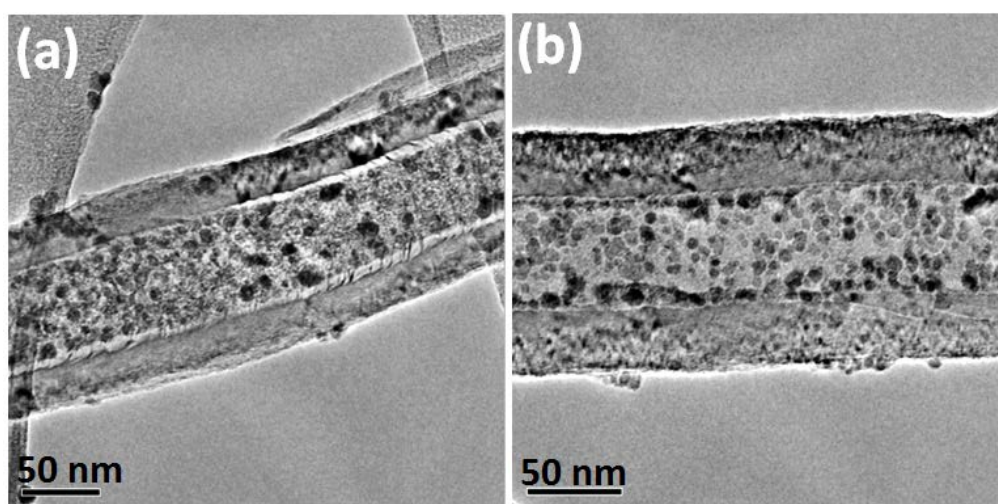


Figure 67: Intercalated CNFs obtained from drying at: (a) room temperature; (b) 120°C. Note the denser packing in (b), as compared to (a).

Careful inspection of Fig. 67.a also reveals that multiple graphene layers peel off from the CNF wall and bend towards the polymeric deposit at the core of the CNF cavity. This peeling may be due to the capillary tension of the dispersion medium, which upon drying, forces the inner graphene layers of the CNF wall to separate out and bend towards the surfactant deposits. Figure 68 shows a magnified detail from another CNF observed on the same TEM grid.

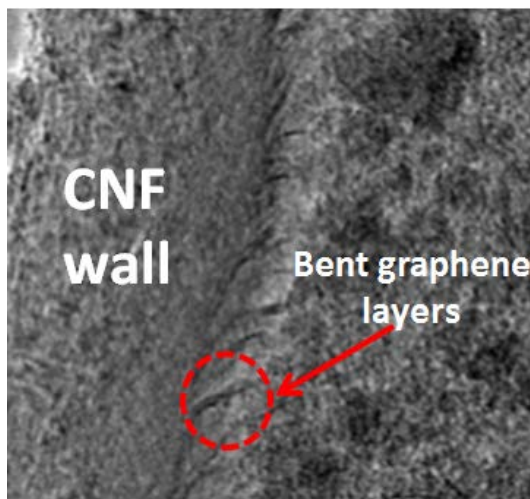


Figure 68: Magnified detail of HRTEM image showing bending of graphene sheets from CNF wall (left) toward the surfactant nanoparticle mixture at the core of CNF (right).

The protruding bent layers of graphene sheets were not observed in the sample dried at 120°C. Polymeric surfactant deposits in this case were probably completely destroyed because of the higher drying temperature. It is worth noting that similar observations have been made^[232] in the interior of hydrothermally-synthesized closed-end carbon nanofibers which contained an aqueous phase. The capillary action of the enclosed water phase was reported therein to be responsible for the peeling of the graphene layers towards the encased fluid.

5.4.3.6. Sonication before drying

To evaluate the effect of sonication on concentration gradient driven filling, two intercalation experiments were carried out. In one case, the 10 mg of CNF was bath sonicated for 10min in 20 ml toluene. Subsequently, 4.16 mg of nanoparticle (from EMG-911) were added into the CNF dispersion and bath sonicated for 6 hrs. In another case, the same amount of magnetite (from EMG-911) was added into the CNF dispersion after 6 hrs of bath sonication. In the latter case, there was no sonication of the combined CNF plus nanoparticle mixture. HRTEM observation of these samples confirmed the importance of simultaneous sonication of CNFs and nanoparticles for effective intercalation. When sonication of nanoparticles and CNFs was performed, higher

degree of intercalation was observed as already shown in Fig. 66.b. In the case where sonication was performed up to the addition of the nanoparticles, very few CNFs were seen to contain intercalated nanoparticles (Fig. 69). Moreover, even in the rare CNFs seen to encase nanoparticles, the number of nanoparticles was very small.

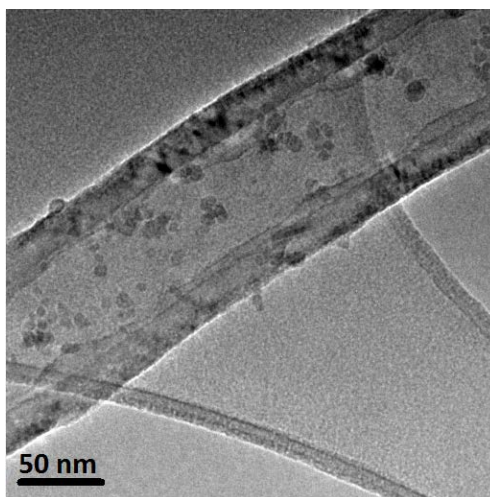


Figure 69: HRTEM image of intercalated CNF obtained from experiment where the Ferrofluid nanoparticles were added after sonication of the Ferrofluid. The curved edges of the supporting carbon film can be also seen.

There exists a variation in intercalation density among the different CNFs in this sample. Some CNFs were found to have very few intercalated nanoparticles, whereas most CNFs were completely vacant. This difference can only be explained by emphasizing the importance of simultaneous sonication of nanoparticles and CNFs. The probability of intercalation of a nanoparticle inside any CNF cavity increases with increasing CNF-nanoparticle collision probability. The number of collisions N per unit volume between nanoparticles and the open ends of the carbon nanofibers is estimated by the following equation,^[39]

$$N = \alpha 4\pi D R_c n_1 n_2 \left[t + \frac{2R_c \sqrt{t}}{\sqrt{\pi D}} \right] \dots \dots \dots (32)$$

where D is the Diffusion coefficient of nanoparticles from Eq. (1); n_1 is the concentration of nanoparticles in the liquid; n_2 the concentration of CNFs in the liquid; t the time from the onset of the experiment; and $\alpha = 1/3$ (expression factor). Under simultaneous sonication of CNFs and nanoparticles, the interaction probability is expected to be orders of magnitude higher compared to the simple diffusive case. In other words, the effective value of D for sonication-assisted mixing will be much higher than the simple diffusion case. Moreover, prolonged bath sonication ensures uniform distribution of surfactant (a Ferrofluid ingredient) and nanoparticles both inside and outside the CNF cavity. Prolonged sonication also helps the CNFs to mix well with the surfactant molecules, causing the CNFs to be well dispersed. Well dispersed CNFs ensure higher probability of nanoparticle-CNF interaction during the drying process. Because of the above mentioned reasons, simultaneous sonication of CNF and nanoparticle yields higher intercalation efficiency and is thus preferable.

5.5. Tilt mode TEM observation of LHT CNFs

To confirm the presence of nanoparticles inside the CNF cavity, selected samples were observed at different tilt angles inside the TEM. Figure 70 shows HRTEM images obtained from one such experiment at 3 different tilt angles with respect to the longitudinal axis of the CNF. As is evident from the figure, nanoparticles constrained by the CNF wall always remain within the space bounded by the walls, irrespective of the rotation angle of the tilt stage. Such observations assisted in resolving definitely whether particles were within the CNF cavity or were attached to the CNF wall exterior.

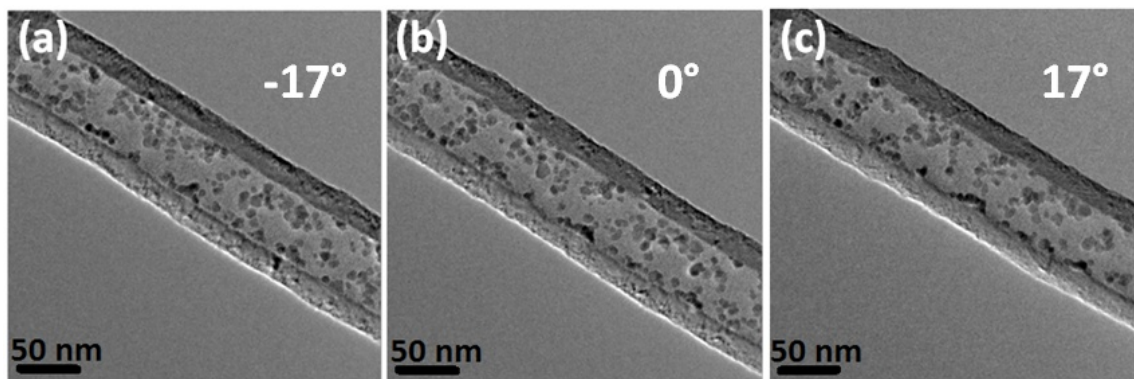


Figure 70: Tilt specimen HRTEM images of intercalated CNFs rotated at: (a) -17° ; (b) 0° , (c) 17° around the CNF axis. Such imaging helps in determining whether particles are encased within the CNF cavity or are attached to the exterior walls.

5.6. Intercalation of HHT CNFs

Unlike the LHT CNFs, HHT CNFs have completely different morphology, as described earlier (Fig. 57). Due to their smaller inner diameter and highly corrugated internal wall structure, intercalation of nanoparticles in HHT CNFs is more challenging. Both probe sonication and bath sonication were used separately to intercalate nanoparticles inside HHT CNFs. One sample was prepared with 240 min bath sonication, while another with 60 minutes of probe sonication. For the latter case, one minute of probe sonication was followed by one minute of cooling in a room temperature water bath at a time; this cycle was repeated sixty times. Subsequently, both dispersions were dried and cleaned to remove nanoparticle deposits from the CNF wall exterior. HRTEM observation of the probe-sonicated CNF sample showed that most HHT CNFs with diameter above 40 nm contained nanoparticles (Fig. 71.a and b). Moreover, nanoparticles were densely packed inside the CNF cavities. On the other hand, the number of intercalated HHT CNFs in the bath-sonicated sample was far lower than in the probe-sonicated sample. For the bath-sonicated sample with similar time scale of ultrasonication time, only CNFs with very large inner diameter (greater than ~ 70 nm) were seen to have nanoparticles inside (Fig. 70.c, d). Thus, compared to the LHT tubes, intercalation in HHT tubes is clearly inferior. One possible approach to improve the intercalation of HHT CNFs may be the use of smaller nanoparticles, as most of the

HHT CNFs have smaller internal diameters, thus making it difficult for the larger nanoparticles to penetrate into the hollow CNF cavity.

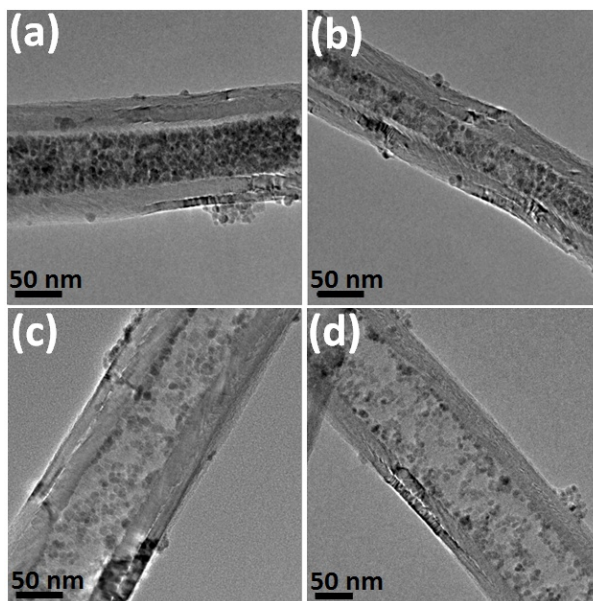


Figure 71: HRTEM images of intercalated CNFs from (a), (b) 60 min of probe sonication; (c), (d) 240 min of bath sonication.

5.7. Response of intercalated CNFs under an external magnetic field

To show the response of intercalated CNFs under an external magnetic field, a dilute (1mg in 20 ml toluene) dispersion of LHT CNFs was prepared. Intercalation was performed with 360min of bath sonication, as described earlier. A strong magnet (0.1 Tesla field strength) was placed close to the glass vial containing the dispersion (Fig. 72.a).

As expected, the magnet caused the magnetic CNFs to separate from the dispersion medium; as seen in Fig. 72.b, the magnetized CNFs accumulated on the glass vial wall by the magnet. As the intercalated magnetite nanoparticles are single crystal/single domain superparamagnetic in nature, the presence of any external magnetic field generates magnetic moment in them, thus causing

them to align towards the magnet. Since the intercalated CNFs are free to move within the liquid medium and the magnetite nanoparticles remain trapped in the CNF cavity, CNFs move towards the direction of the externally applied magnet field. The amount of force generated on each CNF is proportional to the strength of the external magnetic field and the total number of nanoparticles inside the CNF. This magnetic force must first overcome the liquid viscous drag and diffusive forces, in order to move the CNF towards the magnet. Figure 72.a and b show that the intercalation process reported herein is efficient enough to impart enough magnetic property to the CNFs so that they be pulled by a 0.1 T magnet.

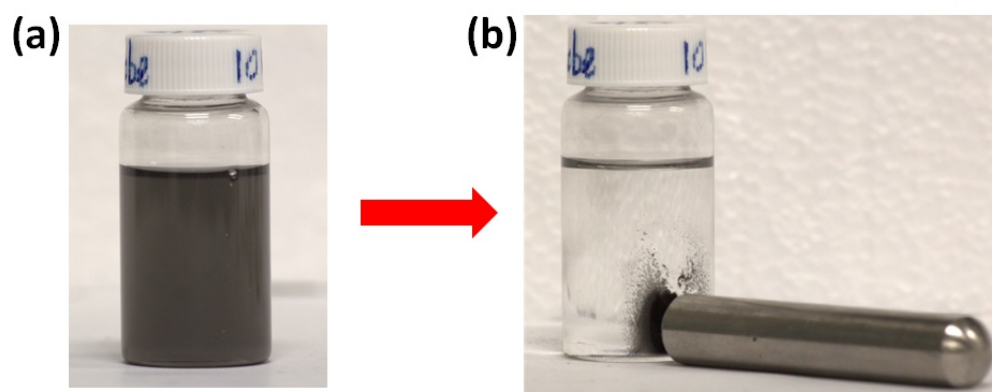


Figure 72: (a) Well dispersed magnetized CNFs in toluene; (b) Separation of magnetized CNFs from toluene in the presence of a bar magnet (0.1 T).

5.8. Application: Alignment of magnetic CNFs to fabricate polymeric coatings of anisotropic properties.

Magnetic nanoparticle loaded LHT CNFs prepared via 360 minutes of bath sonication process were successfully used to fabricate polymer nanocomposites with high anisotropic properties. Magnetic nanofibers were introduced in a solution of PMMA in different weight concentration and dry casted on a silicon substrate under a magnetic field of 0.13 Tesla. Figure 73 shows an

optical image of oriented nanofibers in composite film. To estimate the anisotropic electrical property of the composites, PMMA composites with 1wt% magnetic CNFs loading were prepared both under a magnetic field and without it. Measurement in composites with aligned CNFs shows (Fig. 74) high electrical current when voltage was applied along the direction of fiber alignment. No current was detected (Fig.74.) when the applied voltage was perpendicular to the direction of fiber alignment, indicating very high degree of electrical anisotropy in these composites. Similar measurement in control composites with randomly oriented CNFs showed no significant variation in electrical current, hence no electrical anisotropy. Similar anisotropy is also expected in magnetic as well as mechanical properties of these composites.

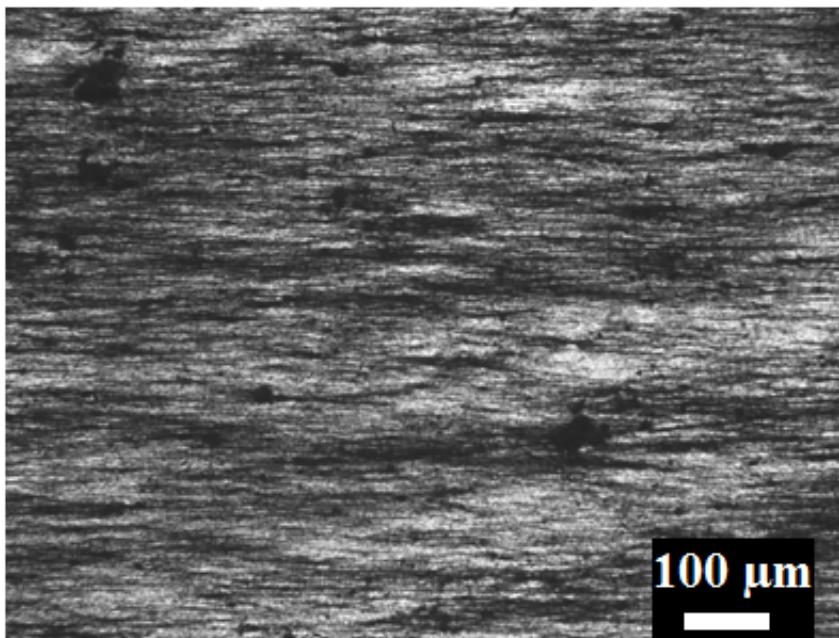


Figure 73: Oriented magnetic nanofibers in PMMA nanocomposite with 1 wt% nanofiber loading, prepared by solution casting process under 0.13 Tesla magnetic field. Alignment experiments were performed by collaborators at the Italian Institute of Technology, Italy.

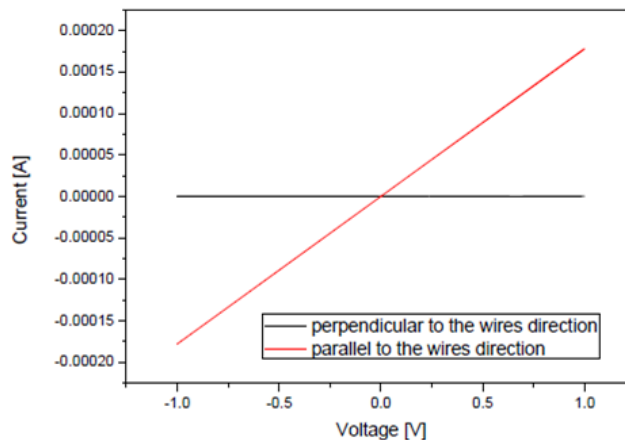


Figure 74: I-V measurement in 1 wt% magnetic-CNF nanocomposite with aligned nanofibers under an external magnetic field. Measurements were performed by collaborators at the Italian Institute of Technology, Italy.

5.9. Conclusion

We have demonstrated a nonchemical low cost process to create magnetically active CNFs. This is achieved via incorporation of superparamagnetic single crystal magnetite nanoparticles inside their hollow cavities by ultrasonication assisted and concentration gradient driven filling mechanism. Influence of important process parameters on intercalation process are analyzed with detailed HRTEM observations. Tuning the process parameters, different types of nanoparticles morphologies and different nanoparticles densities were obtained which may tune the magnetic response of the CNFs under externally applied magnetic field. Because of high electrical and thermal conductivities of these magnetically active CNFs, promising smart materials such as magnetically tunable nanofluids, polymer composites with anisotropic thermal, electrical and mechanical properties can be synthesized. Such materials can find applications in sensors, optoelectronic devices, energy and heat transfer devices. These nanoscale composites also open up a possibility of a new class of not only magnetically active materials, but also of nanoscale multifunctional composites. As future work, nanoparticles having properties other than magnetic could be intercalated into the CNFs to synthesize new classes of nanohybrid materials with other functionalities and applications. This process also creates a new platform to study the various properties and interaction of nanoparticles inside nanoenclosures (eg. CNFs).

CITED LITERATURE

1. C.P.Poole, J, Owens, F. J.: Introduction to Nanotechnology. Hoboken, NJ, Wiley-Interscience, 2003.
2. Walter, P., Welcomme, E., Hallégot, P., Zaluzec, N. J., Deeb, C., Castaing, J., Veysière, P., Bréniaux, R., Lévêque, J.L., and Tsoucaris, G.: Early use of PbS nanotechnology for an ancient hair dyeing formula. *Nano Lett.*, 6: 2215-2219, 2006.
3. Freestone, I., Meeks, N., Sax, M., and Higgitt. C.: The Lycurgus Cup –A Roman Nanotechnology. *Gold Bulletin*, 40: 204-277, 2007.
4. Reibold, M., Paufler, P., Levin, A. A., Kochmann, W., Pätzke N., and Meyer, D. C.: Materials: Carbon nanotubes in an ancient Damascus sabre. *Nature*, 444: 286, 2006.
5. Binnig, G., and Rohrer, H.: Scanning tunneling microscopy. *IBM Journal of Research and Development*, 30: 355-369, 1986.
6. Kroto, H. W., Heath, J. R., O'Brien, S. C., Curl, R. F., and Smalley, R. E.: C60:Buckminsterfullerene. *Nature*, 318:162–163, 1985.
7. Feynman R.: There is plenty of room at the bottom. *Caltech Engineering and Science*, 23: 22-365, 1960.
8. Capek, I.: Nanocomposite Structures and Dispersions Science and Nanotechnology-Fundamental Principles and colloidal Particles. New York, Elsevier, 2006.
9. Manz, A., Becker, H. (eds): Microsystem Technology in Chemistry and Life Sciences, Topics in Current Chemistry 194, Berlin, Heidelberg , Springer, 1998.
10. Beebe, D. J., Mensing, G. A., and Walker G.M.: Physics and applications of microfluidics in biology. *Annu. Rev. Biomed. Eng.*, 4:261–286, 2002.
11. Xia, Y., and Whitesides G.M.: Soft lithography. *Angew. Chem. Int. Ed.*, 37: 550–575, 1998.
12. Becker, H., and Gaertner, C.: Polymer microfabrication methods for microfluidic analytical applications. *Electrophoresis*, 21: 12–26, 2000.
13. Xia, Y., Kim, E., Zhao, X.M., Rogers, J. A., Prentiss, M., Whitesides, G. M.: Complex optical surfaces formed by replica molding against elastomeric masters. *Science*, 273:347–349, 1996.
14. Chou, S.Y., Krauss, P.R., and Renstrom, P.J.: Imprint lithography with 25-nanometer resolution. *Science*, 272: 85–87, 1996.
15. Kumar, A., and Whitesides, G.M.: Features of gold having micrometer to centimeter dimensions can be formed through a combination of stamping with an elastomeric stamp and an alkanethiol ink followed by chemical etching. *Appl. Phys. Lett.*, 63: 2002–2004, 1993.

CITED LITERATURE (continued)

16. Drexler, K.E.: *Nanosystems: Molecular Machinery, Manufacturing and Computation*. New York, Wiley, 1992.
17. Timp, G. (ed.): *Nanotechnology*. New York, Springer, 1999.
18. Rietman, E. A.: *Molecular Engineering of Nanosystems*. New York, Springer, 2001.
19. Goddard, W. A., Brenner, D. W., Lyshevski, S. E., and Iafrate, G. J. (eds): *Handbook of Nanoscience, Engineering, and Technology*. Boca Raton, CRC Press, 2002.
20. Nalwa, H. S. (ed.): *Nanostructured Materials and Nanotechnology*. San Diego, Academic Press, 2002.
21. Bhushan, B.: *Handbook of Micro/Nanotribology*, 2nd edn. Boca Raton, CRC Press, 1999.
22. Kamigaito, O.: What can be improved by nanometer composites? *J. Jpn. Soc. Powder Powder Metall.*, 38:315-21, 1991 in Kelly, A, Concise encyclopedia of composites materials. Elsevier Science Ltd, 1994.
23. Sandler, J.K.W., Kirk, J.E., Kinloch, I.A., Shaffer, M.S.P., and Windle, A.H.: Ultra-low electrical percolation threshold in carbon-nanotube-epoxy composites. *Polymer*, 44: 5893-5899, 2003.
24. Ramasubramaniam, R., Chen, J., and Liu, H.Y.: Homogeneous carbon nanotube/polymer composites for electrical applications. *Appl. Phys. Lett.*, 83: 2928-2930, 2003.
25. Usuki, A., Kawasumi, M., Kojima, Y., Okada, A., Kurauchi, T., Kamigaito, O.: Swelling behavior of montmorillonite cation exchanged for omega amino acids by epsilon-caprolactam. *J. Mater. Res.*, 8: 1174-1178, 1993.
26. Ding, Y.Y., Hu, Y., Gui, Z., and Song, L.: Preparation of poly (methyl methacrylate)/lanthanum hydroxide nanowire nanocomposites with improvement in thermal stability. *Mat. Lett.*, 62: 4290-4292, 2008.
27. Tiwari, M. K., Bayer, I. S., Jursich, G. M., Schutzius, T. M., and Megaridis C. M.: Highly liquid-repellent, large-area, nanostructured poly (vinylidene fluoride)/ poly (ethyl 2-cyanoacrylate) composite coatings: Particle filler effects. *ACS App. Mat. & Interphase*, 2: 1114-1119, 2010.
28. Cao, L., Jones, A. K., Sikka, V. K., Wu, J., and Gao, D.: Anti-icing superhydrophobic coatings. *Langmuir*, 25: 12444-12448, 2009.
29. Mishchenko, L., Hatton, B., Bahadur, V., Taylor, J. A., Krupenkin T., and Aizenberg, J.: Design of ice-free nanostructured surfaces based on repulsion of impacting water droplets. *ACS Nano*, 4: 7699-7707, 2010.
30. Betz, A. R., Xu, J., Qiu, H., and Attinger, D.: Do surfaces with mixed hydrophilic and

CITED LITERATURE (continued)

- hydrophobic areas enhance pool boiling? *Appl. Phys. Lett.*, 97: 141909, 2010.
31. Garrod, R. P., Harris, L. G., Schofield, W. C. E., McGettrick, J., Ward, L. J., Teare, D. O. H., and Badyal, J. P. S.: Mimicking a Stenocara beetle's back for microcondensation using plasmachemical patterned superhydrophobic-superhydrophilic surfaces. *Langmuir*, 23: 689-693, 2007.
 32. Zhai, L., Berg, M. C., Cebeci, F. Ç., Kim, Y., Milwid, J. M., Rubner, M. F., and Cohen, R. E.: Patterned superhydrophobic surfaces: Toward a synthetic mimic of the Namib Desert beetle. *Nano Lett.*, 6: 1213-1217, 2006.
 33. Tuteja, A., Choi, W., McKinley, G. H., Cohen, R. E., and Rubner, M. F.: Design parameters for superhydrophobicity and superoleophobicity. *MRS Bulletin*, 33:752-758, 2008.
 34. Al-Saleh, M. H., and Sundararaj, U.: A review of vapor grown carbon nanofiber/polymer conductive composites. *Carbon*, 47: 2-22, 2009.
 35. Geetha, S., Kumar, K.K.S., Rao, C.R.K., Vijayan, M., Trivedi, D.C.: EMI shielding: Methods and materials—A Review. *J. Appl. Polym. Sci.*, 112:2073- 2086, 2009.
 36. Gautam, U.K., Costa, P. M .F. J., Bando, Y., Fang, X., Li, L., Imura, M., and Golberg, D.: Recent developments in inorganically filled carbon nanotubes:successes and challenges. *Sci. Technol. Adv. Mater.*, 11:054501, 2010.
 37. Smith, B.W., Monthieux, M., and Luzzi, D.E.: Encapsulated C60 in carbon nanotubes *Nature*, 396: 323-324, 1998.
 38. Das, M., Dhand, C., Sumana, G., Srivastava, A. K., Nagarajan, R., and Malhotra, B. D.: Electrophoretically fabricated core-shell CNT-DNA biowires for biosensing. *J. Mater. Chem.*, 22: 2727-2732, 2012.
 39. Chamberlain, T. W., Popov, A. M., Knizhnik, A. A., Samoilov, G. E., and Khlobystov, A. N.: The role of molecular clusters in the filling of carbon nanotubes. *ACS Nano*, 4: 5203-5210, 2010.
 40. Torre, A. L., Fay, M. W., Rance, G.A., Lopez, M.C.G., Solomonsz, W.A., Brown, P. D., and Khlobystov, A. N.: Interactions of gold nanoparticles with the interior of hollow graphitized carbon nanofibers. *Small*, 8:1222-1228, 2012.
 41. de Gennes, P.G., Brochard-Wyart, F., and Quere, D.: Capillarity and Wetting Phenomena-Drops, bubbles, Pearls, Waves. New York, Springer-Verlag, Inc., 2004.
 42. Yan, Y.Y., Gao, N., and Barthlott W.: Mimicking natural superhydrophobic surfaces and grasping the wetting process: A review on recent progress in preparing superhydrophobic surfaces. *Adv. Colloid Interface Sci.*, 169:80–105, 2011.

CITED LITERATURE (continued)

43. Bhushan, B., and Jung, Y. C.: Natural and biomimetic artificial surfaces for superhydrophobicity, self-cleaning, low adhesion, and drag reduction. *Prog. Mater Sci.*, 56:1–108, 2011.
44. Barthlott W, and Neinhuis C.: Purity of the sacred lotus, or escape from contamination in biological surfaces. *Planta*, 202:1–8, 1997.
45. Li, X.M., Reinhoudt, D., and Crego-Calama, M.: What do we need for a superhydrophobic surface? A review on the recent progress in the preparation of superhydrophobic surfaces. *Chem. Soc. Rev.*, 36: 1529–1530, 2007.
46. Roach, P., Shirtcliffe, N. J., and Newton, M, I.: Progress in superhydrophobic surface development. *Soft Matter*, 4: 224–240, 2008.
47. Gao, L., and McCarthy, T. J.: How Wenzel and Cassie were wrong. *Langmuir*, 23: 3762-3765, 2007.
48. Nosonovsky, M.: On the range of applicability of the Wenzel and Cassie equations. *Langmuir*, 23: 9919-9920, 2007.
49. Abraham, F. F.: Homogeneous nucleation theory. New York, Academic Press, 1974.
50. Ham, F. S.: Diffusion-limited growth of precipitate particles. *J. Appl. Phys.*, 30:1518-1525, 1959.
51. Götz, G., Mészáros, E., and Vali, G.: Atmospheric Particles and Nuclei. Budapest, Akadémiai Kiadó, 1991.
52. Young, K. C.: Microphysical Processes in Clouds. New York, Oxford Univ. Press, 1993.
53. Pruppacher, H. R. and Klett, J. D.: Microphysics of Clouds and Precipitation - Second Edition. Dordrecht, Boston, London, Kluwer Academic Publ., 1997.
54. Jeffery, C. A. and Austin, P. H.: Homogeneous nucleation of supercooled water: Results from a new equation of state. *J. Geophys. Res. Atmosph.*, 102: 25269-25279, 1997.
55. Volmer, M., Weber, A.: Keimbildung in übersättigten Gebilden (Nucleation of supersaturated structures). *Z. Physik. Chem.*, 119:277-301, 1926.
56. Fokin, V. M., Yuritsyn, N. S., and Zanotto, E. D.: Nucleation and Crystallization Kinetics in Silicate Glasses: Theory and Experiment. In: Nucleation Theory and Applications, Eds. Schmelzer, J.W.P., pp 74-125. Alemanha, Wiley -VCH Verlag GmbH & Co., 2005.
57. Varanasi, K. K., Deng, T., Smith, J. D., Hsu, M., and Bhate, N.: Frost formation and ice adhesion on superhydrophobic surfaces. *Appl. Phys. Lett.*, 97: 234102, 2010.

CITED LITERATURE (continued)

58. Sarkar, D. K., and Farzaneh, M.: Superhydrophobic coatings with reduced ice adhesion. *J. Adhes. Sci. Technol.*, 23: 1215–1237, 2009.
59. Bahadur, V., Mishchenko, L., Hatton, B., Taylor, J. A., Aizenberg, J., and Krupenkin, T.: Predictive model for ice formation on superhydrophobic surfaces. *Langmuir*, 27: 14143–14150, 2011.
60. Kulinich, S. A., and Farzaneh, M.: How wetting hysteresis influences ice adhesion strength on superhydrophobic surfaces. *Langmuir*, 25: 8854–8856, 2009.
61. Antonini, C., Innocenti, M., Horn, T., Marengo, M., and Amirfazli, A.: Understanding the effect of superhydrophobic coatings on energy reduction in anti-icing systems. *Cold Reg. Sci. Technol.*, 67: 58–67, 2011.
62. Chung, D.D.L.: Electromagnetic interference shielding effectiveness of carbon materials. *Carbon*, 39: 279–285, 2001.
63. Chung, D.D.L.: Materials for electromagnetic interference shielding. *J. Mater. Eng. Perform.*, 9:350–354, 2000.
64. Belevitch, V.: Summary of the history of circuit theory, *Proceed. IRE.*, 50: 848–855, 1962.
65. Vandewalle, J.: In memoriam – Vitold Belevitch, *Intl. J. Circ. Theo. and Appl.*, 28: 429–430, 2000.
66. Valkenburg, M.E. Van. : Circuit Theory: Foundations and Classical Contributions, pp.334, Stroudsburg, Pennsylvania, Dowden, Hutchinson & Ross, 1974.
67. Dicke, R. H.: A computational method applicable to microwave networks. *J. Appl. Phys.*, 18: 873-878, 1947.
68. Hong, Y.K., Lee, C.Y., Jeong, C.K., Sim, J.H., Kim, K., Joo, J., Kim, M.S., Lee, J.Y., Jeong, S.H., and Byun S.W.: Electromagnetic interference shielding characteristics of fabric complexes coated with conductive polypyrrole and thermally evaporated Ag. *Curr. Appl. Phys.*, 1: 439–442, 2001.
69. S parameter design: Application Note 154, Hewlett Packard, 1972.
70. Xia, F., and Jiang, L.: Bio-inspired, smart, multiscale interfacial materials. *Adv. Mater.*, 20: 2842–2858, 2008.
71. Zhang, Y., Chen, Y., Shi, L., Li, J., and Guo, Z.: Recent progress of double-structural and functional materials with special wettability. *J. Mater. Chem.*, 22: 799-815, 2012.
72. Liu, K., Jiang, L.: Bio-inspired self-cleaning surfaces. *Annu. Rev. Mater. Res.*, 42:231–263, 2012.

CITED LITERATURE (continued)

73. Liu, K., Jiang, L.: Bio-inspired design of multiscale structures for function integration. *Nano Today*, 6: 155-175, 2011.
74. Bhushan, B.: Biomimetics: lessons from nature-an overview. *Phil. Trans. R. Soc. A.*, 367: 1445-1486, 2009.
75. Koch, K., and Barthlott, W.: Superhydrophobic and superhydrophilic plant surfaces: an inspiration for biomimetic materials. *Phil. Trans. R. Soc. A*, 367:1487–1509, 2009.
76. Zheng, Y., Gao, X., and Jiang, L.: Directional adhesion of superhydrophobic butterfly wings. *Soft Matter*, 3: 178- 182, 2007.
77. Gao, X.F., and Jiang, L.: Biophysics: water repellent legs of water striders. *Nature*, 432:36, 2004.
78. Feng, X.Q., Gao, X., Wu, Z., Jiang, L., and Zheng Q.S.: Superior water repellency of water strider legs with hierarchical structures: experiments and analysis. *Langmuir*, 23: 4892-4896, 2007.
79. Liu, K., Zhang, M., Zhai, J., Wang, J., and Jiang, L.: Bioinspired construction of Mg–Li alloys surfaces with stable superhydrophobicity and improved corrosion resistance. *Appl. Phys. Lett.*, 92: 183103, 2008.
80. Liu, M.J., Wang, S.T, Wei, Z.X., Song, Y.L., and Jiang, L.: Bioinspired design of a superoleophobic and low adhesive water/solid interface. *Adv. Mater.*, 21:665–669, 2009.
81. Parker, A. R., and Lawrence, C. R.: Water capture by a desert beetle. *Nature*, 414: 33-34, 2001.
82. Xue, C. H., Jia, S.T., Zhang, J., and Ma, J. Z.: Large-area fabrication of superhydrophobic surfaces for practical applications: an overview. *Sci. Technol. Adv. Mater.*, 11: 033002, 2010.
83. Liu, K., Tian , Y., and Jiang, L.: Bio-inspired superoleophobic and smart materials: design, fabrication, and application. *Prog. Mater Sci.*, 58: 503–564, 2013.
84. Pan, S., Kota, A. K., Mabry, J. M., and Tuteja, A.: Superomniphobic surfaces for effective chemical shielding. *J. Am. Chem. Soc.*, 135: 578–581, 2013.
85. Bayer, I. S., Tiwari, M. K., and Megaridis, C. M.: Biocompatible poly (vinylidene fluoride) /cyanoacrylate composite coatings with tunable hydrophobicity and bonding strength. *Appl. Phys. Lett.*, 93: 173902, 2008.
86. Hwang, H.S., Kim, N.H., Lee, S.G., Lee, D.Y., Cho, K., and Park, I.: Facile fabrication of transparent superhydrophobic surfaces by spray deposition. *ACS Appl. Mater. Interfaces*, 3:2179–2183, 2011.

CITED LITERATURE (continued)

87. Han, J.T., Kim, S.Y., Woo, J.S., and Lee, G.W.: Transparent, conductive, and superhydrophobic films from stabilized carbon nanotube/silane sol mixture solution. *Adv. Mater.*, 20:3724–3727, 2008.
88. Cober, S. G., Isaac, G. A., and Strapp, J. W.: Characterizations of aircraft icing environments that include supercooled large drops. *J. Appl. Meteor.*, 40: 1984-2002, 2001.
89. Lasher-Trapp, S., Anderson-Bereznicki, S., Shackelford, A., Twohy, C. H., and Hudson, J. G.: An investigation of the influence of droplet number concentration and giant aerosol particles upon supercooled large drop formation in wintertime stratiform clouds. *J. Appl. Meteorol. Clim.*, 47: 2659–2678, 2008.
90. Gent, R. W., Dart, N. P., Cansdale, J. T.: Aircraft icing. *Philos. Trans R. Soc., A.*, 358: 2873–2911, 2000.
91. FAA-H-8083-15A, Instrument Flying Handbook, Chapter 10, http://www.faa.gov/library/manuals/aviation/instrument_flying_handbook.
92. FAA Regulation 25 Appendix C, FAR 25-C, Federal Aviation Administration, 1999.
93. Liu, Z., Gou, Y., and Wang, J.: Frost formation on a super-hydrophobic surface under natural convection conditions. *Int. J. Heat Mass Trans.*, 51: 5975-5982, 2008.
94. Tourkine, P., Merrer, M. L., and Quéré, D.: Delayed freezing on water repellent materials. *Langmuir*, 25: 7214-7216, 2009.
95. Poots, G.I.: Ice and snow accretion on structures. Res. Stud. Press, 1996.
96. Anderson, D.N., and Reich, A.D.: Test of the Performance of coatings for low Ice adhesion. NASA Tech. Memorandum 107399, also paper AIAA-97-0303, 1997.
97. Jung, S., Dorrestijn, M., Raps, D., Das, A., Megaridis, C.M., and Poulikakos, D.: Are superhydrophobic surfaces best for icephobicity? *Langmuir*, 27: 3059–3066, 2011.
98. Yao, X., Song, Y., Jiang, L. Applications of bio-inspired special wettable surfaces. *Adv. Mater.*, 23:719-734, 2011.
99. Meuler, A.J., McKinley, G.H., and Cohen, R.E.: Exploiting topographical texture to impart icephobicity. *ACS Nano*, 4:7048–7052, 2010.
100. Kulinich, S. A., Farhadi, S., Nose, K., and Du, X. W.: Superhydrophobic surfaces: are they really ice-repellent? *Langmuir*, 27:25–29, 2011.
101. Kim, P., Wong, Tak-Sing., Alvarenga, J., Kreder, M. J., Adorno-Martinez, W. E., Aizenberg, J.: Liquid-infused nanostructured surfaces with extreme anti-ice and anti-frost performance. *ACS Nano*, 6: 6569-6577, 2012.

CITED LITERATURE (continued)

102. Xiao, J., and Chaudhuri, S.: Design of anti-icing coatings using supercooled droplets as nano-to-microscale probes. *Langmuir*, 28: 4434–4446, 2012.
103. Wier, K. A., and McCarthy, T. J.: Condensation on ultrahydrophobic surfaces and its effect on droplet mobility: ultrahydrophobic surfaces are not always water repellent. *Langmuir*, 22: 2433–2436, 2006.
104. Meuler, A. J., Smith, J. D., Varanasi, K. K., Mabry, J. M., McKinley, G. H., and Cohen, R. E.: Relationships between water wettability and ice adhesion. *ACS Appl. Mater. Interfaces*, 2: 3100–3110, 2010.
105. Das, A., Hayvaci, H. T., Tiwari, M. K., Bayer, I.S., Erricolo, D., and Megaridis, C. M.: Superhydrophobic and conductive carbon nanofiber/PTFE composite coatings for EMI shielding. *J. Colloid Interface Sci.*, 353: 311–315, 2011.
106. Das, A., Schutzius, T. M., Bayer, I. S., and Megaridis, C. M.: Superoleophobic and conductive carbon nanofiber/fluoropolymer composite films. *Carbon*, 50:1346-1354, 2012.
107. Tiwari, M.K., Bayer, I.S., Jursich, G.M., Schutzius, T.M., and Megaridis, C.M.: Poly (vinylidene fluoride) and poly (ethyl 2-cyanoacrylate) blends through controlled polymerization of ethyl 2-cyanoacrylates. *Macromol. Mater. Eng.*, 294: 775-780, 2009.
108. Fletcher, N. H.: Effect in Heterogeneous Nucleation. *J. Chem. Phys.*, 29: 572-576, 1958.
109. Gorbunov, B., Baklanov, A., Kakutkin, N., Windsor, H.L., and Toumi, R.: Ice nucleation on soot particles. *J. Aerosol Sci.*, 32: 199-215, 2001.
110. Wenzel, R. N.: Surface roughness and contact angle. *J. Phys. Chem.*, 53:1466-1470, 1949.
111. Turnbull, D., and Vonnegut, B.: Nucleation catalysis. *Ind. Eng. Chem.*, 44: 1292-1298, 1952.
112. Kloubek, J.: Calculation of surface free energy components of ice according to its wettability by water, chlorobenzene, and carbon disulfide. *J. Colloid Interf. Sci.*, 46: 185-190, 1974.
113. Trinh, E. H., and Ohsaka, K.: Measurement of density, sound velocity, surface tension, and viscosity of freely suspended supercooled liquids. *Int. J. Thermophys.*, 16: 545-555, 1995.
114. Israelachvili, J. N.: Intermolecular & Surface Forces. 2nd ed, New York, Academic Press, 1991.
115. Kim, H.I., Kushmerick, J.G., Houston, J.E., and Bunker, B.C.: Viscous “Interphase” Water adjacent to oligo (ethylene glycol)-terminated monolayers. *Langmuir*, 19: 9271-9275, 2003.

CITED LITERATURE (continued)

116. Jung, S., Tiwari, M. K., Poulikakos, D.: Frost halos from supercooled water droplets. *Proc. Natl. Acad. Sci. USA*, 109: 16073-16078, 2012.
117. Kuhn, H.H., Child, A.D., and Kimbrell, W.C.: Toward real applications of conductive polymers. *Synth. Met.*, 71: 2139-2142, 1995.
118. Chandrasekhar, P., and Naishadham, K.: Broadband microwave absorption and shielding properties of a poly (aniline)" *Synth. Met.*, 105: 115-120, 1999.
119. Yang, Y.L., Gupta, M.C., Dudley, K.L., and Lawrence, R.W.: Novel carbon nanotube-polystyrene foam composites for electromagnetic interference shielding. *Nano Lett.*, 5: 2131-2134, 2005.
120. Yang, Y., Gupta, M.C., and Dudley, K.L.: Towards cost-efficient EMI shielding materials using carbon nanostructure-based nanocomposites. *Nanotechnology*, 18: 345701, 2007.
121. Zhu, Y., Zhang, J., Zheng, Y., Huang, Z., Feng, L., and Jiang, L.: Stable, Superhydrophobic, and conductive polyaniline/polystyrene films for corrosive environments. *Adv. Funct. Mater.*, 16: 568-574, 2006.
122. Luo, C., Zuo, X., Wang, L., Wang, E., Song, S., Wang, J., Wang, J., Fan, C., and Cao, Y.: Flexible carbon nanotube-polymer composite films with high conductivity and superhydrophobicity made by solution process. *Nano. Lett.*, 8: 4454-458 , 2008.
123. Meng, L.Y., and Park, S.J.: Effect of fluorination of carbon nanotubes on superhydrophobic properties of fluoro-based films. *J. Colloid Interface Sci.*, 342: 559-563, 2009.
124. Zou, J., Chen, H., Chunder, A., Yu, Y., Huo, Q., and Zhai, L.: Preparation of a superhydrophobic and conductive nanocomposite coating from a carbon-nanotube-conjugated block copolymer dispersion. *Adv. Mater.*, 20: 3337-3341, 2008.
125. Siegel, P. H.: Terahertz Technology. *IEEE Trans. Microwave Theory Tech.*, 50: 910-928, 2002.
126. Globus, T. R., Norton, M. L., Lvovska, M. I., Gregg, D. A., Khromova, T. B., and Gelmont, B. L.: Reliability analysis of THz characterization of modified and unmodified vector sequences. *IEEE Sens. J.*, 10: 410-418, 2010.
127. Brown, E. R., Mendoza, E. A., Xia, D., and Brueck, S. R. J.: Narrow THz spectral signatures through an RNA solution in nanofluidic channels. *IEEE Sens. J.*, 10: 755-759, 2010.
128. Phillips, T. G., and Keene, J.: Sub millimeter astronomy. *Proc. IEEE*, 80: 1662-1678, 1992.

CITED LITERATURE (continued)

129. Liu, L., Xu, H., Lichtenberger, A. W., and Weikle, R. M.: Integrated 585 GHz hot-electron mixers and focal-plane arrays based on annular-slot antennas. *IEEE Trans. Microwave Theory Tech.*, 58: 1943-1951, 2010.
130. Federici, J., and Moeller, L.: Review of terahertz and subterahertz wireless communications. *Appl. Phys. Lett.*, 107: 111101, 2010.
131. Seo, M. A., Yim, J. H., Ahn, Y. H., Rotermund, F., Kim, D. S., Lee, S., and Lim, H.: Terahertz electromagnetic interference shielding using single-walled carbon nanotube flexible films. *Appl. Phys. Lett.*, 93: 231905, 2008.
132. Shenderova, O., Grishko, V., Cunningham, G., Moseenkov, S., McGuire, G., and Kuznetsov, V.: Onion-like Carbon for terahertz electromagnetic shielding. *Diam. Relat. Mater.*, 17: 462-466, 2008.
133. Gommans, H. H., Alldredge, J. W., Tashiro, H., Park, J., Magnuson, J., and Rinzler, A. G.: *J. Appl. Phys.*, 88:2509-2514, 2000.
134. Bird, G. R., and Parrish, M. J.: The wire grid as a near-infrared polarizer. *J. Opt. Soc. Am.*, 50: 886-887, 1960.
135. Zhang, L., Teng, J. H., Tanoto, H., Yew, S. Y., Deng, L. Y., and Chua, S. J.: Terahertz wire-grid polarizer by nanoimprinting lithography on high resistivity silicon substrate, in The International Conference on Infrared, Millimeter, and Terahertz Waves, Rome, Italy, 2010.
136. Yamada, I., Takano, K., Hangyo, M., Saito, M., and Watanabe, W.: Terahertz wire-grid polarizers with micrometer-pitch Al gratings. *Opt. Lett.*, 34: 274-276, 2009.
137. Tian, D.B., Zhang, H.W., Lai, W.E., Wen, Q.E., Song, Y.Q., and Wang, Z.G.: Double wire-grid terahertz polarizer on low-loss polymer substrates. *Chin. Phys. Lett.*, 27: 104210, 2010.
138. Ren, L., Pint, C. L., Booshehri, L. G., Rice, W. D., Wang, X., Hilton, D. J., Takeya, K., Kawayama, I., Tonouchi, M., Hauge, R. H., and Kono, J.: Carbon nanotube terahertz polarizer. *Nano Lett.*, 9: 2610-2613, 2009.
139. Kyoung, J., Jang, E. Y., Lima, M. D., Park, H.R., Robles, R. O., Lepro, X., Kim, Y. H., Baughman, R. H., and Kim, D.S.: A reel-wound carbon nanotube polarizer for terahertz frequencies. *Nano Lett.*, 11: 4227-4231, 2011.
140. Das, A., Megaridis, C. M., Liu, L., Wang, T., and Biswas, A.: Design and synthesis of superhydrophobic carbon nanofiber composite coatings for terahertz frequency shielding and attenuation. *Appl. Phys. Lett.*, 98: 174101, 2011.
141. Orecchini, G., Alimenti, F., Palazzari, V., Rida, A., Tentzeris, M. M., and L. Roselli.: Design and fabrication of ultra-low cost radio frequency identification antennas and tags exploiting paper substrates and inkjet printing technology. *IET Microwaves, Antennas Propag.* 5: 99-1001, 2011.

CITED LITERATURE (continued)

142. Shaker, G., Safavi-Naeini, S., Sangary, N., and Tentzeris, M. M.: Inkjet printing of ultrawideband (UWB) antennas on paper-based substrates. *IEEE Antennas Wireless Propag. Lett.*, 10: 111-114, 2011.
143. Deegan, R. D., Bakajin, O., Dupont, T. F., Huber, G., Nagel, S. R., and Witten, T. A.: Capillary flow as the cause of ring stains from dried liquid drops. *Nature*, 389: 827-829, 1997.
144. Yunker, P. J., Still, T., Lohr, M. A., and Yodh, A. G.: Suppression of the coffee-ring effect by shape-dependent capillary interactions. *Nature*, 476: 308-311, 2011.
145. Hammel, E., Tang, X., Trampert, M., Schmitt, T., Mauthner, K., Eder, A., and Potschke, P.: Carbon nanofibers for composite applications. *Carbon*, 42: 1153-1158, 2004.
146. Yang, S., Lozano, K., Lomeli, A., Foltz, H.D., and Jones, R.: Electromagnetic interference shielding effectiveness of carbon nanofiber/LCP composites. *Composites: Part A*, 36: 691-697, 2005.
147. Liu, L., Hesler, J. L., Weikle, R. M., Wang, T., Fay, P., and Xing, H.: A 570-630 GHz frequency domain spectroscopy based on a quasi-optical broadband Schottky diode detector. *Int. J. High Speed Electron Syst.*, 20: 629-638, 2011.
148. Liu, L., Hesler, J. L., Xu, H., Lichtenberger, A. W., and R. M. Weikle.: A broadband quasi-optical terahertz detector utilizing a zero bias Schottky diode. *IEEE Microw. Wirel. Compon. Lett.*, 20: 504-506, 2010.
149. Jorio, A., Dresselhaus, G., and Dresselhaus, M. S. (eds.): Carbon Nanotubes: Advanced Topics in the Synthesis, Structure, Properties and Applications, Berlin, Springer, 2008.
150. Goldsmith, P. F.: Quasioptical Systems: Gaussian Beam Quasioptical Propagation and Applications, Series on Microwave Technology and Techniques, IEEE/Chapman & Hall, 1997.
151. Manoudis P.N., Karapanagiotis, I., Tsakalof, A., Zuburtikudis, I., and Panayiotou, C.: Superhydrophobic composite films produced on various substrates. *Langmuir*, 24:11225-11232, 2008.
152. Steele, A., Bayer, I.S., and Loth, E.: Inherently superoleophobic nanocomposite coatings by spray atomization. *Nano Lett.*, 9:501-505, 2009.
153. Bayer, I.S., Steele, A., Martorana, P.J., and Loth, E.: Fabrication of superhydrophobic polyurethane/organoclay nano-structured composites from cyclomethicone-in-water emulsions. *Appl. Surf. Sci.*, 257:823-826, 2010.
154. Bayer, I.S, Steele, A., Martorana, P.J., Loth, E., and Miller, L.: Superhydrophobic cellulose-based bio nanocomposite films from Pickering emulsions. *Appl. Phys. Lett.*, 94:163902, 2009.

CITED LITERATURE (continued)

155. Bayer, I.S., Steele, A., Martorana, P., Loth, E., Robinson, S.J., and Stevenson, D.: Biolubricant induced phase inversion and superhydrophobicity in rubber-toughened biopolymer/ organoclay nanocomposites. *Appl. Phys. Lett.*, 95: 063702, 2009.
156. Bayer I.S., Brown, A., Steele, A., and Loth, E.: Transforming anaerobic adhesives into highly durable and abrasion resistant superhydrophobic organoclay nanocomposite films: a new hybrid spray adhesive for tough superhydrophobicity. *Appl. Phys. Exp.*, 2: 125003, 2009.
157. Zhao, J., Piao, G., Wang, X., Lian, J., Wang, Z., Hu, H., Chena, L., Wang, X., Tao, Y., Shi, D.: Improved dispersion of PEG-functionalized carbon nanofibers in toluene. *Mater Sci Eng C*, 29: 742–745. 2009.
158. Chen, H., Muthuraman, H., Stokes, P., Zou, J.H., Liu, X., Wang, J., Huo, Q., Khondaker, S.I., and Zhai, L.: Dispersion of carbon nanotubes and polymer nanocomposite fabrication using trifluoroacetic acid as a cosolvent. *Nanotechnology*, 18:415606, 2007.
159. Tibbetts, G.G., Lake, M.L., Strong, K.L., and Rice, B.P.: A review of the fabrication and properties of vapor-grown carbon nanofiber/ polymer composites. *Compos. Sci. Technol.*, 67:1709–1718, 2007.
160. Wang, K., Hu, N.X., Xu, G., and Qi, Y.: Stable superhydrophobic composite coatings made from an aqueous dispersion of carbon nanotubes and a fluoropolymer. *Carbon*, 49: 1769–1774, 2011.
161. Gao, L.C., and McCarthy, T.J.: The ‘lotus effect’ explained: two reasons why two length scales of topography are important. *Langmuir*, 22:2966–2967, 2006.
162. Beecher, P., Servati, P., Rozhin, A., Colli, A., Scardaci, V., Pisana, S., Hasan, T., Flewitt, A. J., Robertson, J., and Hsieh, G. W.: Ink-jet printing of carbon nanotube thin film transistors. *J. Appl. Phys.*, 102: 043710, 2007.
163. Dragoman, M., Flahaut, E., Dragoman, D., Al Ahmad, M., Plana, R.: Writing simple RF electronic devices on paper with carbon nanotube ink. *Nanotechnology*, 20:375203, 2009.
164. Elwi, T.A., Al-Rizzo H.M., Rucker, D.G., Dervishi, E., Li, Z.R., and Biris, A.S.: Multi-walled carbon nanotube-based RF antennas. *Nanotechnology*, 21: 045301, 2010.
165. Han, X., Janzen, D.C., Vaillancourt, J., and Lu, X.: Printable high-speed thin-film transistor on flexible substrate using carbon nanotube solution. *Micro Nano Lett.*, 2:96–98, 2007.
166. Hsieh, G.W., Li, F.M., Beecher, P., Nathan, A., Wu, Y.L., Ong, B.S., and Milne, W. I.: High performance nanocomposite thin film transistors with bilayer carbon nanotube-polythiophene active channel by ink-jet printing. *J. Appl. Phys.*, 106:123706, 2009.

CITED LITERATURE (continued)

167. Jones, C.S., Lu, X.J., Renn, M., Stroder, M., and Shih, W.S.: Aerosol-jetprinted, high-speed, flexible thin-film transistor made using single-walled carbon nanotube solution. *Microelectron. Eng.*, 87:434–437, 2010.
168. Kordas, K., Mustonen, T., Toth, G., Jantunen, H., Lajunen, M., Soldano, C, Talapatra, S., Kar, S., Vajtai, R., and Ajayan, P. M.: Inkjet printing of electrically conductive patterns of carbon nanotubes. *Small*, 2:1021–1025, 2006.
169. Okimoto, H., Takenobu, T., Yanagi, K., Shimotani, H., Miyata, Y., Kataura, H., and Iwasa, Y.: Low-voltage operation of ink-jet-printed single-walled carbon nanotube thin film transistors. *Jpn J Appl Phys.*, 49:02BD09, 2010.
170. Takenobu, T., Miura, N., Lu, S.Y., Okimoto, H., Asano, T., Shiraishi, M., and Iwasa, Y.: Ink-jet printing of carbon nanotube thin-film transistors on flexible plastic substrates. *Appl. Phys. Exp.*, 2: 025005, 2009.
171. Vaillancourt, J., Zhang, H.Y., Vasinajindakaw, P., Xia, H.T., Lu, X.J., Han, X.L., Janzen, D.C., Shih, W.S., Jones, C.S., Stroder, M., Chen, M.Y., Subbaraman, H., Chen, R.T., Berger, U., and Renn, M.: All ink-jet-printed carbon nanotube thin-film transistor on a polyimide substrate with an ultrahigh operating frequency of over 5 GHz. *Appl. Phys. Lett.*, 93: 243301, 2008.
172. Wei, T., Ruan, J., Fan, Z., Luo, G., and Wei, F.: Preparation of a carbon nanotube film by ink-jet printing. *Carbon*, 45: 2712–2716, 2007.
173. Ozkan, T., Naraghi, M., and Chasiotis, I.: Mechanical properties of vapor grown carbon nanofibers. *Carbon*, 48:239–244, 2010.
174. Pierce, E., Carmona, F.J., and Amirfazli, A.: Understanding of sliding and contact angle results in tilted plate experiments. *Colloid Surf A*, 323:73–82, 2008.
175. Tuteja, A., Choi, W., Ma, M., Mabry, J.M., Mazzella, S.A., and Rutledge, G.C.: Designing superoleophobic surfaces. *Science*, 318:1618–1622, 2007.
176. Wang, S., Zhang, Y., Abidi, N., and Cabrales, L.: Wettability and surface free energy of graphene films. *Langmuir*, 25:11078–11081, 2009.
177. Lin, J.J., Chu, C.C., Chiang, M.L., and Tsai, W.C.: Manipulating assemblies of high-aspect-ratio clays and fatty amine salts to form surfaces exhibiting a lotus effect. *Adv. Mater.*, 18:3248–3252, 2006.
178. Ming, Z., Jian, L., Chunxia, W., Xiaokang, Z., and Lan, C.: Fluid drag reduction on superhydrophobic surfaces coated with carbon nanotube forests (CNTs). *Soft Matter*, 7:4391–4396, 2011.
179. Sethi, S., and Dhinojwala, A.: Superhydrophobic conductive carbon nanotube coatings for steel. *Langmuir*, 25:4311–4313, 2009.

CITED LITERATURE (continued)

180. Morita, M., Ogisu, H., and Kubo, M.: Surface properties of perfluoroalkylethyl acrylate/n-alkyl acrylate copolymers. *J. Appl. Polym. Sci.*, 73:1741–1749, 1999.
181. Zhang, H.B., Yan, Q., Zheng, W.G., He, Z., and Yu, Z.Z.: Tough graphene– polymer microcellular foams for electromagnetic interference shielding. *ACS Appl. Mater. Interf.*, 3:918–924, 2011.
182. Extrand, C.W., and Gent, A.N.: Retention of liquid drops by solid surfaces. *J. Colloid. Interf. Sci.*, 138:431–442, 1990.
183. Brinkmann, M., and Lipowsky, R.: Wetting morphologies on substrates with striped surface domains. *J. Appl. Phys.*, 92:4296–4306, 2002.
184. Szczech, J.B., Megaridis, C.M., Gamota, D.R., and Zhang, J.: Fine-line conductor manufacturing using advanced drop-on-demand PZT printing technology. *IEEE Trans. Electron. Packag. Manuf.*, 25:26–33, 2002.
185. Szczech, J.B., Megaridis, C.M., Zhang, J., and Gamota, D.R.: Ink jet processing of metallic nanoparticle suspensions for electronic circuitry fabrication. *Microscale Thermophys. Eng.*, 8:327–39, 2004.
186. Liu, C., Fan, Y. Y., Liu, M., Cong, H. T., Cheng, H. M., and Dresselhaus, M. S.: Hydrogen storage in single-walled carbon nanotubes at room temperature. *Science*, 286:1127–1129, 1999.
187. Misewich, J. A., Martel, R., Avouris, P., Tsang, J. C., Heinze, S., and J. T.: Electrically induced optical emission from a carbon nanotube FET. *Science*, 300:783–786, 2003.
188. Bachtold, A., Hadley, P., Nakanishi, T., and Dekker, C.: Logic circuits with carbon nanotube transistors. *Science*, 294:1317–1320, 2001.
189. Kuzmany, H., Fink, J., Mehring, M., and Roth, S. (eds): Nanotube. In: *Electronic Properties of Molecular Nanostructures*, pp. 562–567. New York, Springer, 2001.
190. Dai, H., Kong, J., Zhou, C., Franklin, N., Tomblor, T., Cassell, A., Fan, S., and Chapline, M.: Controlled chemical routes to nanotube architectures, Physics, and Devices. *J. Phys. Chem. B*, 103: 11246–11255, 1999.
191. Sloan, J., Wright, D. M., Bailey, S., Brown, G., York, A. P. E., Coleman, K. S., Green, M. L. H., Sloan, J., Wright, D. M., Hutchison, J. L., and Woo, H.G.: Capillarity and silver nanowire formation observed in single walled carbon nanotubes. *Chem. Commun.*, 699–700, 1999.
192. Charlier, J., Lambin, P., and Ebbesen, T.: Electronic properties of carbon nanotubes with polygonized cross sections. *Phys. Rev. B: Condens. Matter*, 54:R8377–R8380, 1996.
193. Mönch, I., Meye, A., Leonhardt, A., Krämer, K., Kozhuharova, R., Gemming, T., Wirth, M. P., Büchner, B.: Ferromagnetic filled carbon nanotubes and nanoparticles:

CITED LITERATURE (continued)

- synthesis and lipid-mediated delivery into human tumor cells. *J. Magn. Magn. Mater.*, 290:276–278, 2005.
194. Luo, J., Mark, L. P., Giannakopoulos, A. E., Colburn, A. W., Macpherson, J. V., Drewello, T., Derrick, P. J., Teh, A. S., Teo, K. B. K., and Milne, W. I.: Field ionization using densely spaced arrays of nickel-tipped carbon nanotubes. *Chem. Phys. Lett.*, 505:126–129, 2011.
 195. Day, T. M., Unwin, P. R., and Macpherson, J. V.: Factors controlling the electrodeposition of metal nanoparticles on pristine single walled carbon nanotubes. *Nano Lett.*, 7:51–57, 2007.
 196. Day, T. M., Unwin, P. R., Wilson, N. R., and Macpherson, J. V.: Electrochemical templating of metal nanoparticles and nanowires on single-walled carbon nanotube networks. *J. Am. Chem. Soc.*, 127:10639–10647, 2005.
 197. Cheng, H., Qiu, H., Zhu, Z., Li, M., and Shi, Z.: Investigation of the electrochemical behavior of dopamine at electrodes modified with ferrocene-filled double-walled carbon nanotubes. *Electrochim. Acta*, 63:83–88, 2012.
 198. Costa, P. M. F. J., Coleman, K. S., and Green, M. L. H.: Influence of catalyst metal particles on the hydrogen sorption of single-walled carbon nanotube materials. *Nanotechnology*, 16:512–517, 2005.
 199. Chou, S. Y., Wei, M. S., Krauss, P. R., and Fischer, P. B.: Single-domain magnetic pillar array of 35 nm diameter and 65 Gbits/in² density for ultrahigh density quantum magnetic storage. *J. Appl. Phys.*, 76:6673–6675, 1994.
 200. Dong, X., Lau, C. M., Lohani, A., Mhaisalkar, S. G., Kasim, J., Shen, Z., Ho, X., Rogers, J. A., and Li, L.-J.: Electrical detection of femtomolar DNA via gold-nanoparticle enhancement in carbon-nanotube-network field-effect transistors. *Adv. Mater.*, 20:2389–2393, 2008.
 201. Dong, X., Fu, D., Ahmed, M. O., Shi, Y., Mhaisalkar, S. G., Zhang, S., Moochhala, S., Ho, X., Rogers, J. A., and Li, L.-J.: Heme-enabled electrical detection of carbon monoxide at room temperature using networked carbon nanotube field-effect transistors. *Chem. Mater.*, 19:6059–6061, 2007.
 202. Castillejos, E., Debouttière, P.-J., Roiban, L., Solhy, A., Martinez, V., Kihn, Y., Ersen, O., Philippot, K., Chaudret, B., and Serp, P.: An efficient strategy to drive nanoparticles into carbon nanotubes and the remarkable effect of confinement on their catalytic performance. *Angew. Chem. Int. Ed.*, 48:2529–2533, 2009.
 203. Wang, C., Guo, S., Pan, X., Chen, W., and Bao, X.: Tailored cutting of carbon nanotubes and controlled dispersion of metal nanoparticles inside their channels. *J. Mater. Chem.*, 18:5782–5786, 2008.

CITED LITERATURE (continued)

204. Palaniselvam, T., Kannan, R., and Kurungot, S.: Facile construction of non-precious iron nitride-doped carbon nanofibers as cathode electrocatalysts for proton exchange membrane fuel cells. *Chem. Commun.*, 47: 2910–2912, 2011.
205. Winkler, A., Mühl, T., Menzel, S., Kozhuharova-Koseva, R., Hampel, S., Leonhardt, A., and Büchner, B.: Magnetic force microscopy sensors using iron-filled carbon nanotubes. *J. Appl. Phys.*, 99:104905, 2006.
206. Pan, X., and Bao, X.: Reactions over catalysts confined in carbon nanotubes. *Chem. Commun.*, 47:6271–6281, 2008.
207. Dresselhaus, M., Dresselhaus, G., and Avouris, P. (eds): Carbon Nanotubes: Synthesis, Properties and Applications, In Topics in Applied Physics, Berlin, Heidelberg, New York, Springer-Verlag, 2001.
208. Lee, J., Park, J., Kim, J., Yi, W.: Efficient visible photoluminescence from encapsulation of fluorescent materials inside single-walled carbon nanotubes. *Colloids and Surfaces A*, 313-314:296–299, 2008.
209. Sinha-Ray, S., Sahu, R. P., and Yarin, A. L.: Nano-encapsulated smart tunable phase change materials. *Soft Matter*, 7:8823-8827, 2011.
210. Smith, B. W., Monthieux, M., and Luzzi, D. E.: Carbon nanotube encapsulated fullerenes : a unique Class of hybrid materials. *Chem. Phys. Lett.*, 315:31–36, 1999.
211. Takenobu, T., Takano, T., Shiraishi, M., Murakami, Y., Ata, M., Kataura, H., Achiba, Y., and Iwasa, Y.: Stable and controlled amphoteric doping by encapsulation of organic molecules inside carbon nanotubes. *Nature Mater.*, 2:683–688, 2003.
212. Li, L.-J., Khlobystov, A. N., Wiltshire, J. G., Briggs, G. A.D., and Nicholas, R. J.: Diameter-selective encapsulation of metallocenes in single-walled carbon nanotubes. *Nature Mater.*, 4:481–485, 2005.
213. Demoncey, N., and St, O.: Filling carbon nanotubes with metals by the arc-discharge method : the key role of sulfur. *Eur. Phys. J. B*, 4:147–157, 1998.
214. Guerretpiecourt, C., Lebouar, Y., Loiseau, A., Pascard, H. Relation between metal electronic structure and morphology of metal compounds inside carbon nanotubes. *Nature*, 372:761–765, 1994.
215. Guan, L., Shi, Z., Li, M., and Gu, Z.: Ferrocene-filled single-walled carbon nanotubes. *Carbon*, 43: 2780–2785, 2005.
216. Ugarte, D., Chatelain, A, and de Heer, W.A.: Nanocapillarity and chemistry in carbon nanotubes. *Science*, 274:1897–1899, 1996.
217. Ajayan, P. M., and Iijima, S.: Capillarity-induced filling of carbon nanotubes. *Nature*, 361:333–334, 1993.

CITED LITERATURE (continued)

218. Tsang, S. C., Chen, Y. K., Harris, P. J. F., and Green, M. L. H.: A simple chemical method of opening and filling carbon nanotubes. *Nature*, 372:159–162, 1994.
219. Ebbesen, W.: Wetting, filling and decorating. *J. Phys. Chem. Solids*, 57:951–955, 1996.
220. Chu, A., Cook, J., Heesom, R. J. R., Hutchison, J. L., Green, and M. L. H., Sloan, J.: Filling of carbon nanotubes with silver, gold, and gold chloride. *Chem. Mater.*, 8:2751–2754, 1996.
221. Qiu, H., Shi, Z., Zhang, S.L., Gu, Z., and Qiu, J.: Synthesis and Raman scattering study of double-walled carbon nanotube peapods. *Solid State Commun.*, 137:654–657, 2006.
222. Okazaki, T., Suenaga, K., Hirahara, K., Bandow, S., Iijima, S., Shinohara, H., and Corporation, T.: Real time reaction dynamics in carbon nanotubes. *J. Am. Chem. Soc.*, 123:9673–9674, 2001.
223. Brune, H., Ernst, H., Grunwald, A., Grünwald, W., Hofmann, H., Krug, H., Janich, P., Mayor, M., Rathgeber, W., Schmid, G., Simon, U., Vogel, and V., D. W.: Nanotechnology: Assessment and Perspectives. In: Ethics of Science and Technology Assessment Vol 27, eds. C.F. Gethmann, K. Mader, and F. Wutscher. Berlin, Heidelberg, Springer, 2006.
224. Goldstein, A. N., Echer, C. M., and Alivisatos, A. P.: Melting in semiconductor nanocrystals. *Science*, 256:1425–1427, 1992.
225. Torre, A. La, Rance, G. A., Harfi, J. El, Li, J., Irvine, D. J., Brown, P. D., and Khlobystov, A. N.: Transport and encapsulation of gold nanoparticles in carbon nanotubes. *Nanoscale*, 2:1006–1010, 2010.
226. Tîlmaciu, C.M., Soula, B., Galibert, A.M., Lukanov, P., Datas, L., González, J., Barquín, L. F., Rodríguez Fernández, J., González-Jiménez, F., Jorge, J., and Flahaut, E.: Synthesis of superparamagnetic iron (III) oxide nanowires in double-walled carbon nanotubes. *Chem. Commun.*:6664–6666, 2009.
227. Wolny, F., Mühl, T., Weissker, U., Lipert, K., Schumann, J., Leonhardt, A., and Büchner, B.: Iron filled carbon nanotubes as novel monopole-like sensors for quantitative magnetic force microscopy. *Nanotechnology*, 21:435501, 2010.
228. Tessonier, J.P., Ersen, O., Weinberg, G., Pham-Huu, C., Su, D. S., and Schlögl, R.: Selective deposition of metal nanoparticles inside or outside multiwalled carbon nanotubes. *ACS Nano*, 3: 2081–2089, 2009.
229. Pyrograf products: <http://pyrografproducts.com/nanofiber.html>.
230. Bazilevsky, A. V, Sun, K., Yarin, A. L., Megaridis, C. M.: Selective intercalation of polymers in carbon nanotubes. *Langmuir*, 23:7451–7455, 2007.

CITED LITERATURE (continued)

231. Bazilevsky, A. V., Sun, K., Yarin, A. L., and Megaridis, C. M.: Room-temperature, open-air, wet intercalation of liquids, surfactants, polymers and nanoparticles within nanotubes and microchannels. *J. Mater. Chem.*, 18:696-702, 2008.
232. Ye, H., Naguib, N., Gogotsi, Y., Yazicioglu, A. G., and Megaridis, C. M.: Wall structure and surface chemistry of hydrothermal carbon nanofibres. *Nanotechnology*, 15:232–236, 2004.

APPENDIX

Re print permission letter for figure 13 a, b

7/30/13

Rightslink Printable License

AMERICAN INSTITUTE OF PHYSICS LICENSE TERMS AND CONDITIONS

Jul 30, 2013

All payments must be made in full to CCC. For payment instructions, please see information listed at the bottom of this form.

License Number	3198960799933
Order Date	Jul 30, 2013
Publisher	American Institute of Physics
Publication	Applied Physics Letters
Article Title	Bioinspired construction of Mg-Li alloys surfaces with stable superhydrophobicity and improved corrosion resistance
Author	Kesong Liu, Milin Zhang, Jin Zhai, Jun Wang, et al.
Online Publication Date	May 6, 2008
Volume number	92
Issue number	18
Type of Use	Thesis/Dissertation
Requestor type	Student
Format	Print and electronic
Portion	Figure/Table
Number of figures/tables	2
Title of your thesis / dissertation	Functional Polymer Nanocomposites and Nanohybrids: Synthesis, Characterization and Application
Expected completion date	Aug 2013
Estimated size (number of pages)	160
Total	0.00 USD

Terms and Conditions

American Institute of Physics -- Terms and Conditions: Permissions Uses

American Institute of Physics ("AIP") hereby grants to you the non-exclusive right and license to use and/or distribute the Material according to the use specified in your order, on a one-time basis, for the specified term, with a maximum distribution equal to the number that you have ordered. Any links or other content accompanying the Material are not the subject of this license.

1. You agree to include the following copyright and permission notice with the reproduction of the Material: "Reprinted with permission from [FULL CITATION]. Copyright [PUBLICATION YEAR], American Institute of Physics." For an article, the copyright and permission notice must be printed on the first page of the article or book chapter. For photographs, covers, or tables, the copyright and permission notice may appear with the Material, in a footnote, or in the reference list.
2. If you have licensed reuse of a figure, photograph, cover, or table, it is your responsibility to ensure that the material is original to AIP and does not contain the copyright of another entity, and that the copyright notice of the figure, photograph, cover, or table does not indicate that it was reprinted by AIP, with permission, from another source. Under no circumstances does AIP, purport or intend to grant permission to reuse material to which it

<https://s100.copyright.com/AppDispatchServlet>

1/3

does not hold copyright.

3. You may not alter or modify the Material in any manner. You may translate the Material into another language only if you have licensed translation rights. You may not use the Material for promotional purposes. AIP reserves all rights not specifically granted herein.
4. The foregoing license shall not take effect unless and until AIP or its agent, Copyright Clearance Center, receives the Payment in accordance with Copyright Clearance Center Billing and Payment Terms and Conditions, which are incorporated herein by reference.
5. AIP or the Copyright Clearance Center may, within two business days of granting this license, revoke the license for any reason whatsoever, with a full refund payable to you. Should you violate the terms of this license at any time, AIP, American Institute of Physics, or Copyright Clearance Center may revoke the license with no refund to you. Notice of such revocation will be made using the contact information provided by you. Failure to receive such notice will not nullify the revocation.
6. AIP makes no representations or warranties with respect to the Material. You agree to indemnify and hold harmless AIP, American Institute of Physics, and their officers, directors, employees or agents from and against any and all claims arising out of your use of the Material other than as specifically authorized herein.
7. The permission granted herein is personal to you and is not transferable or assignable without the prior written permission of AIP. This license may not be amended except in a writing signed by the party to be charged.
8. If purchase orders, acknowledgments or check endorsements are issued on any forms containing terms and conditions which are inconsistent with these provisions, such inconsistent terms and conditions shall be of no force and effect. This document, including the CCC Billing and Payment Terms and Conditions, shall be the entire agreement between the parties relating to the subject matter hereof.

This Agreement shall be governed by and construed in accordance with the laws of the State of New York. Both parties hereby submit to the jurisdiction of the courts of New York County for purposes of resolving any disputes that may arise hereunder.

If you would like to pay for this license now, please remit this license along with your payment made payable to "COPYRIGHT CLEARANCE CENTER" otherwise you will be invoiced within 48 hours of the license date. Payment should be in the form of a check or money order referencing your account number and this invoice number RLNK501079166. Once you receive your invoice for this order, you may pay your invoice by credit card. Please follow instructions provided at that time.

**Make Payment To:
Copyright Clearance Center
Dept 001
P.O. Box 843006
Boston, MA 02284-3006**

For suggestions or comments regarding this order, contact RightsLink Customer Support: customercare@copyright.com or +1-877-622-5543 (toll free in the US) or +1-978-646-2777.

Gratis licenses (referencing \$0 in the Total field) are free. Please retain this printable license for your reference. No payment is required.

Re print permission letters for figure 13c and 14

7/30/13

Rightslink Printable License

**THE ROYAL SOCIETY LICENSE
TERMS AND CONDITIONS**

Jul 30, 2013

This is a License Agreement between Arindam Das ("You") and The Royal Society ("The Royal Society") provided by Copyright Clearance Center ("CCC"). The license consists of your order details, the terms and conditions provided by The Royal Society, and the payment terms and conditions.

License Number	3198940846554
License date	Jul 30, 2013
Licensed content publisher	The Royal Society
Licensed content publication	Philosophical Transactions A
Licensed content title	Superhydrophobic and superhydrophilic plant surfaces: an inspiration for biomimetic materials
Licensed ccopyright line	Copyright © 2009, The Royal Society
Licensed content author	Kerstin Koch, Wilhelm Barthlott
Licensed content date	2009
Volume number	367
Issue number	1893
Type of Use	Thesis/Dissertation
Requestor type	academic/educational
Format	print and electronic
Portion	figures/tables/images
Quantity	7
Will you be translating?	no
Circulation	10000
Order reference number	
Title of your thesis / dissertation	Functional Polymer Nanocomposites and Nanohybrids: Synthesis, Characterization and Application
Expected completion date	Aug 2013
Estimated size (number of pages)	160
Billing Type	Credit Card
Credit card info	Visa ending in 8876
Credit card expiration	09/2014
Permissions Cost	4.20 USD
VAT (0.0%)	0.00 USD

<https://s100.copyright.com/AppDispatchServlet>

1/3

7/30/13

Rightslink Printable License

Total 4.20 USD

[Terms and Conditions](#)

STANDARD TERMS AND CONDITIONS FOR REPRODUCTION OF MATERIAL FROM A ROYAL SOCIETY JOURNAL

1. Use of the material is restricted to the type of use specified in your order details.
2. The publisher for this copyrighted material is the Royal Society. By clicking "accept" in connection with completing this licensing transaction, you agree that the following terms and conditions apply to this transaction (along with the Billing and Payment terms and conditions established by Copyright Clearance Center, Inc. ("CCC"), at the time that you opened your Rightslink account and that are available at any time at <http://myaccount.copyright.com>.
3. You may not alter or modify the material in any manner, nor may you translate the material into another language without written consent of the Royal Society.
4. The following credit line appears wherever the material is used: author, title, journal, year, volume, issue number, pagination, by permission of the Royal Society.
5. For the reproduction of a full article from a Royal Society journal for whatever purpose, the corresponding author of the material concerned should be informed of the proposed use. Contact details for the corresponding authors of all Royal Society journals can be found alongside either the abstract or full text of the article concerned, accessible from royalsocietypublishing.org.
6. If the credit line in our publication indicates that any of the figures, images or photos was reproduced from an earlier source it will be necessary for you to clear this permission with the original publisher as well. If this permission has not been obtained, please note that this material cannot be included in your publication/photocopies.
7. Licenses may be exercised anywhere in the world.
8. While you may exercise the rights licensed immediately upon issuance of the license at the end of the licensing process for the transaction, provided that you have disclosed complete and accurate details of your proposed use, no license is finally effective unless and until full payment is received from you (either by publisher or by CCC) as provided in CCC's Billing and Payment terms and conditions. If full payment is not received on a timely basis, then any license preliminarily granted shall be deemed automatically revoked and shall be void as if never granted. Further, in the event that you breach any of these terms and conditions or any of CCC's Billing and Payment terms and conditions, the license is automatically revoked and shall be void as if never granted. Use of materials as described in a revoked license, as well as any use of the materials beyond the scope of an unrevoked license, may constitute copyright infringement and publisher reserves the right to take any and all action to protect its copyright in the materials.
9. Publisher reserves all rights not specifically granted in the combination of (i) the license details provided by you and accepted in the course of this licensing transaction, (ii) these terms and conditions and (iii) CCC's Billing and Payment terms and conditions.

7/30/13

Rightslink Printable License

10. Publisher makes no representations or warranties with respect to the licensed material.
11. You hereby indemnify and agree to hold harmless publisher and CCC, and their respective officers, directors, employees and agents, from and against any and all claims arising out of your use of the licensed material other than as specifically authorized pursuant to this license.
12. This license may not be amended except in a writing signed by both parties (or, in the case of publisher, by CCC on publisher's behalf).

If you would like to pay for this license now, please remit this license along with your payment made payable to "COPYRIGHT CLEARANCE CENTER" otherwise you will be invoiced within 48 hours of the license date. Payment should be in the form of a check or money order referencing your account number and this invoice number RLNK501079119. Once you receive your invoice for this order, you may pay your invoice by credit card. Please follow instructions provided at that time.

**Make Payment To:
Copyright Clearance Center
Dept 001
P.O. Box 843006
Boston, MA 02284-3006**

For suggestions or comments regarding this order, contact RightsLink Customer Support: customercare@copyright.com or +1-877-622-5543 (toll free in the US) or +1-978-646-2777.

Gratis licenses (referencing \$0 in the Total field) are free. Please retain this printable license for your reference. No payment is required.

Re print permission letter for figure 13 d.e.f

7/30/13

Rightslink® by Copyright Clearance Center



RightsLink®

[Home](#)
[Account Info](#)
[Help](#)

ACS Publications
 High quality. High impact.

Title: Superior Water Repellency of Water Strider Legs with Hierarchical Structures: Experiments and Analysis

Logged in as:
 Arindam Das
 Account #:
 3000654163

Author: Xi-Qiao Feng et al.

Publication: Langmuir

Publisher: American Chemical Society

Date: Apr 1, 2007

Copyright © 2007, American Chemical Society

[LOGOUT](#)

PERMISSION/LICENSE IS GRANTED FOR YOUR ORDER AT NO CHARGE

This type of permission/license, instead of the standard Terms & Conditions, is sent to you because no fee is being charged for your order. Please note the following:

- Permission is granted for your request in both print and electronic formats, and translations.
- If figures and/or tables were requested, they may be adapted or used in part.
- Please print this page for your records and send a copy of it to your publisher/graduate school.
- Appropriate credit for the requested material should be given as follows: "Reprinted (adapted) with permission from (COMPLETE REFERENCE CITATION). Copyright (YEAR) American Chemical Society." Insert appropriate information in place of the capitalized words.
- One-time permission is granted only for the use specified in your request. No additional uses are granted (such as derivative works or other editions). For any other uses, please submit a new request.

If credit is given to another source for the material you requested, permission must be obtained from that source.

[BACK](#)
[CLOSE WINDOW](#)

Copyright © 2013 [Copyright Clearance Center, Inc.](#) All Rights Reserved. [Privacy statement.](#) Comments? We would like to hear from you. E-mail us at customercare@copyright.com

Re print permission letter for figure 15

6/21/13

Rightslink Printable License

**NATURE PUBLISHING GROUP LICENSE
TERMS AND CONDITIONS**

Jun 21, 2013

This is a License Agreement between Arindam Das ("You") and Nature Publishing Group ("Nature Publishing Group") provided by Copyright Clearance Center ("CCC"). The license consists of your order details, the terms and conditions provided by Nature Publishing Group, and the payment terms and conditions.

All payments must be made in full to CCC. For payment instructions, please see information listed at the bottom of this form.

License Number	3173941305300
License date	Jun 21, 2013
Licensed content publisher	Nature Publishing Group
Licensed content publication	Nature
Licensed content title	Water capture by a desert beetle
Licensed content author	Andrew R. Parker, Chris R. Lawrence
Licensed content date	Nov 1, 2001
Volume number	414
Issue number	6859
Type of Use	reuse in a thesis/dissertation
Requestor type	academic/educational
Format	print and electronic
Portion	figures/tables/illustrations
Number of figures/tables/illustrations	3
Figures	Figure 1 in paper and Figure 15 in Thesis
Author of this NPG article	no
Your reference number	
Title of your thesis / dissertation	Functional Polymer Nanocomposites and Nanohybrids: Synthesis, Characterization and Application
Expected completion date	Aug 2013
Estimated size (number of pages)	200
Total	0.00 USD
Terms and Conditions	Terms and Conditions for Permissions

Nature Publishing Group hereby grants you a non-exclusive license to reproduce this material for this purpose, and for no other use, subject to the conditions below:

1. NPG warrants that it has, to the best of its knowledge, the rights to license reuse of this material. However, you should ensure that the material you are requesting is original to Nature Publishing Group and does not carry the copyright of another entity (as credited in the published version). If the credit line on any part of the material you have requested indicates that it was reprinted or adapted by NPG with permission from another source, then you should also seek permission from that source to reuse the material.
2. Permission granted free of charge for material in print is also usually granted for any electronic version of that work, provided that the material is incidental to the work as a whole and that the electronic version is essentially equivalent to, or substitutes for, the print version. Where print permission has been granted for a fee, separate permission must be obtained for any additional, electronic re-use (unless, as in the case of a full paper, this has already been accounted for during your initial request in the calculation of a print run). NB: In all cases, web-based use of full-text articles must be authorized separately through the 'Use on a Web Site' option when requesting permission.
3. Permission granted for a first edition does not apply to second and subsequent editions and for editions in other languages (except for signatories to the STM Permissions Guidelines, or where the first edition permission was granted for free).
4. Nature Publishing Group's permission must be acknowledged next to the figure, table or abstract in print. In electronic form, this acknowledgement must be visible at the same time as the figure/table/abstract, and must be hyperlinked to the journal's homepage.
5. The credit line should read:
 Reprinted by permission from Macmillan Publishers Ltd: [JOURNAL NAME] (reference citation), copyright (year of publication)
 For AOP papers, the credit line should read:
 Reprinted by permission from Macmillan Publishers Ltd: [JOURNAL NAME], advance online publication, day month year (doi: 10.1038/sj.[JOURNAL ACRONYM].XXXXX)

Note: For republication from the *British Journal of Cancer*, the following credit lines apply.

Reprinted by permission from Macmillan Publishers Ltd on behalf of Cancer Research UK: [JOURNAL NAME] (reference citation), copyright (year of publication) For AOP papers, the credit line should read:
 Reprinted by permission from Macmillan Publishers Ltd on behalf of Cancer Research UK: [JOURNAL NAME], advance online publication, day month year (doi: 10.1038/sj.[JOURNAL ACRONYM].XXXXX)

6. Adaptations of single figures do not require NPG approval. However, the adaptation should

be credited as follows:

Adapted by permission from Macmillan Publishers Ltd: [JOURNAL NAME] (reference citation), copyright (year of publication)

Note: For adaptation from the *British Journal of Cancer*, the following credit line applies.

Adapted by permission from Macmillan Publishers Ltd on behalf of Cancer Research UK: [JOURNAL NAME] (reference citation), copyright (year of publication)

7. Translations of 401 words up to a whole article require NPG approval. Please visit <http://www.macmillanmedicalcommunications.com> for more information. Translations of up to a 400 words do not require NPG approval. The translation should be credited as follows:

Translated by permission from Macmillan Publishers Ltd: [JOURNAL NAME] (reference citation), copyright (year of publication).

Note: For translation from the *British Journal of Cancer*, the following credit line applies.

Translated by permission from Macmillan Publishers Ltd on behalf of Cancer Research UK: [JOURNAL NAME] (reference citation), copyright (year of publication)

We are certain that all parties will benefit from this agreement and wish you the best in the use of this material. Thank you.

Special Terms:

v1.1

If you would like to pay for this license now, please remit this license along with your payment made payable to "COPYRIGHT CLEARANCE CENTER" otherwise you will be invoiced within 48 hours of the license date. Payment should be in the form of a check or money order referencing your account number and this invoice number RLNK501048898. Once you receive your invoice for this order, you may pay your invoice by credit card. Please follow instructions provided at that time.

**Make Payment To:
Copyright Clearance Center
Dept 001
P.O. Box 843006
Boston, MA 02284-3006**

For suggestions or comments regarding this order, contact RightsLink Customer Support: customercare@copyright.com or +1-877-622-5543 (toll free in the US) or +1-978-646-2777.

Gratis licenses (referencing \$0 in the Total field) are free. Please retain this printable license for your reference. No payment is required.

6/21/13

Rightslink Printable License

VITA

NAME Arindam Das

EDUCATION B.E., Mechanical Engineering, Jadavpur University, India, 2006
Ph.D., Mechanical and Industrial Engineering, University of Illinois at Chicago- Expected Summer, 2013

TEACHING EXPERIENCE Teaching Assistant (TA), Mechanical and Industrial Engineering, in Internal Combustion Engines (ME 429), Heat Transfer (ME 321), Experimental Methods in Mechanical, Engineering (ME 341), Fluid Mechanics I (ME 211), Fall 2007-2012.

HONORS Chancellors Student Service and Leadership Award, 2010, University of Illinois at Chicago.

PROFESSIONAL Member, American Society of Mechanical Engineers.

PUBLICATIONS Das, A., Hayvaci, H. T., Tiwari, M. K., Bayer, I.S., Erricolo, D., and Megaridis, C. M.: Superhydrophobic and conductive carbon nanofiber/PTFE composite coatings for EMI shielding. *J. Colloid Interface Sci.*, 353: 311–315, 2011.

Jung, S., Dorrestijn, M., Raps, D., Das, A., Megaridis, C.M., and Poulidakos, D.: Are superhydrophobic surfaces best for icephobicity? *Langmuir*, 27: 3059–3066, 2011.

Das, A., Megaridis, C. M., Liu, L., Wang, T., and Biswas, A.: Design and synthesis of superhydrophobic carbon nanofiber composite coatings for terahertz frequency shielding and attenuation. *Appl. Phys. Lett.*, 98: 174101, 2011.

Das, A., Schutzius, T. M., Bayer, I. S. and Megaridis, C. M.: Superoleophobic and conductive carbon nanofiber/fluoropolymer composite films. *Carbon*, 50:1346-1354, 2012.

Schutzius, T. M., Bayer, I. S., Jursich, G M., Das, A., and Megaridis, C. M.: Superhydrophobic- Superhydrophilic Binary Micropatterns by Localized Thermal Treatment of Polyhedral Oligomeric Silsesquioxane (POSS)-Silica Films. *Nanoscale*, 4: 5378-5385, 2012.

Das, A., Schutzius, T.M., Megaridis, C. M., Subhechha, S., Wang, T., and Liu. L.: Quasi-optical Terahertz Polarizers Enabled by Inkjet Printing of Carbon Nanocomposites. *Appl. Phys. Lett.*, 101: 243108, 2012.

Das, A., Raffi, M., Megaridis, C. M., and Fragouli, D. : Anisotropic Polymer composite film made of Magnetic nanoparticle filled Carbon Nanofibers (Article in preparation).

Kapatral, S., Das, A., and Megaridis, C.M.: Role of surface wettability and morphology on Passive condensation and active deicing/defrosting process on the CNF-PMC conductive superhydrophobic surface. (Article in preparation).

Patents and Disclosures

C. M. Megaridis, T. Schutzius and A. Das, “Elastomeric (Stretchable) Electrically-Conducting Composite Coatings,” Invention Disclosure DE153 (filed on 5-31-2011).

C. M. Megaridis, I. S. Bayer, M. K. Tiwari and A. Das, “Liquid-Repellent, Large-area, Electrically-Conducting Polymer Composite Coatings,” US Non-provisional Patent Application 13/156,908 (filed on 6-9-2011).